UNIVERSITÉ DU QUÉBEC
INRS- ÉNERGIE, MATÉRIAUX ET TÉLÉCOMMUNICATIONS

Development of an intense THz source using tilted pulse front method in $LiNbO_3$ crystal and its application in non-linear THz spectroscopy

par
Gargi Sharma

Thèse présentée
pour l'obtention
du grade de PhilosophiæDoctor (Ph.D.)
en Sciences de l'Énergie et des Matériaux

Jury d'évaluation

Président du jury et examinateur interne	Dr. Francois Vidal, (INRS-EMT)
Examinateur externes	Dr. Daniel Mittleman, (Rice University)
	Dr. Safieddin Safavi-Naeini, (University of waterloo)
Directeur de recherche	Dr. Tsuneyuki Ozaki, (INRS-EMT)
Codirecteur de recherche	Dr. Roberto Morandotti, (INRS-EMT)

Abstract

The aim of this thesis was to develop an intense THz sources using tilted pulse front technique and its application in nonlinear THz spectroscopy of semiconductors and graphene.

At the Advanced Laser Light Source, an intense THz source based on large aperture ZnTe crystal had already been available. This source uses 50mJ laser energy to generate THz pulses with 1μJ energy. The main limitation of the ZnTe based source is its low signal to noise ratio, as it uses the 100Hz laser system, where the pulse to pulse fluctuation may vary up to 10%.

To overcome the limited signal to noise ratio and to increase the efficiency of THz generation, a new intense THz source based on the tilted pulse front technique in $LiNbO_3$ crystal is designed and developed as a first part of this thesis.

At the time of source characterization it was realized that the measurement of intense THz electric field is a big challenge, as the conventional electro-optic sampling technique suffers from the limitation of over-rotation. In this thesis work a new detection technique has been demonstrated based on spectral domain interferometry, which not only overcomes the limitation of over-rotation but also significantly simplifies the detection system.

Using the developed intense THz sources, the nonlinear response of semiconductors like GaAs are investigated. Optical pump-THz probe technique is used to investigate the carrier dynamics in GaAs sample. When the THz electric field is intense enough, it not only probes but also pumps the semiconductor which is observed as absorption bleaching of the intense THz pulse in the GaAs sample. The first experiment was done at fixed optical pump fluence. For further investigation, the optical pump fluence is increased and as a result THz induced absorption bleaching is decreased. The results are modeled using intervalley

scattering Drude model. This simple model explains the experiment results quite well.

Next, using the available THz sources, the linear and nonlinear properties of graphene have been investigated. The sheet conductivity of the graphene sample is investigated using a low energy THz source. The sheet conductivity varies from sample to sample and can be used to test the quality of the graphene sample. After performing linear characterization, the nonlinear properties of graphene sample are also investigated using intense THz sources available at ALLS. The results show that when the graphene sample is pumped with an intense THz electric field, the frequency multiplication effect takes place. This is the first experimental demonstration of the nonlinear effects at THz frequencies. We are in collaboration with Tokyo University for theoretical modeling of these experimental observations.

Acknowledgement

First of all I would like to thank my principle supervisor Dr. Tsuyenuki Ozaki for his constant support throughout my doctoral work. His excellent guidance, motivation and immense knowledge always inspired me. This work would not have taken its present shape without him.

I am honored to work with Dr. Roberto Morandotti, my co-supervisor, who put a lot of efforts in arranging the funding for several of my doctoral projects. He has been an excellent critic and a great source of improvisation.

My sincere thanks also goes to Dr. David Cook (McGill University) who is although not on my supervisor list but has guided me and helped me understanding my work a lot.

Besides my supervisors, my lab members have also played a crucial role in completion of my thesis. I would like to thank Dr. Francois Blanchard who helped me in initial course of my work. Dr. Ibraheem Al-Naib supported me throughout my PhD work, whether it was in the lab or writing papers, he was always there to provide his valuable suggestions to improve the work. I am thankful to Dr. Luca Razzari as well for helping me in understating the theoretical aspects of the experimental work that I performed. A big thank to Regis Imbault who helped with the French translation of my thesis abstract.

The ALLS facility at INRS is a major contributor to the success of this work. I am thankful Amelie Auger, Mathieu Giguere, Stephane Payeur, Francois Poitras and all other members of ALLS. Special thanks goes to Antoine Lamaree, who would respond to my calls (even on sunny weekend) and rush to the lab to fix the problems with laser.

My special thanks to Guy Lebrun, and all the technicians at machine shop, they always helped me to fix my small issues in their busy schedule.

INRS administration was a great helping hand throughout my stay at INRS. I appreciate the efforts of Nathalie Graveline, Helene Sabourin, Louise Hudon, and all who do their best to simplify the life of lazy student like me at INRS.

My husband Kanwarpal spent several nights at the couch at INRS cafeteria while I was performing experiments on weekends in ALLS. I am lucky to have him as he not only provided the scientific input to my work but also supported me morally throughout my PhD. My sincere gratitude towards my parents and my sister Shivani, for their encouragement throughout my life.

I am grateful to INRS and FQRNT for the financial support for my doctoral work.

Last but not least, I would like to thank the members of the review committee who took out time from their busy research life and reviewed my thesis.

Table of figures

Table of Contents

Chapter 1

Introduction and objectives

1.1 Introduction

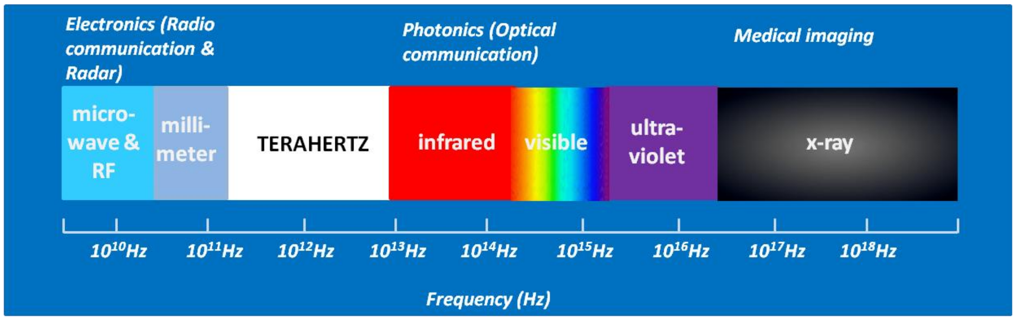

Figure 1. Electromagnetic spectrum

The complete electromagnetic spectrum can be roughly divided into different wavelength regions, as shown in Figure 1. In this spectrum, the terahertz (THz) frequency band lies between 0.1 and 10 THz, being one of the least explored region in the electromagnetic spectrum. Several important phenomena take place in this frequency range, making THz a field of substantial interest to the research community. For example, intermolecular vibrations of solid materials are observed at THz frequencies [1]. In biology, important collective modes of proteins vibrate at THz frequencies [2]. The rotational energy levels of small molecules also fall within the THz frequency range [3]. Rotation and collective modes cause polar liquids (such as water) to strongly absorb THz frequencies [4, 5]. Furthermore, in gaseous and solid plasma, the molecules oscillate at THz frequencies [6, 7]. Matter at temperature above 10 K emits blackbody radiation, which also falls within THz frequencies [8].

The fact that coherent detection techniques could be used makes coherent THz radiation a very important tool for studying the fundamental properties of various molecules. Further, THz frequencies also have a huge potential in imaging, offering several advantages over conventional imaging and spectroscopy techniques. For example, its low photon energy (4.1 meV) allows THz radiation to penetrate through many materials (such as wood or plastic) without photoionizing the molecule, unlike X-ray radiation. These two fundamental properties make THz technology a potential tool for several applications. This trend is presented well in the most cited publications in the field of THz, namely: THz spectroscopy [9, 10] and THz imaging [11, 12].

One of the most challenging scientific applications of high power terahertz waves is nonlinear spectroscopy. Using intense THz sources, it is now possible to study the nonlinear optical response of materials at THz frequencies and at picosecond (and even sub-picosecond) timescales. For example, a long-lived coherent THz emission (centered at around 2 THz), as well as a carrier-wave Rabi oscillations have been observed between bound impurity levels of n-type GaAs, excited by an intense THz pulse with peak electric field amplitude of 70 kV/cm [13, 14]. In addition, THz-intensity-dependent cross phase modulation has been observed in electro-optic crystals, in turn leading to spectral shifting, broadening and modulation of co-propagating laser pulses [15, 16]. Using intense THz pulses, there have been reports of lattice anharmonicity and self-phase modulation in $LiNbO_3$ [17], and THz-electric–field-induced impact ionization in InSb [18, 19]. Moreover, these sources have allowed the observation of a decrease in THz absorption due to intervalley scattering in doped InGaAs, GaAs, Si, and Ge using THz-pump / THz-probe techniques [19-21]. More recently, they have also enabled the detection of the Kerr effect at THz frequencies, resulting in a THz intensity dependent birefringence in liquids [22]. Intense THz fields are used to map the effective mass anisotropy in the non-parabolic conduction band of an InGaAs thin film [20]. There have also been studies on THz electro-optic modulation of excitons in carbon nanotubes [23], THz induced saturation absorption in semiconductors [24] and coherent control of antiferromagnetic spin waves [25].

In spite of the results mentioned above, the field of THz nonlinear spectroscopy is still at its preliminary stage. The best is still to come, the main limitation being the availability of high power THz sources. Not surprisingly, many researchers across the world are working on the development of intense THz sources to exploit this field of research.

1.2 Objective of the thesis

The main objective of this thesis is to develop an intense THz source and to use it to study the nonlinear THz response of semiconductors and graphene. This thesis is arranged as follows. First, the intense THz source developed using the tilted-pulse-front technique in a $LiNbO_3$ crystal is explained in Chapter 2. During the course of this thesis work, a novel technique for THz detection using spectral domain interferometry has been proposed and demonstrated, and the details of this technique are described in Chapter 3. Finally, the developed source is used to investigate the nonlinear response of various materials, and the results obtained are described in Chapter 4 and 5.

1.2.1 Intense THz source development

The Advanced Laser Light Source (ALLS) facility, located at the Varennes, Québec campus of the INRS, is one of the leading facilities for intense THz research. The THz group at ALLS has successfully demonstrated the generation of high-power THz radiation using optical rectification in a large aperture zinc telluride crystal [26]. This source uses ~50 mJ of laser energy as the pump, resulting in a peak THz electric field as high as 200 kV/cm. Such high electric field is good for observing nonlinear THz phenomena in various materials. The main limitation of this THz source is the signal-to-noise ratio, since the laser used to pump this source has a repetition rate of 100 Hz, and the pulse-to-pulse fluctuations could be as high as 10 %. In general, the electric field strength of this source is already close to the threshold for observing nonlinear THz response in many materials, and the low signal-to-noise ratio increases the experimental challenges significantly. One way to increase the signal-to-noise ratio is to increase the generated THz electric field or energy. With the current technique, crystals with larger size and higher pump laser energies are required, leading to unpractical set-ups.

Recently, a new technique has been proposed to generate intense THz sources: optical rectification pumping a $LiNbO_3$ crystal with the tilted-pulse-front method. To date, this is arguably the most efficient way to generate THz radiation, with an efficiency as high as $\sim 10^{-3}$. One of my first tasks was to demonstrate this source at ALLS using a relatively low power laser system, providing 4 mJ of laser energy at

1 kHz repetition rate and 40 fs pulse duration. The details of this source are discussed in Chapter 2.

1.2.2 THz detection using spectral domain interferometry

During the characterization of the intense THz source mentioned above, we experienced the problem of detecting intense THz electric field. The conventional method for THz detection is electro-optic sampling. It is a commonly used method but has many limitations when it comes to detecting intense THz electric fields, including the problem of over-rotation. In Chapter 3, we describe a novel technique based on modified electro-optic sampling using spectral domain interferometry for THz detection. This technique enables us to detect intense THz electric field without the limitation of over-rotation.

1.2.3 Nonlinear THz spectroscopy

The next objective of this thesis was to study nonlinear THz spectroscopy of various materials.

1.2.3.1 Semiconductors

Chapter 4 is dedicated to the nonlinear experiments performed on semiconductors. We have investigated the optical-pump / THz-probe spectroscopy of GaAs samples. In these experiments, the THz probe is the intense THz pulse, so it is not only probing but also pumping the GaAs sample. Here, we observed THz-pulse-induced intervalley scattering, resulting in absorption bleaching of the intense THz pulse.

Next, the effect of optical pump fluence on THz-induced absorption bleaching is investigated. It is observed that the carrier density in the conduction band of the semiconductor strongly affects this phenomenon.

The results are modeled using an intervalley-scattering-based Drude model. This simple model gives reasonable agreement with our experimental observation.

1.2.3.2 Graphene

In Chapter 5 of this thesis, some of our experimental results recently obtained with graphene are discussed. Graphene is one of the most exciting materials currently investigated, because of its many unique properties, including high mobility and the possibility of frequency multiplication at THz frequencies, as shown by our recent experimental results.

Chapter 2

Intense THz generation via tilted-pulse-front technique in $LiNbO_3$ crystal

2.1 Introduction

To be able to investigate the nonlinear response of materials at THz frequencies, one requires intense THz sources with high electric field strengths. In this chapter, the intense THz source using the tilted-pulse-front technique in $LiNbO_3$ crystal is discussed, designed and demonstrated, as a first step towards nonlinear THz spectroscopy.

2.2 Optical rectification for THz generation

Optical rectification (OR) is a second-order nonlinear optical process in which, following the application of an intense laser field, a quasi dc polarization is induced in an electro-optic crystal due to difference frequency generation. This effect was first observed in 1962 by M, Bass *et al.*, by using Ruby lasers in a KDP crystal [27]. If the incident laser pulses have femtosecond duration, then the difference-frequency generation between the various frequency components of a broadband femtosecond laser pulse gives rise to broadband THz radiations. Although it has been known for a long time that the emission of radiation in the far-infrared can result from the optical rectification of an optical pulse [28], experimental and theoretical evidence of rectification in (110) crystal semiconductors was only demonstrated in 1994 by Rice *et al.* [29].

The other conventional way to generate THz radiations is the photoconductive antenna, where the femtosecond laser pulse excites the electrons in the conduction band of the semiconductor, and the subsequent acceleration of carriers due to the applied voltage gives rise to emission of radiation. If the lifetime of the carrier lies within the picosecond range, THz radiation is generated.

Optical rectification is a more popular choice for THz pulse generation when working with amplified lasers, because the pump laser intensity threshold for saturation is much higher than that in photoconductive antennas [30-35]. On the other hand, THz generation by non-resonant optical rectification has the unique advantage of an extremely broad spectral bandwidth [36], compared to photoconductive antenna THz generators, when pumped with sub 100 femtosecond laser pulses. The mathematical formulation of the theory of THz generation is discussed further.

Mathematically, the polarization P can be expanded into a power series of the electric field E_{opt},

$$\vec{P}(t)=\chi^{(1)}(t)\vec{E}_{opt}(t)+\chi^{(2)}(t)\vec{E}_{opt}(t)\vec{E}_{opt}(t)+\chi^{(3)}(t)\vec{E}_{opt}(t)\vec{E}_{opt}(t)\vec{E}_{opt}(t)+\ldots \tag{2.1}$$

where $\chi^{(n)}$ is the n^{th} order nonlinear susceptibility tensor. The second term in Eq. (2.1) is responsible for the optical rectification process; This is the result of noncentrosymmetric nature of the nonlinear crystal, which induces optical rectification . If the incident light is a plane wave, then it can be expressed as,

$$\vec{E}_{opt}(t)=\int_0^{\infty}\vec{E}_{opt}(\omega)exp(-i\omega t)d\omega+cc. \tag{2.2}$$

By substituting Eq. (2.2) into Eq. (2.1), the polarization for the optical rectification can be rewritten as,

$$\vec{P}_{OR}^{(2)}(t)=2\chi^{(2)}\int_{-\infty}^{\infty}\int_{-\infty}^{\infty}\vec{E}_{opt}(\omega_1)\vec{E}_{opt}^{*}(\omega_2)\exp[-i(\omega_1\pm\omega_2)t]d\omega_1 d\omega_2 \tag{2.3}$$

Here, $\omega_1=\omega+\Omega$ and $\omega_2=\omega$, where Ω is the difference between the various frequency components of the broadband laser pulse. On substituting these values in to Eq. (2.3), one gets:

$$\vec{P}_{OR}^{(2)}(t)=2\chi^{(2)}\int_0^{\infty}\int_0^{\infty}\vec{E}_{opt}(\omega+\Omega)\vec{E}_{opt}^{*}(\omega)\exp[-i\Omega t]d\omega d\Omega \tag{2.4}$$

In the far field, the radiated electric field $E_{THz}(t)$ is proportional to the second order derivative of the induced polarization with respect to time.

$$\vec{E}_{THz}(t) \propto \frac{\partial^2}{\partial t^2}\vec{P}_{OR}^{(2)}(t) \tag{2.5}$$

The susceptibility tensor is the property of the nonlinear crystal structure. Thus, by knowing the crystal structure and the incident light, Eq. (2.5) can be used to calculate the far-field waveform of the radiation.

The actual configuration for generating THz pulses via optical rectification is rather simple, as shown in Figure 2. As discussed above, when an intense laser beam propagates through a second order nonlinear medium, a transient polarization is induced, which results in the generation of THz radiation. The generated THz pulse is proportional to the second-order time derivative of this polarization [29, 37-40]

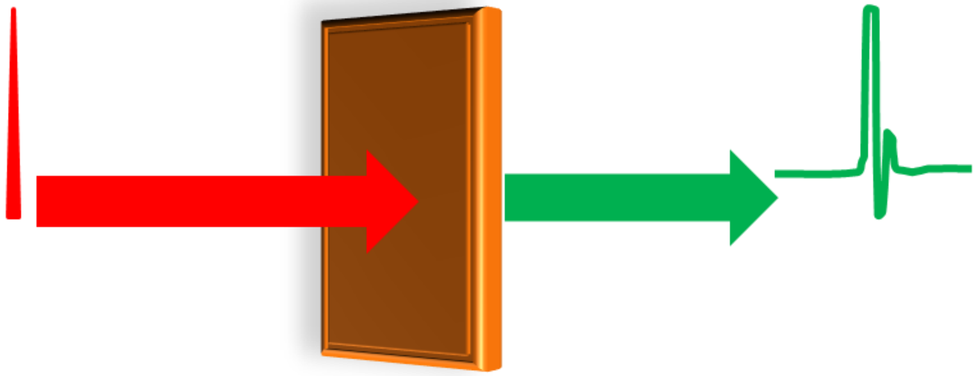

Figure 2. THz generation via optical rectification in a nonlinear crystal. A femtosecond laser pulse, passing through a $\chi^{(2)}$ material, generates a broadband THz pulse by means of difference frequency generation processes in between all the spectral components of the broadband optical pulse.

The efficiency, shape and frequency distribution of the radiated THz waveform depends on various factors, such as the materials used, crystal orientation, thickness, absorption and dispersion, diffraction, phase matching, and saturation. Although all of these factors affect the efficiency of THz generation, for a nonlinear process such as optical rectification, phase matching is the most important factor. For efficient transfer of energy from optical to THz radiation, the phase matching condition, which is given by the following equation, should be satisfied:

$$k(\omega+\Omega)-k(\omega)=k_{THz}(\Omega) \tag{2.6}$$

Here, k is the wave vector, ω is the angular frequency of the pump beam, and Ω is one particular frequency of the radiated THz wave packet. Using this expression, we may depict the radiated THz waves as the superposition of all the frequency components in the optical pump beam. Additionally, Ω depends on the second-order dispersion coefficient of the crystal, as well as on the pump beam spectrum and on the phase shift between the pump and the THz waves.

From Eq. (2.6) one can write,

$$\frac{\tilde{k}_{THz}}{\Omega}=\left[\frac{\partial\tilde{k}}{\partial\omega}\right]_{opt} \tag{2.7}$$

Eq. (2.7) gives the phase matching condition for efficient THz generation from the optical pulse. This states that the group velocity of the optical wave should match the phase velocity of the THz wave [33]. Eq. (2.7) is the condition for collinear phase matching, where the optical and THz wave propagates collinearly through the nonlinear medium. The phase matching condition is satisfied only when the participating waves are in phase with each other. This leads to maximum conversion of energy along the propagation of the optical wave through the nonlinear medium. Phase mismatch leads to a phase walk-off as the optical wave propagates through the medium. When the phase difference between the optical and the THz pulse is more than π, there will not be any energy transfer between the two. The length for which the phase difference between the optical and the THz pulse changes by π inside the nonlinear medium is known as the coherence length of the crystal [39].

$$\Delta k L_c = \pi \tag{2.8}$$

Here $\Delta k = k(\omega+\Omega) - k(\omega) - k_{THz}(\Omega)$. In order to generate efficient THz radiation from a bulk crystal, the thickness of the crystal cannot be longer than the coherence length, in order to avoid the conversion cancellation due to phase mismatch.

2.3 THz detection using free space electro-optic sampling

Free-space electro-optic detection uses the linear Pockels effect in an electro-optic (EO) crystal to detect the quasi-DC electric field of the THz pulse with respect to a femtosecond gating pulse. This technique was first demonstrated in 1996, by X.-C. Zhang's group [41], the group of P. Jepsen and M. Helm [42] and finally, the group of T.F. Heinz [38]. A schematic diagram of this technique is shown in Figure 3.

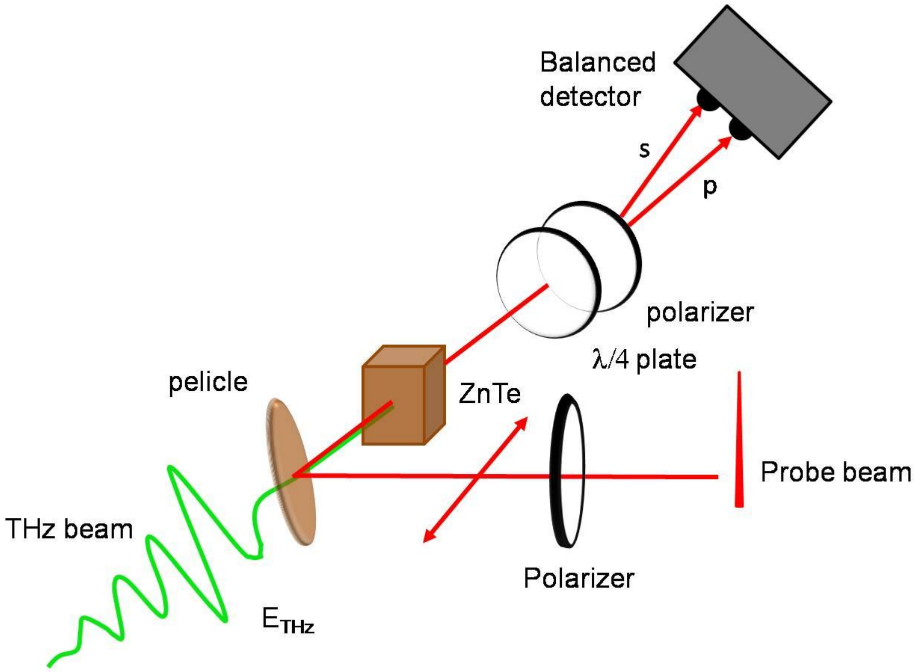

Figure 3. THz detection using electro-optic sampling technique using a ZnTe crystal (see text below for a description of the technique)

In the absence of the THz field, a linearly polarized gating pulse traverses a ZnTe crystal and passes through a $\lambda/4$ waveplate unaffected and becomes circularly polarized. The orthogonal polarization components of the gating pulse are then equally separated by a Wollaston prism, and each is sent to one of the photodiodes of a balanced two-photodiode detector. Since the pulse is circularly polarized, each photodiode reads the same voltage, which is sent to a lock-in amplifier, subtracts the two and returns a zero reading. When the THz field overlaps the gating pulse in time, the polarization of the gating beam is rotated slightly by an amount proportional to the strength of the electric field (Pockels effect). In this case, after the $\lambda/4$ plate, the polarization is elliptically polarized and after separation by the Wollaston polarizer, there is an imbalance between the signals of the two photodiodes, registered by a lock-in as a signal proportional to the subtraction of the two components. Such signal is directly proportional to the electric field of the THz pulse, and by scanning the time delay between the gating beam and THz beam, the entire THz waveform may be mapped in time. The lock-in amplifier is locked to the frequency of an optical chopper, which modulates the THz source beam at, e.g., 500 Hz for a 1kHz repetition rate laser system. Conventionally for EO sampling ZnTe crystal is used, although crystals like GaSe, GaP, InP, GaAs and DAST have also been demonstrated [43-45]. A detailed study on the crystal orientation dependence of the THz detection in ZnTe is given in Ref. [46]. Because the nonlinear optical rectification process is instantaneous, one would assume that the bandwidth is only limited by the sampling pulse duration. However, the detection bandwidth is fundamentally limited by the phase mismatch between the THz pulse and the 800 nm detection pulse due to a difference in the refractive index at these two wavelengths [38]. Very thin ZnTe crystals, which minimize the influence of this phase mismatch, have been used to extend the detection bandwidth to 100 THz, using sub ten femtosecond pulses [47]. Other sources that limit bandwidth are absorptive phonons at 1.6 and 3.7 THz in ZnTe [48], as well as a transverse optical (TO) phonon at 5.31 THz [41].

For a zinc blend crystal, such as ZnTe, when an electric field is applied, the refractive index ellipsoid is given by:

$$\frac{x^2+y^2+z^2}{n_0^2}+2r_{41}E_x yz+2r_{41}E_y zx+2r_{41}E_z xy=1 \tag{2.9}$$

where n_0 is the refractive index of the crystal without the electric field, *x*, *y*, *z* are the coordinates of the ellipsoid and E_x, E_y, E_z, are the applied electric fields along the corresponding axes, respectively. r_{14} is the EO coefficient of the crystal. A phase delay ϕ (the retardation introduced in the wave due to the applied electric field) can be calculated according to the change in the refractive index.

$$\phi = \frac{2\pi d}{\lambda} \Delta n \tag{2.10}$$

Here, *d* is the thickness of the EO crystal and Δn is the difference of the refractive index for the two axes. Here the process is assumed to be phase matched. If only normal incidence is considered, and if the THz electric field E makes an angle θ with the X axis (-110) of the ZnTe crystal, then the phase delay in (100), (110) and (111) oriented ZnTe crystal is

$$\phi = 0 \qquad [\mathit{for}\ (100)\ \mathit{crystal}] \tag{2.11}$$

$$\phi = \frac{\pi d n_0^3 r_{41} E}{\lambda} \sqrt{1 + 3\cos^2\theta} \qquad [\text{for (110) crystal}] \tag{2.12}$$

$$\phi = \frac{\pi d n_0^3 r_{41} E}{\lambda} \sqrt{\frac{8}{3}} \qquad [\mathit{for}\ (111)\ \mathit{crystal}] \tag{2.13}$$

For (110) ZnTe crystal, if $\phi \ll 1$, then the measured signal is given by

$$I = I_0\left(\sin 2\theta \sin\frac{\phi}{2}\right)^2 \approx \frac{1}{4} I_0 \phi^2 \sin^2 2\theta \tag{2.14}$$

However, in reality, the EO crystal is not perfectly homogeneous, thus inducing a phase delay ϕ_0 , Eq. (2.14) then becomes:

$$I \approx \frac{1}{4} I_0 (\phi + \phi_0)^2 \sin^2 2\theta \tag{2.15}$$

If $\phi_0 \gg \phi$, then Eq. (2.15) becomes

$$\Delta I \approx \frac{1}{2} I_0 \phi \phi_0 \sin^2 2\theta \tag{2.16}$$

Here, ΔI represents the signal difference (or gain) with and without the presence of the THz field. As a note, since this technique is very sensitive, it is good to extract the electric field information only if the modulation between the two polarization components of the probe pulse is small. If the modulation is high, the approximation $\sin\phi \approx \phi$ is not valid anymore, in turn inducing inaccuracies in the electric field evaluation. For the THz electric field greater than few tens of kV/cm, the EO sampling is used only to extract the temporal shape of the THz pulse.

2.4 Intense THz generation via optical rectification method

2.4.1 Choice of material for optical rectification

Various materials have been studied for efficient THz generation by optical rectification. THz generation by optical rectification can be mathematically expressed as a difference frequency generation in a second order nonlinear crystal. When phase matching is achieved, the efficiency of THz generation in a nonlinear medium in the absence of pump absorption is given by:

$$\eta_{THz} = \frac{2\Omega^2 d_{eff}^2 L^2 I}{\varepsilon_0 \left(n_{opt}^{gr}\right)^2 n_{THz}^{ph} c^2} \exp\left[-\frac{\alpha_{THz} L}{2}\right] \frac{\sin^2\left[\alpha_{THz}\left(L/4\right)\right]}{\left[\alpha_{THz}\left(L/4\right)\right]^2} \tag{2.17}$$

where η_{THz} is the THz generation efficiency, Ω is the difference (THz) frequency, d_{eff} is the effective nonlinear coefficient, I is the intensity of the input laser pulse, ε_0 is the free space permittivity, c is the velocity of the light, L is the length of nonlinear crystal, α_{THz} is the intensity absorption coefficient of the THz radiation in the crystal, n_{opt}^{gr} and n_{THz}^{ph} are the group and phase refractive index for an optical and a THz beam, respectively. If the absorption $\alpha_{THz} L << 1$, Eq. (2.17) can be simplified as:

$$\eta_{THz} = \frac{2\Omega^2 d_{eff}^2 L^2 I}{\varepsilon_0 \left(n_{opt}^{gr}\right)^2 n_{THz}^{ph} c^2} \tag{2.18}$$

If THz absorption is very high inside the nonlinear crystal, that is $\alpha_{THz}L >> 1$ Eq. (2.17) can be rewritten as:

$$\eta_{THz} = \frac{32\Omega^2 d_{eff}^2 I}{\varepsilon_0 \left(n_{opt}^{gr}\right)^2 n_{THz}^{ph} c^2 \alpha_{THz}^2} \exp\left[-\frac{\alpha_{THz} L}{2}\right] \tag{2.19}$$

From Eqs (2.18) and (2.19), it is clear that it is useful to increase the crystal length only below the penetration depth of the THz radiation α_{THz}^{-1}. Only those photons that are produced within the region $L_{eff} = \alpha_{THz}^{-1}$ will exit the surface of the crystal and can significantly contribute to THz emission. The other determining factor in choosing the crystal thickness is the dispersion of the optical pump pulse and the THz pulse inside the nonlinear medium. For example, for a 100 fs optical pulse, the crystal thickness is limited to 1-2 mm. Various crystals have been investigated for generating THz radiation using optical rectification. The different parameters contributing to THz generation by optical rectification in various crystals are shown in Table 1.

Table 1. Comparison of different materials for THz generation via optical rectification[49]

Material	**Group index for 800nm**	**Phase index for THz**	**Electro-optic coefficient r(pm/V)**	**Absorption coefficient (α_{THz})**
CdTe	3.73	3.23	4.5	4.8
GaAs	4.18	3.61	1.43	0.5
GaP	3.57	3.34	0.97	1.9
ZnTe	3.31	3.17	4.04	1.3
GaSe	3.13	3.72	1.7	0.07
$LiTaO_3$	2.22	6.42	30.5	46

$sLiNbO_3$	2.23	5.16	30.9	16
DAST	3.31	2.4	77	150

Table 1 shows the important properties of various materials for THz generation via optical rectification. At room temperature, DAST has the highest electro-optic coefficient. DAST has been used recently to generate THz pulses with a 50 kV/cm focused field strength [50-52]. However, this material is not commonly used for intense THz generation because it is very fragile, and present strong absorption at 800 nm wavelength. CdTe has the fourth highest electro-optic coefficient, but there has been no report of its use for THz generation via optical rectification yet. One possible reason could be that CdTe is strongly absorbing at the 800 nm output of Ti:sapphire lasers [38, 53]. ZnTe is the most commonly used electro-optic crystal for optical rectification and electro-optic sampling, even if the electro-optic coefficient for ZnTe is only the fifth largest in Table 1. ZnTe is used widely because of the collinear velocity matching between the pump pulse and the THz radiation, which is approximately fulfilled for Ti:sapphire laser pulses.

However, it is important to notice that $sLiNbO_3$ (sLN) has the second highest electro-optic coefficient, its value being more than seven times larger than that of ZnTe. The energy of the THz pulses (even at room temperature) generated using $sLiNbO_3$ is orders of magnitude higher [54] than that for ZnTe for the same pump energy. The other advantage of sLN crystal is that much higher pump laser energy can be used, as compared to other materials. One reason for this is that the relatively small band gap of many semiconductors allows two-photon absorption of the pump pulses at 800 nm [40, 55-57]. However, the band gap of sLN is significantly higher [58, 59] than other materials, which restricts two-photon absorption at 800 nm. This results in much higher THz pulse energy generation and higher conversion efficiency. The problem with sLN is the strong THz absorption due to the carriers created by two-photon absorption.

Even though the electro-optic coefficient of sLN is very high, this crystal was not commonly used for THz generation prior to 2007. The main reason for this was the phase mismatch between the group velocity of the optical pulse and the phase velocity of the THz pulse given by Eq. (2.7). From table 1, the group index of the optical pump pulse is lower than the phase index of THz pulse. Mathematically, one can write $n_{THz}^{ph} > n_{opt}^{gr}$. To efficiently generate THz radiation via optical rectification, the two indices should match, that is $n_{THz}^{ph} = n_{opt}^{gr}$. In collinear geometry, the phase matching condition in LN can be achieved by quasi phase matching (QPM) in periodically poled lithium niobate (PPLN). Multi-cycle narrow-band THz radiation has been generated in PPLN [55, 60]. To generate a single-cycle THz pulse, one needs to use non-collinear phase matching condition. In particular, nonlinear phase matching condition in sLN can be achieved by the techniques detailed below.

2.4.2 Cherenkov scheme

A schematic diagram showing the mechanism of the Cherenkov scheme is shown in Figure 4. Here, THz radiation is generated by optical rectification if the group velocity of the optical pump pulse exceeds the phase velocity of the THz pulse. In an electro-optic crystal like sLN, this condition is easily fulfilled [61]. As can be seen from Figure 4, the Cherenkov radiation is emitted in the form of a cone.

The angle of the cone can be determined by the ratio between the group refractive index of the optical pulse and the phase refractive index of the THz pulses, given by the following expression

$$\theta_c = cos^{-1}\left(\frac{n_{opt}^{gr}}{n_{THz}^{ph}}\right) \tag{2.20}$$

For instance, if we consider sLN, the group index of the optical pump at 800nm wavelength is 2.25, and the phase index for the THz pulse is 4.95, which results in a Cherenkov angle $\theta_c \approx 63^0$.

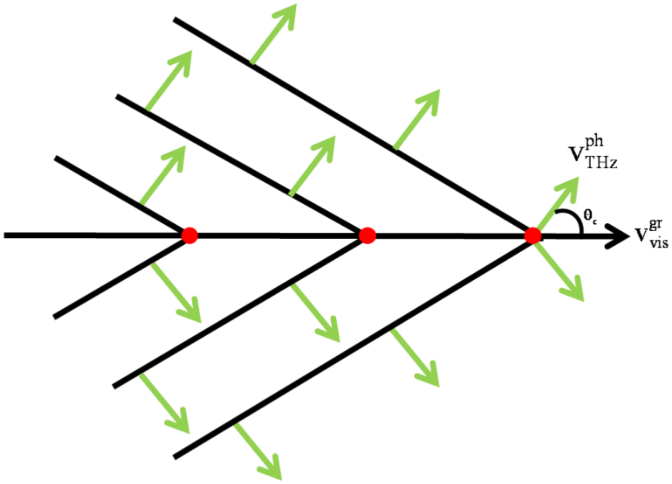

Figure 4. THz generation by Cherenkov radiation. Here v_{opt}^{gr} is the group velocity of the optical pulse and v_{THz}^{ph} is the phase velocity of the generated THz radiation. Phase matching condition is achieved at the critical angle θ_c, which also determines the THz generation angle given with respect to the propagation direction of the optical beam.

THz radiations can only be generated via the electro-optic Cherenkov effect if the beam waist (w_0) of the optical pump beam is considerably smaller than the axial spread of the beam:

$$w_0 << \frac{c}{n_{opt}^{gr}} \tau_{opt} \qquad (2.21)$$

Here τ_{opt} is the optical pulse duration of the optical beam, which has to be significantly shorter than the generated THz radiation [61, 62].

The Cherenkov scheme was demonstrated initially to allow THz generation in an electro-optic crystal where the group velocity of the optical pulse is greater than the phase velocity of the THz radiation [61, 63]. However, this method has not been used for efficient THz generation. There are two main reasons for this; (i) the THz radiation is generated in a cone shape, which makes it difficult to collect the generated radiation for the purpose of possible applications. (ii) The spot size of the optical pump beam should be small, following Eq. (2.21). Therefore, the THz generation efficiency cannot be increased by using larger optical pump spot size, because the radiated energy strongly drops when the beam waist approaches the axial spread of the pulse inside the electro-optic crystal. Due to the limited spot size of the optical pump laser, the maximum pump energy that can be used to generate THz radiation is strongly limited by the damage threshold of the material. [61]

2.4.3 Tilted-pulse-front technique

In 2002, Hebling *et al.* proposed a very efficient method to generate intense THz radiation [64], which was subsequently demonstrated by the same group [49, 65]. The technique involves tilting the pulse front of the optical pump, to match the group velocity of the optical pulse with the phase velocity of the THz pulse. The mechanism of the tilted-pulse-front technique is described in Figure 5.

The pulse front tilt is realized by tilting the pulse front of the optical beam with respect to phase front, which were initially perpendicular to the direction of propagation of the optical beam. THz radiation is excited along this tilted pulse front direction. The pump pulse propagates with a velocity v_{vis}^{gr}, but the projection of this velocity in the direction of propagation of the generated THz is $v_{vis}^{gr}.cos\theta_c$. Here, θ_c is the tilt angle introduced in order to match the group and phase velocities of the THz and optical pulse respectively. Thus, the phase matching condition in this case will be given by

$$v_{vis}^{gr}.\cos\theta_c = v_{THz}^{ph} \tag{2.22}$$

Using this scheme, it is possible to match the two velocities by choosing an appropriate tilt angle θ_c, in a material with significantly large dielectric constant.

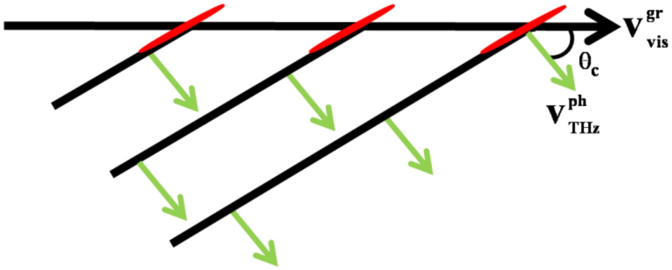

Figure 5. Coherent THz generation in tilted-pulse-front geometry. In this process, the phase mismatch between the optical and THz waves is overcome by tilting the pulse front of the optical wave, thereby resulting in a new phase matching condition: $v_{opt}^{gr}cos\theta_c = v_{THz}^{ph}$. Due to this phase matching, unlike the Cherenkov mechanism, all the generated THz radiations are in phase with each other.

2.4.3.1 Pulse front tilt introduced by a grating

In order to tilt the pulse front of the optical beam with respect to the phase front, a grating is typically used. The typical method to tilt the pulse front using a grating is shown in Figure 6. Using simple ray optics formulation for an optical beam that is incident on the grating with an angle α and is diffracted by an angle β, the pulse front tilt angle θ_c is given by the following expressions:

$$\tan\theta_c = \tan\beta + \frac{\sin\alpha}{\cos\beta} \tag{2.23}$$

This equation can be rewritten as

$$\tan\theta_c = \frac{\sin\alpha + \sin\beta}{\cos\beta} \tag{2.24}$$

By using the grating equation $\sin\alpha + \sin\beta = mN\lambda$, where α and β are the angle of incidence and diffraction, respectively, m is the order of diffraction, N is the number of grooves per millimeter of the grating, and λ is the wavelength of the optical beam, the pulse front tilt angle is given by:

$$\tan\theta_c = \frac{mN\lambda}{\cos\beta} \tag{2.25}$$

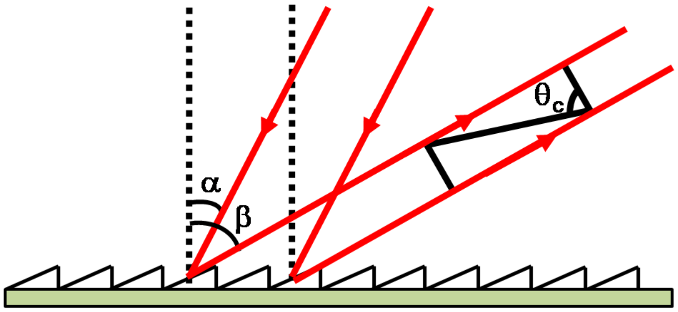

Figure 6. An optical beam incident on the grating (at an angle *α*)with a pulse front and phase front perpendicular to the direction of propagation of the beam. After diffraction (at an angle *β*) the pulse front of the grating is tilted by an angle θ_c .

The optical beam diffracted from the grating will diverge according to the bandwidth of the laser. In order to collect the beam and to achieve higher intensity at the crystal position, a lens is used, as shown in Figure 7, to image the optical beam on to the crystal position (d_i) with a certain demagnification with respect to the spot size at the grating position (d_0). This demagnification ($F=d_o/d_i=S_o/S_i$, where S_o and S_i is the object and image distance in the one-lens configuration) will increase the tilt introduced by the grating by a factor F, so the tilt equation will be :

$$\tan\theta_c = \frac{FmN\lambda}{\cos\beta} \qquad (2.26)$$

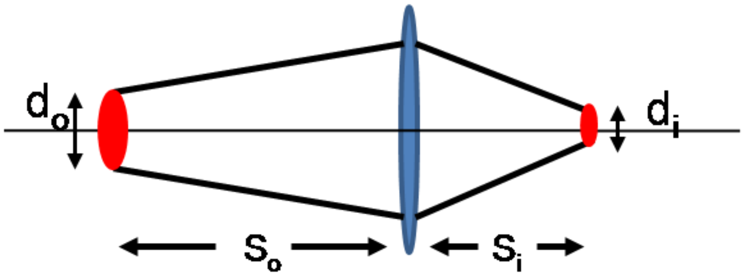

Figure 7. Imaging of the laser beam spot with a demagnification of $F=S_o/S_i$, where S_o and S_i are the object and image distance respectively.

Eq. (2.26) is for a beam propagating in air, but for THz generation, the beam must propagate inside the $LiNbO_3$ crystal, and thus the index of refraction of the crystal will also play a role in the pulse front tilt. If n_{opt} is the index of refraction for the optical beam inside the crystal, then the pulse front tilt equation will be:

$$\tan\theta_c = \frac{F}{n_{opt}} \frac{mN\lambda}{\cos(\beta)} \tag{2.27}$$

From this equation, the angle of diffraction is given by:

$$\beta = \cos^{-1}\left(\frac{F}{n_{opt}} \frac{mN\lambda}{\tan\theta_c}\right) \tag{2.28}$$

Using the grating equation, the angle of incidence of the input beam can be determined by:

$$\alpha = \sin^{-1}\left(mN\lambda - \sin\left(\cos^{-1}\left(\frac{F}{n_{opt}} \frac{mN\lambda}{\tan\theta_c} \right)\right)\right) \qquad (2.29)$$

If the optical pump beam is incident onto the grating, with an angle of incidence α given by the above equation, the required pulse front tilt for the phase matching condition in the sLN crystal will be introduced into the optical beam.

2.4.3.2 Optimization of the pulse-front-tilting setup

In order to obtain optimal pump-to-THz conversion in a tilted pulse front setup, the following conditions have to be fulfilled:

1. Velocity matching of the pump and the THz radiation require a certain tilt angle θ_c of the pump pulse front inside the crystal, given by Eq. (2.27)
2. The pump pulse duration has to be minimal across the tilted pulse front.
3. The pump pulse front has to be flat within the crystal.

2.4.3.3 Description of the sLiNbO$_3$ crystal used to implement the tilted pulse front technique

The crystal used in our experiment is a 1mol% Mg doped LiNbO$_3$ crystal. The optical properties of the LN crystals are improved by Mg doping. In Mg doped sLN crystal, the photorefractive losses are found to be dominant [66]. In order to fulfill the velocity matching condition, the crystal is cut at 63^0, which is determined by the group index of the optical beam and the phase index of the THz beam inside the crystal. In our case, their values are 2.25 [49] and 4.95 [67], respectively. The top view of the crystal is shown in Figure 8.

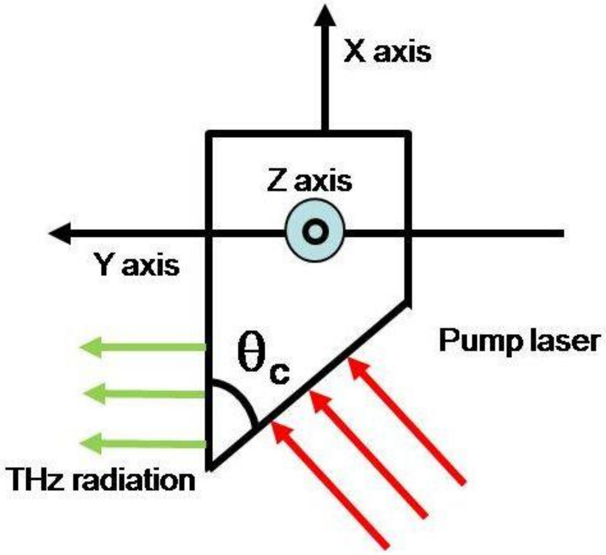

Figure 8. Top view of the sLN crystal. The crystal is cut at the phase matching angle θ_c . THz radiations will be generated (green arrow lines), when an optical beam (red arrow lines) is incident on to the crystal with a pulse front tilt angle of θ_c , so that the phase matching condition is satisfied.

2.4.3.4 Experimental set-up

For developing this source, the kHz Ti:sapphire laser available in the ALLS laboratory at the INRS campus in Varennes is used. This laser delivers 4 mJ laser pulses with 30 fs pulse duration at 1 kHz repetition rate and with a wavelength of 800 nm. The diameter of the optical beam is 5 mm. The layout of the experimental set up is shown in Figure 9.

.

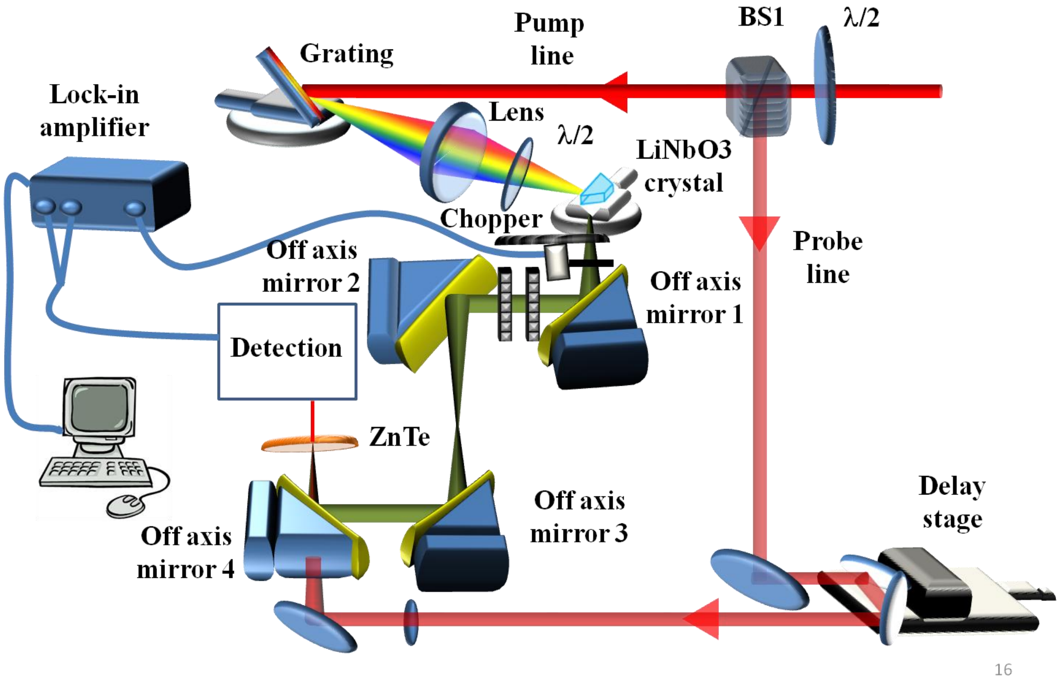

Figure 9. Experimental set up layout. The input laser is split between the pump and the probe beam using beam splitter BS1. The pump beam is used to generate THz using tilted pulse front method in LiNbO3 crystal. The generated THz is steered using four off axis mirror and focused at the ZnTe crystal. The probe beam is used to detect the generated THz via electro optic sampling technique. The THz signal is measured using lock-in amplifier and computer.

The pump beam is split into two parts using a combination of a half wave plate and a polarizing beam splitter BS1. The horizontally polarized beam is first demagnified by a factor of 2 by using a telescope made of two lenses with focal lengths of 200 mm and -100 mm, respectively. This demagnification is required to increase the pump laser intensity at the crystal position. This demagnified, p-polarized beam is sent to the grating (which is more efficient for p-polarization). The s-polarized beam is sent to the detection side (probe line). The pump beam is incident onto the grating with an angle of incidence of 37.31°, determined by Eq. (2.27). The pump beam diffracted from the grating is imaged onto the crystal with a demagnification of 1.7, using a lens with a focal length of 75 mm. After the lens, a half wave plate is placed between the lens and the crystal, in order to rotate the polarization of the pump beam from horizontal to vertical, resulting in the polarization of the pump laser parallel to the z-axis. THz radiation is generated from the crystal and is collected by the gold-coated off axis parabolic mirror. The THz beam is focused on to the 0.5-mm-thick ZnTe detector crystal using an off-axis mirror. In order to maintain the linearity of the detection, the THz electric field is reduced at the ZnTe crystal using wire-grid polarizer and silicon wafers. Free-space electro-optic (EO) sampling is used for the detection of the THz signal [46].

2.4.3.5 Source characterization

A. Energy measurement:

Our first measurement was done to investigate the efficiency of THz generation using the tilted-pulse-front technique in an sLN crystal. For this purpose, the THz energy is measured using a pyroelectric detector (Coherent

Molectron J4–05). Figure 10 shows the dependence of the THz electric field on the optical pump energy. The maximum energy is measured to be 0.6 μJ, with an input pump power of 0.9 mJ at the sLN crystal surface. This results in a maximum conversion efficiency of 6×10^{-4}. In an optical rectification (OR) process, one would expect the THz pulse energy to increase quadratically with the incident pump fluence. Instead, it is clear from Figure 10 that the process is partially saturated, thus resulting in a linear increase of the THz energy as a function of the laser pump energy. In the present configuration, the pump energy could not be further increased, to avoid damage of the grating. As such, we did not reach the complete saturation regime.

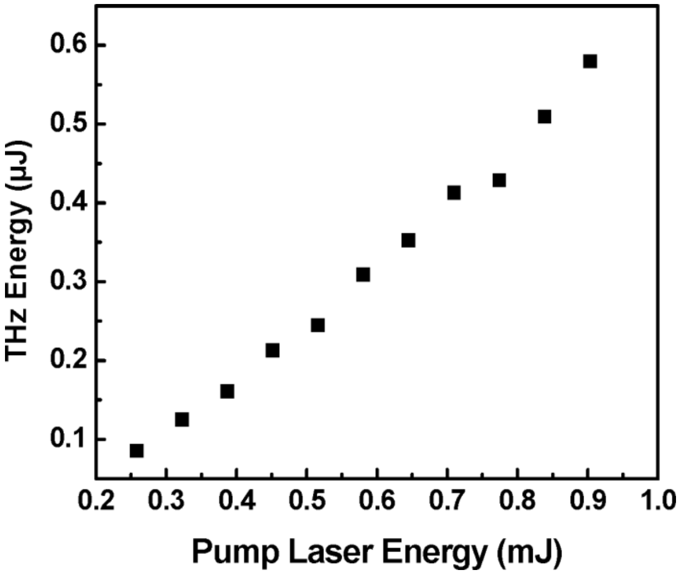

Figure 10. THz energy as a function of optical pump energy. The THz energy is measured using pyroelectric detector (Coherent Molectron J4–05).

B. THz spot size measurements

In order to complete the evaluation of the source, we imaged the THz beam at the focus using a pyroelectric IR camera (ElectroPhysics, model PV320). In this way, we could evaluate easily the peak electric field using the full characteristics of the beam, specifically the energy and physical dimensions of the THz beam at the focus. Recently, we have been able to capture the image of the THz beam using a $BaSrTiO_3$ (BST) pyroelectric infrared camera (Electrophysics model PV320-L2V). This camera operates with an internal 10 Hz chopper and has a 320 × 240 pixel imaging array, with a pixel spacing of 48.5 μm, with a spectral response between 7 to 14 μm. This camera shows the possibility of imaging high-power THz beams directly and in real time [26]. In Figure 11, we show the image of the THz beam at focus, which is used to estimate the electric field. The measured spot size is 0.8×0.7 mm^2 at $1/e^2$ of the intensity profile.

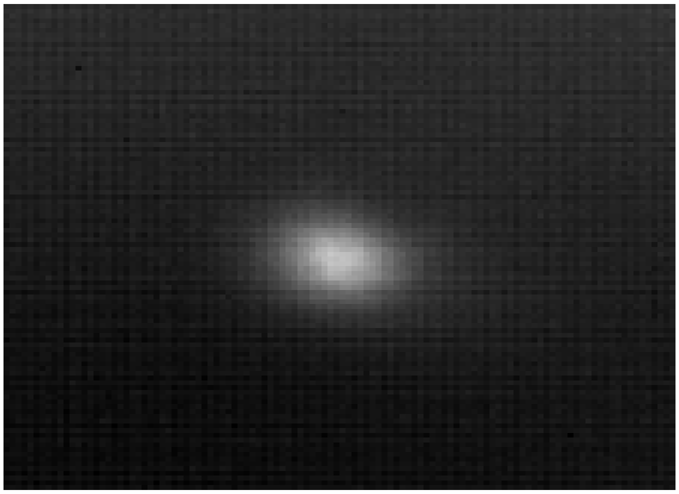

Figure 11. Image of a focused 0.6 μJ THz pulse generated using a 0.5-mm-thick ZnTe crystal. The measurement is done using pyroelectric infrared camera (Electrophysics model PV320-L2V)

C. THz pulse shape measurement

The temporal shape of the THz pulse is measured using the EO sampling method previously discussed in section 2.3. Figure 12 shows the THz pulse shape, and the inset shows the Fourier spectrum corresponding to this temporal profile.

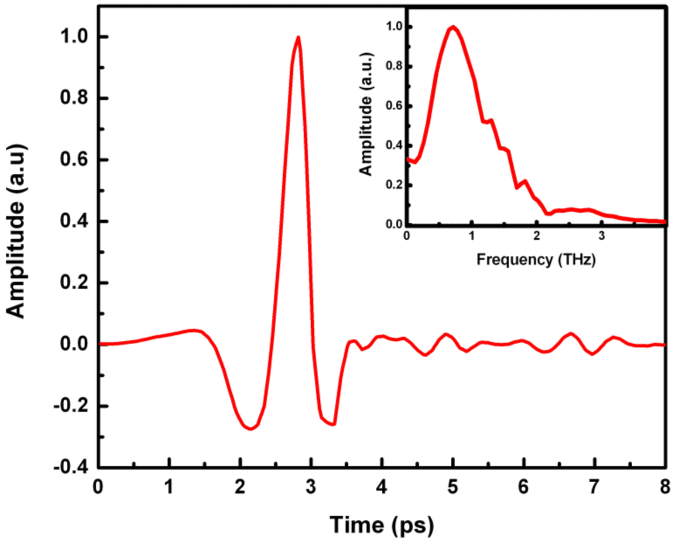

Figure 12. Temporal shape of the THz pulse measured using electro optic sampling. Inset shows the corresponding spectrum.

We have evaluated the THz electric field, following the same method as reported in [68], *i.e.* by using the following expression

$$E_0 = \sqrt{\frac{\eta_0 W}{\pi w_{opt}^2 \int g^2(t)\,dt}} \tag{2.30}$$

Here, E_0 is the THz peak electric field, η_0 is the free-space impedance (377 ohms), W is the THz energy, w_{opt} is the intensity beam waist, and $g(t)$ is the temporal shape of the THz electric field (with a peak value normalized to 1), which can be easily retrieved from the EO sampling measurements.

Knowing the THz spot size, the temporal profile of the THz pulse (measured from EO sampling), and the THz energy measured from the pyroelectric detector and substituting all these values in to Eq. (2.30), the THz electric field can be evaluated. For our LN THz source, we evaluate a peak THz electric field at the focus of the ZnTe detector position of $\sim 160\mathrm{kV/cm}$.

2.5 Comparison of the tilted pulse front $LiNbO_3$ THz source with the large aperture ZnTe THz source

We have compared the tilted-pulse-front based $LiNbO_3$ THz source with another intense THz source available at ALLS [26] based on optical rectification in a large aperture ZnTe crystal. The ZnTe source uses a laser with ~60 mJ energy and at a repetition rate of 100 Hz. Table 2 gives the comparison of different parameters for the two sources. As can be seen from

Table 2, the efficiency of the tilted pulse front $LiNbO_3$ source is 30 times higher than the ZnTe source; this shows that the tilted-pulse-front technique is one of the most promising way to generate intense THz radiation, with 50 times less driving laser energies required for similar performances.

Table 2. Comparison of the tilted pulse front $LiNbO_3$and large aperture ZnTe source

Parameter	**$LiNbO_3$ source**	**ZnTe source**
Electric Field	200kV/cm	200kV/cm
Energy	0.6μJ	1μJ
Spot Size	0.97 × 0.8 mm	1.57 × 1.91 mm
Signal to Noise	of the order of 10^5	of the order of 10^3
Input pump laser (energy per pulse and repetition rate)	~1mJ (1 kHz laser)	~50mJ (100Hz laser)
Conversion efficiency	6×10^{-4}	2×10^{-5}

Chapter 3

THz detection using spectral domain interferometry

3.1 Introduction

As discussed in the previous chapter, for the EO detection of intense THz electric fields, we had to reduce the electric field at the detection crystal using wire-grid polarizers or several silicon wafers, in order to maintain the linearity of the detection.

In EO sampling, a linearly polarized femtosecond laser pulse co-propagates with a picosecond THz pulse in an EO crystal. The THz electric field induces birefringence in the crystal, which changes the polarization of the linearly co-propagating laser pulse. The change in the phase between the two polarization components of the probe beam (which is proportional to the THz electric field) can be measured by using two cross polarizers placed before and after the detection crystal. In this case, the phase change appears as a modulation in the intensity of the probe beam. The complete THz waveform can be reconstructed by scanning the probe pulse over the entire THz pulse.

To improve the performance of EO sampling, several refinements have been proposed. Such improved THz detection techniques include chirped pulse or spectral encoding techniques [27], cross correlation techniques [69], two dimensional THz pulse characterization techniques with dual echelons [70] and tilted wavefront detection techniques using a prism [71].

All the aforementioned EO-sampling-based techniques have used two cross polarizers to measure the THz electric field. However, with recent advances in high power THz generation techniques, the use of thicker crystals poses a big problem in terms of over-rotation. If the THz electric field is high enough to introduce a phase difference of more than 90°, this leads to a reversal in the intensity modulation of the detection beam, leading to ambiguities in the measured THz field [72]. This situation is termed as "over-rotation". Birefringence introduced in the EO crystal is proportional to both the THz electric field and the thickness of the crystal. One could in principle use thinner crystals to avoid over-rotation, but this is not desirable due to internal reflection. Moreover, the use of thin crystals reduces the signal-to-noise ratio (SNR) of the measured THz signal, due to the decrease in interaction length.

To overcome the limitation of over-rotation in the measurement of an intense THz signal, we propose a novel technique based on spectral domain interferometry (SDI). In this technique, instead of using two cross polarizers, we measured the change in the phase difference introduced in the probe beam due to the THz electric field. The suitability of spectral domain interferometry in measuring phase changes as small as few micro-radians has already been demonstrated by various groups [73]. This technique not only overcomes the problem of over rotation, but also simplifies the set-up by eliminating the need of polarization optics after the EO sampling crystal and the lock-in amplifier.

3.2 Theoretical background

The SD-LCI technique is based on a Michelson interferometer [74], where a broadband, low coherence source is used to illuminate a reference surface and a sample as shown in Figure 13.

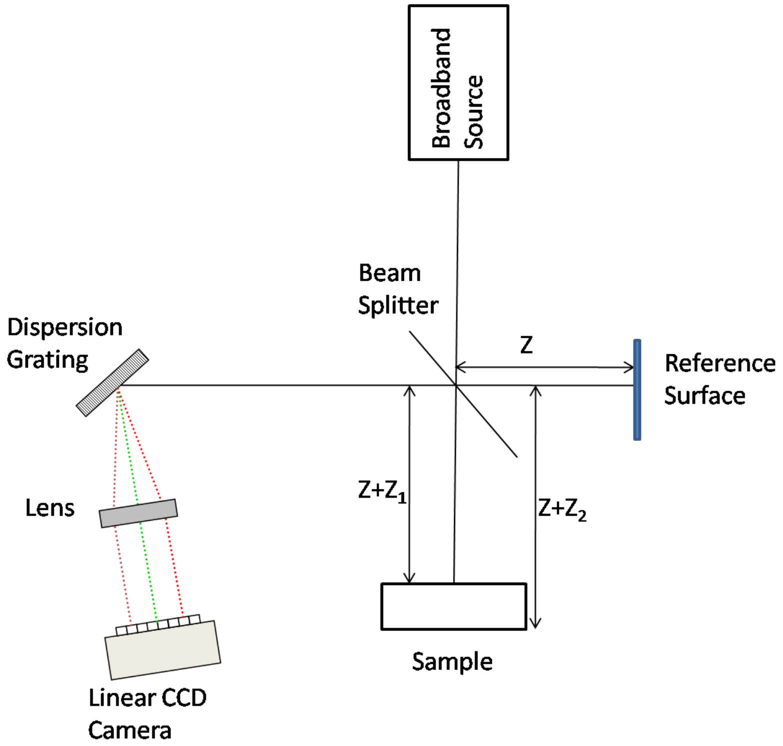

Figure 13. Schematic of spectral domain interferometry. The broadband light source is split in two parts. One part of the beam goes to sample surface and the other goes to the reference surface. After reflection from sample and reference surface, the two beams are sent to the grating via beam splitter. The diffracted spectral components of the beam are focused by lens and the interference pattern between the various spectral components of the two beams is observed at the CCD camera.

Consider that the sample is composed of two reflecting layers, one at an optical path difference of Z_1 and another at an optical path difference of Z_2 from the reference surface. The reflected light from the two illuminated objects is combined onto a dispersion grating that angularly separates the different wavelength components, which form an interference pattern onto a linear CCD camera using a lens. At the image plane, the phase difference between the signal reflected from the reference surface and the first layer of the sample is given by [75, 76]:

$$\phi_1(k) = \phi_0 + \frac{4\pi}{\lambda} Z_1 \tag{3.1}$$

where λ is the wavelength, $\emptyset_0$ is the phase change introduced by reflection at the first layer and Z_1 is the optical path difference between the reference surface and the first layer. Eq. (3.1) can be rewritten in terms of the wave-number, $k = 2\pi/\lambda$, such that

$$\phi_1(k) = \phi_0 + 2kZ_1 \tag{3.2}$$

which is a linear relationship between the phase and the wave-number. As the frequency along the k-axis is given by the rate of change of the phase with respect to the wave-number, Eq. (3.2) leads to

$$f_{k1} = \frac{1}{2\pi} \frac{\partial \phi_1(k)}{\partial k} = \frac{Z_1}{\pi} \tag{3.3}$$

Similarly for the second reflecting layer in the sample, the frequency of the phase is given by

$$f_{k2} = \frac{1}{2\pi}\frac{\partial\phi_2(k)}{\partial k} = \frac{Z_2}{\pi} \qquad (3.4)$$

One should note that analysis in the k-space is preferred to λ-space since f_k is independent of k, whereas the equivalent frequency derived from Eq. (3.1) in λ-space, would vary with λ. Thus, sampling the interferogram intensity data uniformly along the k–axis would cause a broadening in the frequency spectrum, which reduces axial depth resolution of the system [75, 76].

The intensity distribution along k-axis on the linear CCD camera as a result of the interference between the signal reflected from the reference surface and the signal reflected from the two layers of the sample can be expressed as

$$I_1(k) = I_0(k) + 2\sqrt{I_r(k)I_1(k)}\cos\left(\phi_1(k)\right) + 2\sqrt{I_r(k)I_2(k)}\cos\left(\phi_2(k)\right) \qquad (3.5)$$

where $I_0(k)$ is a dc term, $I_r(k)$, $I_1(k)$ and $I_2(k)$ are the intensity of the signals coming from the reference surface, the first layer, and the second layer, respectively, and $\phi_1(k)$ and $\phi_2(k)$ are the phase difference between the signal from the reference surface and the first layer, and the reference surface and the second layer, respectively. Because of the presence of cosine term and the fact that the phase difference is dependent on k, a modulation in the spectrum intensity along the k-axis is introduced. In Eq. (3.5) the modulation is the result of two signals with frequencies given by Eq. (3.3) and (3.4), which are directly proportional to Z_1 and Z_2, respectively. One should note that if there were N_l layers in the sample, the signal from each layer would interfere with the reference signal and produce a modulation in the spectrum intensity along the k-axis whose frequencies would be proportional to the optical path difference between the reference surface and all N_l corresponding reflecting layers. The Fourier transform of the intensity pattern at the camera, after proper calibration from pixel to *k*-space, directly leads to the frequencies of the modulation, thus the position of the reflecting layers within the sample with respect to the reference surface. Such frequency spectrum obtained after the Fourier transform of the spectrum intensity is commonly called axial scan (A-Scan), or depth scan.

3.2.1 Depth range of SDI

One of the drawbacks of using electro-optic sampling for THz measurement has been the difficulty to measure THz signals that causes a phase difference of more than $\pi/2$ between the s- and p-polarization states in EO crystal. This corresponds to a maximum measurable OPD that is equal to $\lambda/4$. However, in SDI, the maximum measureable OPD is limited by the depth range of the system, the details of which are discussed further.

In SDI, the available spectral bandwidth of the light source is spread over the limited number of CCD pixels. If the total Δk_{tot} -bandwidth of the interfering signal acquired with N_p number of pixels of the CCD camera is Δk, then the interval along the distance axis or the distance per pixel (Δd) after Fourier transform is given by $\Delta d = \frac{1}{2}\frac{2\pi}{\Delta k}$. The 1/2 factor in this expression accounts for the doubling of the OPD after reflection. The reader should note that in THz detection experiment, the change in OPD would be due to the change in the refractive index of the EO crystal (in a single pass). Therefore, the distance increment per pixel in this case is given by $\Delta d = \frac{2\pi}{\Delta k}$. Thus the maximum OPD that can be measured as a function of the N_p number of pixels of the CCD camera will be

$$d_{\max} = \frac{N_p}{2}\Delta d = \frac{N}{2}\frac{2\pi}{\Delta k} = \frac{N_p}{2}\frac{\lambda_0^{\;2}}{\Delta\lambda} \tag{3.6}$$

A factor of 2 appears in the denominator of the above equation, since the signal after Fourier transform (FT) is symmetric around zero OPD. Thus, the signals on the opposite side of zero give basically the same information. For a Gaussian profiled spectrum, the depth range can be written as:

$$d_{\max} = \frac{2\ln 2}{\pi}\frac{N_p}{2}\frac{\lambda_0^{\;2}}{\Delta\lambda} \tag{3.7}$$

A typical example of the SDI signal at different depths for a given depth range is shown in Figure 14:

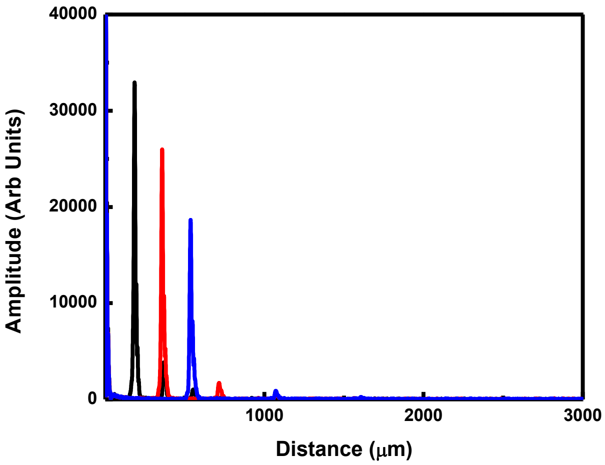

Figure 14. Change in the FFT signal with change in the optical path difference between sample and reference surface. Different colors represent the FFT signal (axial scans) at different optical path difference. The maximum optical path difference that can be measure between the two surfaces is called depth range of the system.

3.2.2 Signal-to-noise ratio of the system

The minimum OPD that can be measured with the SDI depends on the signal-to-noise (SNR) of the SDI system. The SNR of the SDI system is defined as

$$SNR_{SDI} = \frac{\tilde{I}}{SD} \tag{3.8}$$

where $\tilde{I}$ is the peak amplitude of the FFT peak in the Fourier transformed signal of the spectrometer signal, and SD is the standard deviation of the noise, away from the FFT peak. The phase stability or the standard deviation ($\left\langle \phi^2 \right\rangle$) of the measured phase is given by $\left\langle \phi^2 \right\rangle = \frac{1}{SNR_{SDI}}$. Thus the minimum OPD that can be measured with the SDI is given by [75]

$$\Delta z_{minimum} = \frac{\lambda_0}{4\pi} \left\langle \phi^2 \right\rangle \tag{3.9}$$

One can see from the above equation that the minimum measurable OPD depends on the SD of the phase measured, which in turn depends on the SNR of the SDI. Thus, in order to optimize the performance of the system in terms of OPD measurements, one should optimize the system in order to achieve the best SNR.

In SDI, if the two interfering signals pass through different optical elements, then a wavelength-dependent dispersion mismatch between the two interfering signals will induce broadening in the point spread function of the FT signal. This reduces the SNR of the system and thus increases the noise in the OPD measurements.

The dispersion in a signal is caused by the dependence of the propagation constant $\beta(\omega)$ on the frequencies it contains. In order to estimate the material dispersion, the propagation constant can be expanded as a Taylor series around the central frequency:

$$\beta(\omega)=\beta(\omega_m)+(\omega-\omega_m)\left|\frac{d\beta}{d\omega}\right|_{\omega_{\mathrm{m}}}+\frac{1}{2}(\omega-\omega_m)^2\left|\frac{d^2\beta}{d\omega^2}\right|_{\omega_m}+\frac{1}{6}(\omega-\omega_0)^3\left|\frac{d^3\beta}{d\omega^3}\right|_{\omega_m}+\ldots. \tag{3.10}$$

The first term in the equation is the propagation constant at central wavelength, and the second term is the inverse of the group velocity. The 3rd term, referred to as the group velocity dispersion or the 2nd order dispersion, causes pulse broadening in a broadband pulse. The 4th term, referred to as the third order dispersion, produces an asymmetric distortion into the pulse that is reflected in the point-spread function (PSF) of the FT signal.

In order to match the dispersion between the two interfering signals, the optical elements through which the two signals pass must be the same. Nevertheless, the dispersion mismatch can also be corrected numerically. In order to do so, techniques such as those described by Wojtkowski *et al.* [77] can be adopted. Briefly, for numerical dispersion compensation, first the data from the camera is transformed from the wavelength space to the frequency space. Then the phase of this transformed signal is calculated, to which a phase correction term given by the next equation is subsequently added.

$$\overline{\Phi} = -a_2(\omega - \omega_m)^2 - a_3(\omega - \omega_m)^3 \tag{3.11}$$

Following this step, the coefficients a_2 and a_3 can be adjusted to compensate for the 2nd order and 3rd order dispersion mismatch.

3.3 Experimental design

The experimental set-up for measuring the THz pulse shape using the spectral domain interferometric technique is shown in Figure 15.

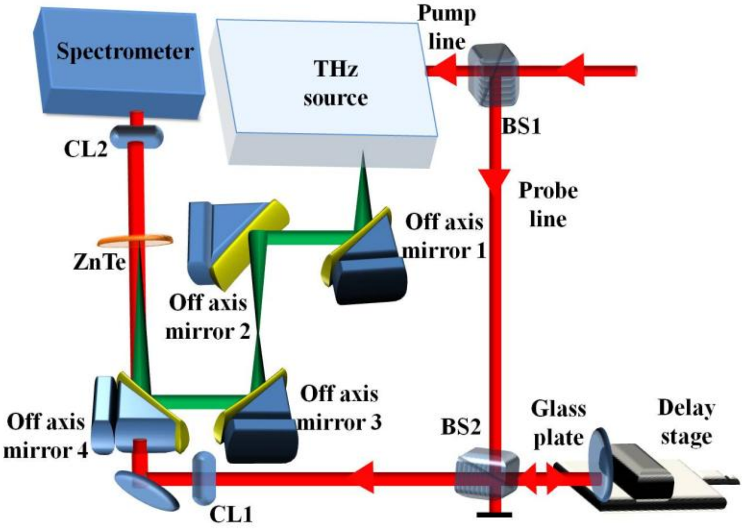

Figure 15. Experimental set-up. The input laser beam is split between the pump and the probe beams using a beam splitter BS1. The pump beam is used to generate THz radiation. The probe beam is further split by a beam splitter BS2. One part of the split beam is sent to the glass plate. The two surfaces of the glass plate reflect 4% each of the total incident signal. At the ZnTe detection crystal, the THz pulse is matched in time with the back-reflected pulse from the glass plate. After the ZnTe crystal, due to the THz electric field (Pockels effect) phase difference will be introduced between the front and back-reflected signals. This phase difference is measured using spectrometer, which is directly proportional to the THz electric field.

The beam splitter (BS1) divides the laser beam into a probe beam and a pump beam. The pump beam is used to generate the THz signal using the tilted-pulse-front technique in a $LiNbO_3$ crystal. This THz source generates 0.3 μJ THz pulses, with bandwidth extending from 0.1 THz to 3 THz. The beam splitter (BS2) divides the probe beam into two equal parts. The reflected part of the beam is sent to a 0.3 mm-thick glass plate. The two surfaces of the glass plate reflect about 4% of the incident beam. Half of the probe beam that is reflected from the glass plate is transmitted through the beam splitter BS2. The reflected signal from the glass plate consists of two pulses, one that is reflected from the front surface (front pulse), and the second from the back surface of the glass plate (back pulse). The front pulse and the back pulse are separated by 3 ps (due to the refractive index $n_r = 1.5$ for the glass plate). Using a cylindrical lens CL1, these two pulses propagate through a hole in the off-axis mirror, and their line-like spatial profile is focused onto the 0.5 mm thick ZnTe detector crystal at the same position in which the THz beam is focused. A cylindrical lens (CL2) is used to collimate the probe beam, which is then sent to a spectrometer. The custom made spectrometer consists of a grating with 600 groves/mm, a cylindrical lens with a focal length f = 100 mm and a 2D CCD camera with 760×1024 pixels. Using the spectrometer, the interference fringes are observed due to the interference between the front and back pulses. In SDI, the different spectral components of the beam are separated after the diffraction grating, and thus the various spectral components of the probe pulse are not mode locked any more. This is why one can measure the interference pattern over the depth range of the SDI technique (determined by the spectrometer used).

To measure the complete THz pulse, an optical delay line is used to vary the delay between the THz pulse and the optical pulse. The THz pulse is temporally matched with the optical back probe pulse. The delay between the front pulse and the back pulse is large enough (3 ps) to allow the front pulse to pass through the ZnTe crystal without “seeing” the THz electric field. The presence of the THz electric field changes the refractive index of the ZnTe crystal via the Pockels effect. The back pulse experiences this change in the refractive index, while the front pulse does not, thus introducing a phase difference between the two optical probe pulses. This phase change between the two optical probe pulses is proportional to the THz electric field. Therefore, we can reconstruct the shape of the THz electric field by changing the delay between the THz and the probe pulse. In our SDI method, we measure the change in the phase introduced by the change in the refractive index of the ZnTe crystal, from which we can measure the THz electric field up to the depth range of the SDI technique.

3.3.1 Numerical processing of the data

The data from the camera was numerically treated, involving a number of intermediate steps to reconstruct the THz signal. The steps that were required in this process are listed below.

1. The data from the camera was rescaled to the k-space from the wavelength space.
2. This data was then Fourier transformed to obtain the frequency corresponding to the OPD between the two signals reflected from the glass plate.
3. The phase between the two pulses reflected from the glass plate was measured using the following relation

$$\phi = \arctan\left[\frac{\mathrm{Im}(\tilde{I})}{\mathrm{Re}(\tilde{I})}\right]_l \tag{3.12}$$

Here, $\tilde{I}$ corresponds to the FT of the interference signal at the frequency peak corresponding to the OPD l.

4. This phase was tracked over time while changing the delay between the THz signal and the probing signal.
5. The phase waveform is directly proportional to the THz electric field.

3.4 Results and discussion

3.4.1 System characterization

Using the values of the parameters related to the designed system, *i.e.* $\lambda_0 = 790nm$, $\Delta\lambda = 40nm$ and N_p=1024 in the Equation (3.7), a theoretical depth range of 3.51 mm is obtained. Considering a change of 2π in phase for one wavelength change in OPD, with a depth range of 3.51 mm, an OPD equal to 8898π at $\lambda_0 = 790nm$ can be measured. This is approximately 18,000 times higher than the OPD measurable with the electro-optic sampling technique.

In order to support the depth range given by equation (3.7), the spectrometer must have a spectral range (for a Gaussian light source) of $\Delta\Lambda = \frac{\pi}{2\ln 2}\Delta\lambda$. The experimental value of the depth range achieved with the designed system was found to be 3.44 mm, which gives a spectral range of 92.46 nm for the spectrometer. Thus the spectral width per pixel is approximately 0.09 nm. For a given grating, whose numbers of groves $\mathbb{N}$ are illuminated with a beam, the theoretical resolution in wavelength for the 1st order diffraction pattern is given by

$$\Delta\lambda_{grating} = \frac{\lambda}{\mathbb{N}} \tag{3.13}$$

Where ℕ is the total number of grooves illuminated by the beam. In the spectrometer a grating with 600 grooves per mm and a beam of 6.2 mm diameter at FWHM was used. Thus, a total of 3720 (= 600 x 6.2) groves of the grating were used to disperse the beam with central wavelength 790 nm, giving a wavelength resolution of 0.21 nm. This is approximately twice the value of the spectral range per pixel at the CCD camera. Thus the designed spectrometer could support the wavelength resolution provided by the grating.

3.4.2 THz electric field measurement

For comparison purposes, the electric field of a THz pulse that was generated from a tilted-wave-front $LiNbO_3$ THz source, was measured simultaneously using EO sampling and SD interferometry, whose results are shown in Figure 16.

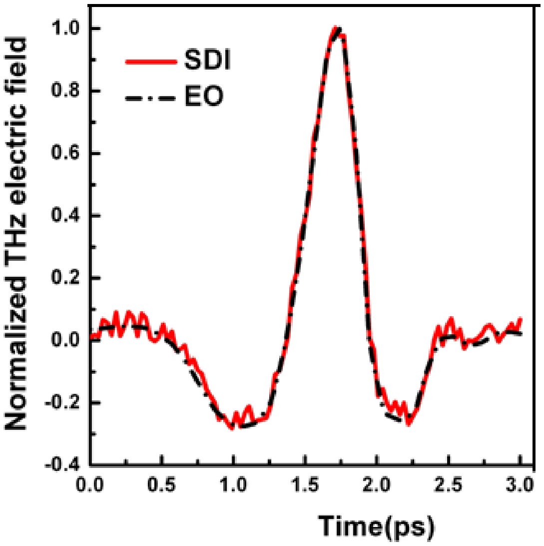

Figure 16. THz pulse measured with a spectral domain technique(blue) and via electro-optic sampling (black)

To compare the signal-to-noise (SNR) ratio of the two techniques, the power spectra of the two pulses are plotted together in Figure 17. From Figure 17, the S/N ratio of the EO sampling and the SDI are measured to be ~50000 and ~5000, respectively. The SNR of the SDI technique was found to around 10 times less than the EO sampling.

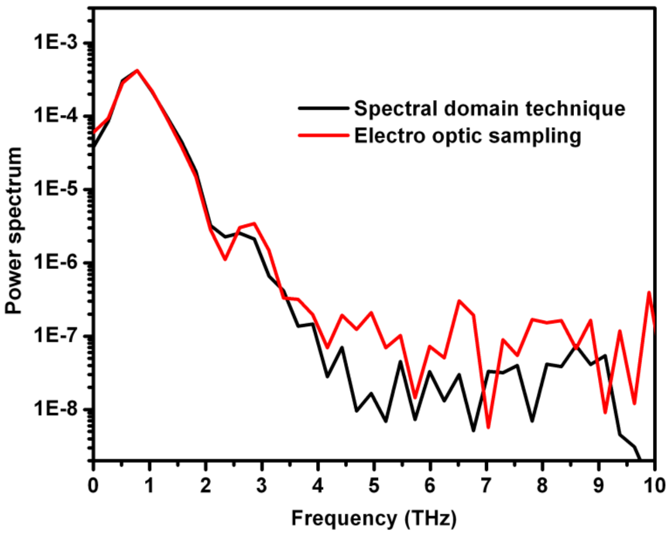

Figure 17. THz spectrum associated to the pulse in Figure 16

In the SDI detection technique, the optical probe beam was focused along a line at the detection crystal. This line was imaged back on the 2D CCD camera along the vertical direction, *i.e.* perpendicular to the diffraction plane of the grating in the spectrometer. This way the phase change or the OPD measured along the vertical direction of the CCD camera gives the spatial profile of the THz signal. Figure 18 shows the reconstructed spatial profile of the THz beam.

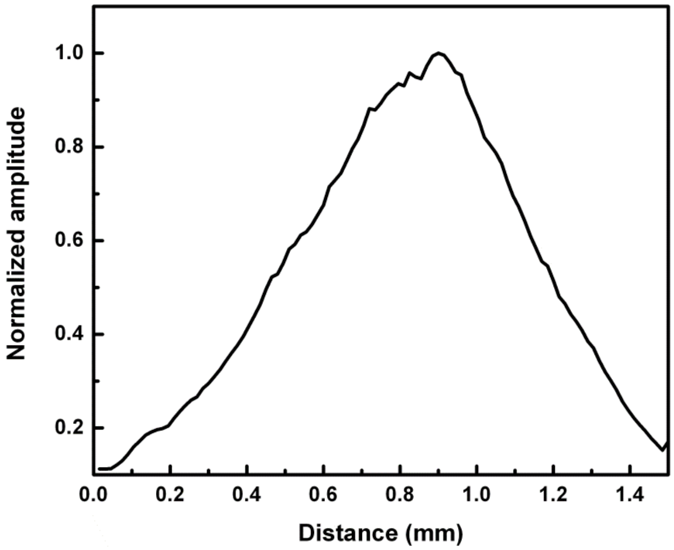

Figure 18. 2D Spatial profile of the THz beam measured in one temporal scan of the THz pulse.

Chapter 4

Nonlinear THz spectroscopy of semiconductors

4.1 Introduction

In the previous chapter, the generation and the detection of intense THz electric fields has been discussed. With the availability of high power THz sources, the next step is to study the different phenomena that may occur with the interaction of intense THz electric fields with different materials. THz spectroscopy is used to characterize the dynamical response of semiconductors. Therefore, at first, we investigated the THz electric field dependent nonlinear response of a gallium arsenide (GaAs) sample. The details of this work are discussed in this chapter.

4.2 Optical-pump/Terahertz-probe (OPTP) or time-resolved terahertz spectroscopy (TRTS)

Since it is the electric field of the THz pulse that is mapped in time, rather than the intensity, both amplitude and phase information are coherently detected and can be used to extract the real and imaginary parts of the index of refraction. In the mid-1980s [78], it was realized that since THz radiation is pulsed with durations on the order of 0.5 ps, it is possible to use them in a typical optical pump-THz probe configuration. Since then, terahertz pulse spectroscopy has become a widely used and powerful research tool to probe the transient conductivity dynamics in materials on a picosecond time scale [79]. The terminology used to describe this technique is known as time-resolved terahertz spectroscopy (TRTS) or optical-pump / THz-probe (OPTP) spectroscopy. A typical optical-pump / THz-probe set-up is shown in Figure 19.

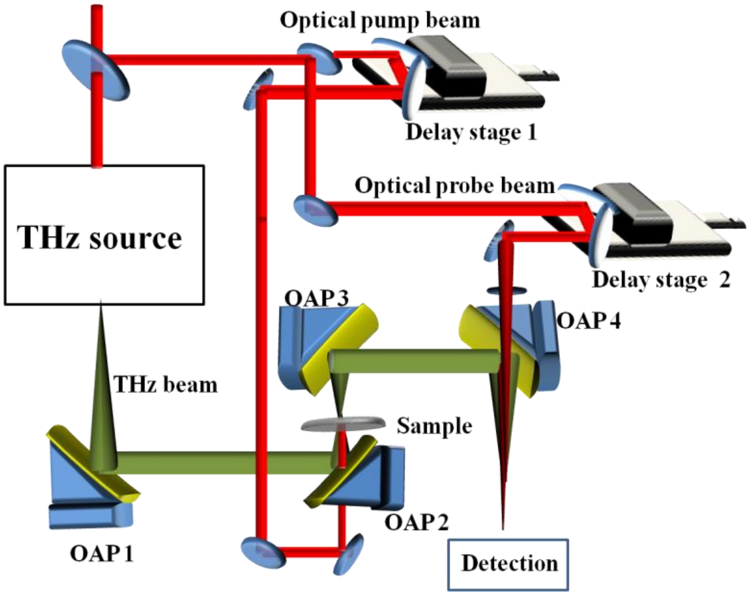

Figure 19. Schematic of the optical-pump-THz-probe technique. The sample is placed at the focus of the THz beam, between two off axis mirrors. An optical beam is sent through a hole in the off axis and illuminates the sample. The THz pulse probes the effect of optical excitation in the sample with picosecond time resolution.

In this technique, the attenuation of the THz electric field amplitude is monitored as it propagates through a photoconductive layer. One first adjusts the time delay such that the sampling beam and the peak of the THz pulse arrive at the detection ZnTe crystal at the same time, using delay stage 2. When the pump pulse overlaps the sample in time with the THz probe pulse, the induced photoconductivity in the sample reduces the transmission of the THz pulse due to free-carrier absorption. A schematic of the resulting scan is shown in Figure 20, with the normalized transmission (starting at 1 and decreasing), where T_0 is the THz transmission at negative pump-probe delay times.

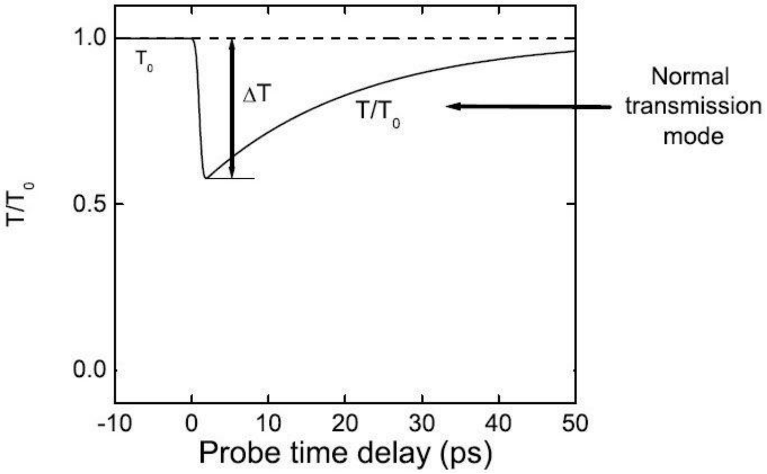

Figure 20. Typical optical-pump / THz-probe spectroscopy scan. When the optical pump pulse is matched in space and time with the THz pulse, the THz signal experience the sample as a conducting sheet with the number of carriers depending upon the optical pump energy. This results in drop in THz transmission, as can be seen in the graph.

4.3 Thin film equation for optical-pump / THz-probe spectroscopy

When a bulk semiconductor sample is pumped optically with appropriate frequency to photo-excite electrons in the conduction band of the semiconductor, a thin conducting film of carriers is formed at the surface due to photoexcitation. The derivation of an expression for the complex transmission function through a thin conducting film in between two media with real index of refraction is discussed in this section. In an OPTP experiment, the first medium would be air and the second would be the semi-insulating dielectric substrate. Figure 21 shows the electric field, magnetic fields and propagation vector for the reflected and transmitted electromagnetic waves that are incident on a thin conducting sheet. The continuity equations describing the electric and magnetic fields at the boundary are given by

$$\vec{n}\times\left(\vec{H}_1-\vec{H}_2\right)=\int_0^{\infty}\vec{J}dz=\vec{J}d \tag{4.1}$$

$$\vec{n}\times\left(\vec{E}_1-\vec{E}_2\right)=0 \tag{4.2}$$

Here $\vec{\mathrm{H}}$, and $\vec{\mathrm{E}}$ are the electric and magnetic fields, $\vec{n}$ is the surface vector normal to the surface, $\vec{J}$ is the current density, and d is the thickness of the sample.

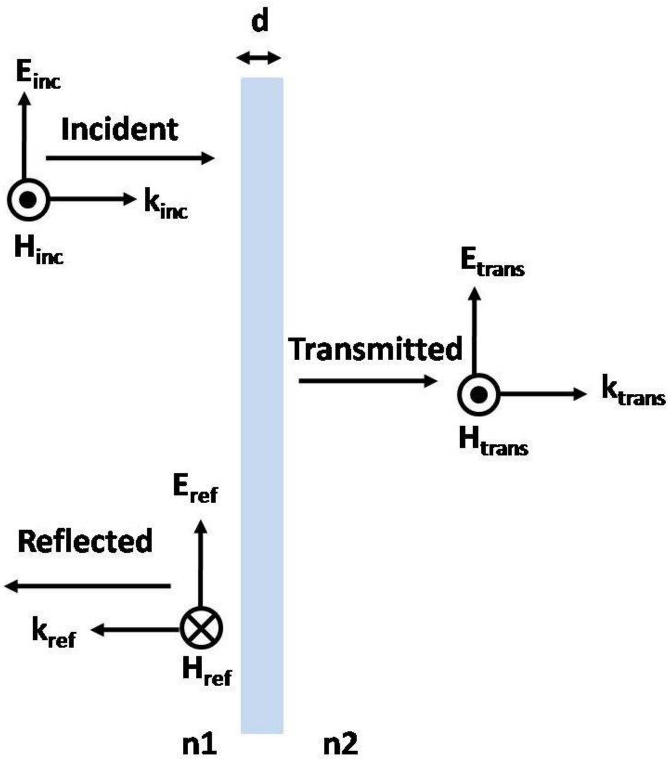

Figure 21. Electric field, magnetic field and propagation vector for the reflected and transmitted electromagnetic waves that are incident on a thin conducting sheet.

At normal incidence this simplifies to

$$H_{inc} - H_{ref} - H_{trans} = Jd \tag{4.3}$$

$$E_{inc} + E_{ref} - E_{trans} = 0 \tag{4.4}$$

Using the definition of admittance *Y* = *H/E* (i.e. the ratio of the magnetic field *H* to the electric field *E)*, and combining Eq. (4.3) and (4.4) the expression for the transmitted electric field can be written as

$$E_{trans}(t) = \frac{1}{Y_1 + Y_2}(2Y_1 E_{inc}(t) - Jd) \tag{4.5}$$

Here, $Y_1 = \dfrac{H_{inc} + H_{ref}}{E_{inc} + E_{ref}}$ and $Y_2 = \dfrac{H_{trans}}{E_{trans}}$. Solving for the transmission coefficient, $t = \dfrac{E_{trans}}{E_{inc}}$ and substituting $J = \tilde{\sigma} E_{trans}$, where $\tilde{\sigma}$ is the complex conductivity, one obtains

$$\tilde{t} = \frac{2Y_1}{Y_1 + Y_2 + \tilde{\sigma} d} \tag{4.6}$$

On substituting $Y_{\mathrm{i}} = \dfrac{n_i}{Z_0}$, where n_i is the index of refraction of the medium and Z_0 is the impedance of free space (377 ohms), the transmission through a thin conducting film, known as the Tinkham equation [80] can be written as

$$\tilde{t}_{film} = \frac{2}{n_r + 1 + Z_0 d \tilde{\sigma}(\omega)} \tag{4.7}$$

Here, the refractive index of air is 1 and n_r is the refractive index of the substrate. This equation is valid provided that $d \ll \lambda$, where λ is the wavelength in the film, so that any internal reflection within the photoexcited layer can be averaged over and neglected.

Using the transmission coefficient for the unexcited dielectric slab (substrate), $t_{subs} = 2/(n_r + 1)$, the transmission function for a photoexcited layer with respect to the background unexcited substrate is given by the following expression:

$$\tilde{T}(\omega) = \frac{t_{film}}{t_{subs}} = \frac{\tilde{E}_{pump}(\omega)}{\tilde{E}_{ref}(\omega)} = \frac{n_r + 1}{n_r + 1 + Z_0 d\tilde{\sigma}\left(\omega\right)} \qquad (4.8)$$

This equation is used to extract the frequency dependent complex conductivity. However, the analysis can be simplified enormously if it is assumed that the conductivity response is purely real, *i.e.* $\tilde{\sigma}(\omega) » \sigma_{dc}$ as it is for a Drude material in the Hagens-Rubens regime ($\omega\tau = 1$).

There are several examples of material systems that have been investigated by OPTP: superconductors[81], organic semiconductor[82], insulators [83], carbon nanotubes [84], nanocrystal silicon[85] and the semiconductor InGaAs / GaAs[86-88]. We applied the same methodology to investigate the effect of an intense THz probe on photoexcited GaAs.

4.4 Optical-pump / THz-probe measurement of a GaAs sample

GaAs is a cubic, direct bandgap semiconductor with an energy gap located at the Γ point in the Brillouin zone. The bandgap energy of GaAs is 1.424 eV. The band structure of GaAs is shown in Figure 22, showing important satellite valleys at the X and L points, located 1.71 eV and 1.9 eV above the valence band maximum at the Γ point. The knowledge of the band structure is important when investigating the electronic properties of semiconductors, since it determines the effective mass of a charge carrier, $m^* = h^2 \left[\frac{d^2E}{dk^2}\right]^{-1}$, and also since it indicates whether a carrier has sufficient energy to scatter into a typically lower-mobility satellite valley.

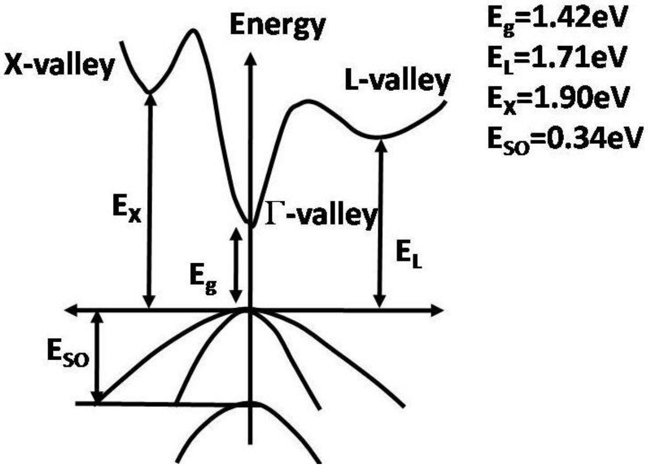

Figure 22. GaAs band structure [89]

4.4.1 THz source used for the experiment

For the GaAs experiments, high-energy THz pulses are generated by optical rectification in a large aperture (75 mm diameter) ZnTe single crystal wafer [26, 90]. The Ti:sapphire laser beam line of the Advanced Laser Light Source (ALLS) used in these experiments operates at a repetition rate of 100 Hz and provides 800 nm, ~ 40 fs laser pulses with energies as high as 48 mJ per pulse (at the ZnTe crystal position). The THz emitter consists of a 1-mm-thick (110) ZnTe single crystal wafer with a diameter of 75 mm. To minimize saturation and to avoid damage to the crystal surface, the 800nm beam is spatially expanded to about 36 cm^2 at $1/e^2$ (calculated based on the full-width at $1/e^2$ maximum beam size) at the surface of the ZnTe emitter. Off-axis parabolic mirrors are used after the THz generating crystal to redirect the THz wave to the detector, with 2 focus positions: (i) at the sample position for spectroscopy, and (ii) at the ZnTe detector crystal for EO sampling. A chopper positioned at the first focus allows modulation of the THz beam for lock-in detection. Two 4-inch diameter wire-grid polarizers (Microtech Instruments, model G30L) are used to control the intensity and the polarization of the THz beam.

To detect the THz pulse waveform, free-space electro-optic (EO) sampling in a second, 0.5mm thick, (110) ZnTe crystal [91, 92] is used. A lock-in amplifier connected to the output of a pair of photodiodes and referenced to the chopper is used to acquire the THz waveforms. The schematic of the experimental set-up is shown in Figure 23.

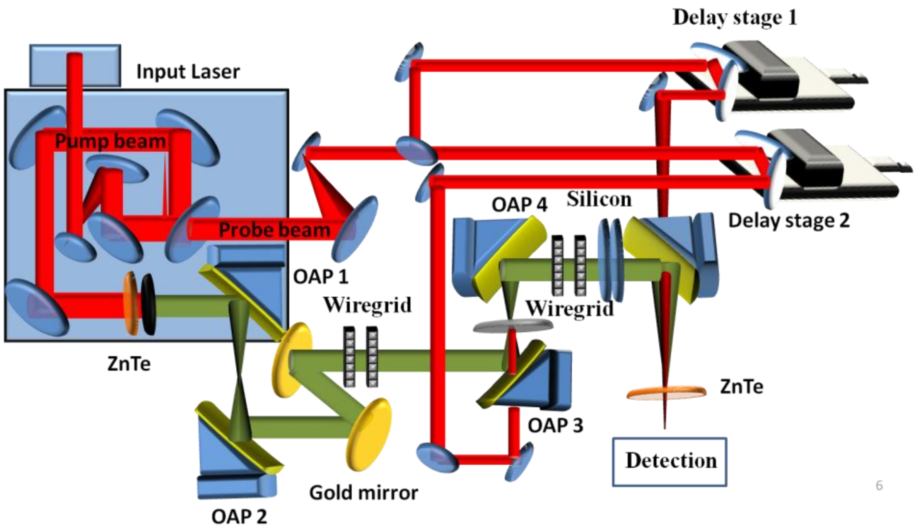

Figure 23. Schematic of the high-intensity THz pulse source at the Advanced Laser Light Source (ALLS) (adapted from Ref. [26]). The input laser is split between two parts, one part is used to generate THz radiation, and the other part is used to detect the THz signal transmitting through the sample using EO sampling.

The source provides picosecond THz pulses in the frequency range of 0.1 – 3 THz, with energy of 0.6 μJ. Figure 24 (a) shows an example of the temporal profile of the THz pulse produced by our source, and the inset shows the corresponding power spectrum. These pulses are focused by an off-axis parabolic mirror down to a spot size of 1.6 mm (full-width at $1/e^2$ maximum) at the first focal position (*i.e.* the sample position). A $BaSrTiO_3$ (BST) pyroelectric infrared camera (Electrophysics model PV320-L2V) is used to image the THz spot at the focus. This camera operates with an internal 10 Hz chopper and has a 320×240 pixel imaging array with a pixel spacing of 48.5 μm. Figure 24 (b) shows the THz image obtained using 0.6 μJ THz pulses. The THz beam profile is found to be well fitted by a Gaussian shape. For measuring the THz energy, a calibrated pyroelectric energy detector (Coherent Molectron J4–05) [26] is used.

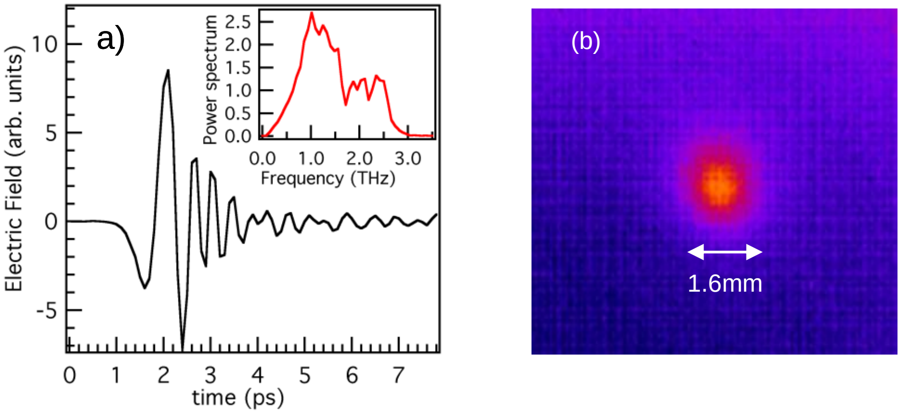

Figure 24. (a) Electric field profile of the terahertz beam emitted by the ZnTe optical rectification source. The inset shows the power spectrum of the THz pulse. (b) Pyroelectric detector array image of the THz spot-size at the focus with a $1/e^2$ diameter of 1.6 mm. (adapted from Ref. [12]).

4.4.2 Optical pump/THz probe experiment

An optical-pump / intense THz-probe (OPTP) technique is applied to explore the nonlinear electron dynamics of undoped GaAs [93]. The OPTP experiment is performed on a 0.5mm thick semi-insulating (SI)-GaAs wafer. The intense THz source described in the previous section is used for this experiment. The sample is placed at the focus of the THz beam, and an optical pump beam (800 nm wavelength, 40 fs pulse duration, 8 μJ/cm^2 fluence) is used to photoexcite the sample, as shown in Figure 23. At the sample position, the spot size of the THz probe beam and the optical pump beam are 1.6 mm and 12 mm, respectively. Before detection, in the arm where the THz beam is collimated, two wire grid polarizers are used to keep the THz electric field within the linear regime of the detection crystal. Another wire-grid polarizer as well as Si wafers is used to adjust the amplitude of the THz probe pulse at the sample position. All experiments were performed under a dry nitrogen purge at room temperature. First, the THz transmission at the peak of the THz pulse is measured, as a function of the pump-probe delay time. This is a common method for probing ultrafast carrier dynamics in semiconductors in linear OPTP experiments [94, 95]. The experiment was performed for high and low THz-probe field transmission in photoexcited GaAs, where high and low fields correspond to 173 kV/cm and 4 kV/cm, respectively. Figure 25 shows the THz transmission as a function of pump-probe delay time for high and low THz fields, respectively. The inset shows the long-term dynamics.

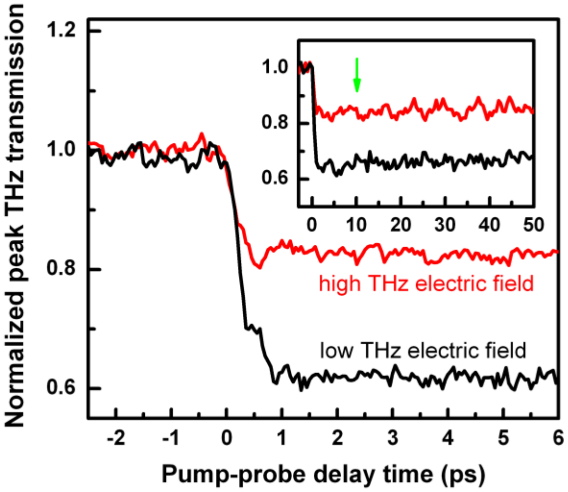

Figure 25. Normalized transmission of the peak electric field of a THz pulse at low and high THz fields as a function of delay time with respect to a 800 nm, 40 fs, optical pump pulse. The inset shows the corresponding long-term dynamics and the delay at which the waveforms shown in Figure 25 were taken (green arrow at 10 ps) [93].

4.4.3 Theoretical interpretation

The 800 nm pump pulse photoexcites electron-hole pairs in the normally insulating GaAs sample. Since holes in GaAs have a significantly lower mobility as compared to electrons, one can safely neglect the contribution of the holes to the overall conductivity of the sample. Due to optical pumping, photoexcited electrons are injected into the higher mobility central Γ valley in the conduction band by the pump beam. At low THz probe fields, the transmission of the THz pulse through the photoexcited GaAs sample is approximately 60% of the transmission through the unexcited sample. However, at high THz probe fields, the relative change in transmission is greatly reduced in comparison to the low THz probe field, suggesting that THz absorption bleaching is taking place. Here, absorption bleaching is defined as the reduction in the THz absorption in a photoexcited GaAs sample at high THz fields as compared to low THz fields. Absorption bleaching observed during the interaction of intense THz pulses with the photo-excited electrons in the conduction band of the GaAs sample can be attributed to THz-induced intervalley scattering between non-equivalent valleys. In particular, we focused on the electron dynamics in the *Γ* and the *L* valleys (being L the closest upper valley in GaAs) of the conduction band of the sample under investigation.

Absorption bleaching of intense THz pulses can be explained as follows. Free carriers in the *Γ* valley are accelerated by the THz electric field during each oscillation. When the carriers acquire enough kinetic energy to overcome the nearest intervalley separation, they may scatter into an upper valley (i.e. the *L* valley), as shown in Figure 26. Since the effective mass of electrons is higher in the *L* valley, the carrier mobility is lower, thus reducing the overall conductivity of the semiconductor-conducting layer. Since the transmission of the THz pulse increases with a decrease in the conductivity of the sample, the transmission is enhanced at high THz electric fields, when carriers are scattered to the upper satellite valleys. The electrons in this upper valley will then have a finite probability of scattering back to the *Γ* valley, where the effective mass is smaller. Therefore, the conductivity of the conducting layer will eventually increase back to its original value, which will result in a decrease in the THz transmission. From previous studies, it is well-known that optically induced intervalley scattering in ultrafast pump-probe and OPTP experiments (performed using higher pump photon energies, *e.g.,* 400 nm pump pulses) can excite carriers directly into the satellite valleys via optical phonon scattering [78, 95-99]. In addition, the observation of electric-field-induced intervalley scattering has been reported in OPTP experiments in DC-biased GaAs wafers [100]. However, in this work, we investigate the intervalley scattering induced by the THz probe pulse itself in an OPTP experiment.

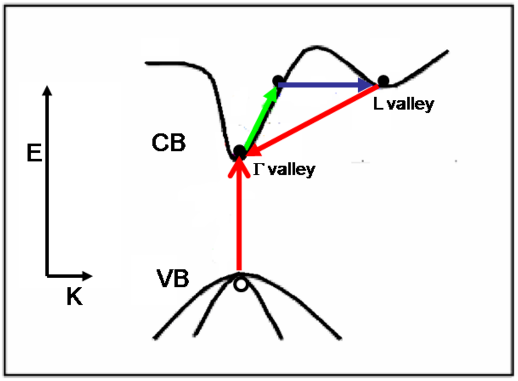

Figure 26. Mechanism of intense THz pulse induced intervalley scattering. The electrons in the conduction band are accelerated by the THz electric field (green arrow); after acquiring enough kinetic energy they may scatter into a satellite valley (L valley in this case, blue arrow), from which they have then a finite probability to scatter back to the bottom of the conduction band (red arrow).

4.4.3.1 Dynamic intervalley-electron-transfer model

A simple Drude-based model incorporating *Γ-L* intervalley scattering is used to describe the temporal dynamics of the observed nonlinear THz transmission. Here, charge carriers are considered free to respond to an electric field, with a collisional damping rate $1/\tau$. When a field is turned on, carriers equilibrate to a velocity distribution with a mean value, v. When the field is switched off, the carrier velocity distribution relaxes exponentially with time constant τ (scattering time), until the average carrier velocity, $v = 0$. The THz transmitted field of the samples, which can be idealized as a thin conducting sheet with thickness d on an insulating substrate with index n_r , can be expressed as:

$$E_{trans}(t) = \frac{1}{Y_0 + Y_s}\left(2Y_0 E_{inc}\left(t\right) - Jd\right) \tag{4.9}$$

Here, E_{trans} and E_{inc} are the transmitted and incident THz fields, respectively, $Y_0 = \left(377 ohms\right)^{-1}$ and $Y_s = n_r Y_0$ are the free-space and substrate admittances respectively, and J is the current density in the film, which is given by

$$J = n_\Gamma v_\Gamma e + n_L v_L e \tag{4.10}$$

Here, e is the electron charge, n_Γ and n_L are the electron densities, and v_Γ and v_L are the drift velocities of the Γ and L valley, respectively. The electron velocities driven by the transmitted THz field E_{trans} and the population of electrons in the Γ valley n_Γ can be described by the dynamic equations:

$$\frac{dv_i}{dt} = \frac{eE_{trans}}{m_i^*} - \frac{v_i}{\tau_i} \qquad i = \Gamma, L \tag{4.11}$$

$$\frac{dn_\Gamma}{dt} = -\frac{n_\Gamma}{\tau_{\Gamma L}} + \frac{n_L}{\tau_{L\Gamma}} \tag{4.12}$$

$$n = n_L + n_\Gamma \tag{4.13}$$

Here, τ_Γ, τ_L and m_Γ^* , m_L^* denote the intravalley scattering times and the effective masses in the two valleys, while $\tau_{L\Gamma}^{-1}$ and $\tau_{\Gamma L}^{-1}$ are the scattering rates from one valley to the other, and n is the total electron density. During the absorption bleaching process, the transmitted field, E_{trans}, accelerates the electrons in the conducting layer of the sample and induces the population transfer between the different valleys of the conduction band. This in turn affects the current density J in Eq. (4.10), and hence modifies the transmitted field. This feedback is responsible for the dynamical features associated with the effect under investigation. The change in electron populations in the Γ and L valleys is determined by the intervalley scattering rates. The $L-\Gamma$ transfer rate $\tau_{L\Gamma}^{-1}$ is kept constant [101], while the Γ–L scattering rate $\tau_{\Gamma L}^{-1}$ is a function of the average kinetic energy of the electrons in the Γ valley [102] :

$$\varepsilon_{\Gamma} = \frac{1}{2} m_{\Gamma}^{*} v_{\Gamma}^{2} + \frac{3}{2} k_{B} T_{L} \tag{4.14}$$

Here T_L is the temperature. This average kinetic energy is associated with the electrons in the Γ valley. The scattering rate $\tau_{\Gamma L}^{-1}$ is zero at low energies but starts to increase rapidly at a threshold value ε_{th} to a maximum value $\tau_{\Gamma L0}^{-1}$ at high energies.

$$\tau_{\Gamma L}^{-1}(\varepsilon_{\Gamma}) = \begin{cases} 0, & \varepsilon_{\Gamma} < \varepsilon_{th}\left(1-b\right) = \varepsilon_{1} \\ \text{smooth function for} & \varepsilon_{1} < \varepsilon_{\Gamma} < \varepsilon_{2} \\ \tau_{\Gamma L0}^{-1}, & \varepsilon_{\Gamma} \geq \varepsilon_{th}\left(1+b\right) = \varepsilon_{2} \end{cases} \tag{4.15}$$

Since intervalley scattering takes place via the emission or absorption of optical phonons, the energy-dependent function of the valley transfer rate, $\tau_{\Gamma L}^{-1}(\varepsilon_{\Gamma})$, is tentatively made “smooth”. The smooth function is inserted via a seventh-order polynomial section that is continuous up to the third derivative [102]. Here ε_{th} and b are the threshold energy and smooth width parameter, respectively. Nonparabolic effects are considered by assuming that the effective masses for Γ and L valley varies as

$$m_{\Gamma}^{*}\left(\varepsilon_{\Gamma}\right)=m_{\Gamma 0}^{*}\left(1+\alpha_{\Gamma}\varepsilon_{\Gamma}\right) \tag{4.16}$$

$$m_{L}^{*}\left(\varepsilon\right)=m_{L0}^{*}\left(1+\alpha_{L}\varepsilon_{L}\right) \tag{4.17}$$

Here, α_Γ and α_L are the nonparabolicity parameters for the Γ and L valley in the sample, $m_{\Gamma 0}^{*}$ and m_{L0}^{*} are the effective masses at the valley minima.

4.4.4 Simulated results

Figure 27 shows the transmitted THz waveforms measured at a pump-probe delay time of 10 ps. These waveforms were normalized to the peak of the THz waveform transmitted through the unexcited sample at negative delay times. Absorption bleaching can be clearly seen in the relative amplitude of the transmitted THz waveform at high THz fields, compared with that at low THz fields. In particular, there is almost no change in the electric-field amplitude or phase shift in the trailing portion of the THz waveform at high THz probe fields. We note that the observed absorption bleaching is inconsistent with an impact ionization mechanism, as impact ionization would induce an enhancement in THz pulse absorption [18, 103]. In Figure 27 (c), the transmitted THz electric field difference (ΔE) before and after the optical pump, under low and high THz probe fields, respectively, is presented. Since the optical penetration depth at 800nm is around 1 μm for GaAs, one can safely use Eq. (4.9) to describe the THz transmission through the sample. As it can be easily shown, ΔE is thus proportional to the current J, as well as to the average drift carrier velocity driven by the THz electric field. Figure 27 (c) shows that the high-field THz induced current/carrier average velocity, exhibits remarkable saturation effects, when compared with the low-field THz probe case. In particular, there is an abrupt drop of the absolute value of ΔE along the trailing edge of the THz pulse (after t=2.8 ps in Figure 27). This indicates that the carrier velocity becomes strongly nonlinear, when the optically excited GaAs is probed by a high-field THz pulse.

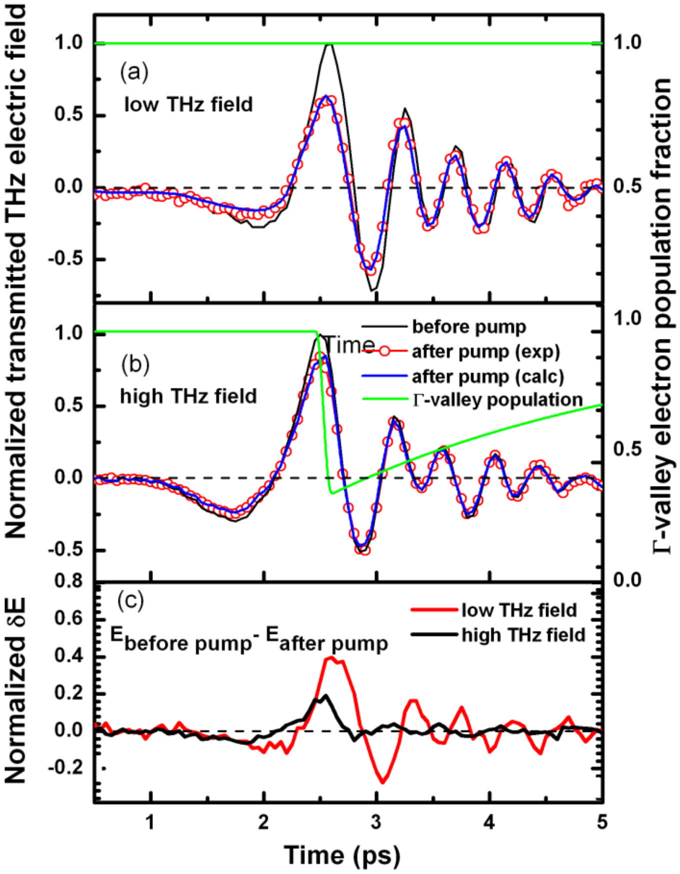

Figure 27. Transmitted THz waveforms measured 10 ps before and after photoexcitation. (a) Low and (b) high THz probe fields. The blue lines represent the best fit obtained using the dynamic intervalley-electron-transfer model. The green line shows the fraction of electrons in the *Γ* valley according to model calculations (adapted from Ref. [93]). (c) The experimental transmitted THz electric field difference between before and after the optical pump obtained from (a) and (b).

From the fitting of the low-field data (Figure 27(a)), the total carrier density and the intravalley relaxation time were obtained, resulting in a value n=1.7×10^{17} cm^{-3} and τ_{Γ} = 0.16 ps, respectively. This corresponds to a carrier mobility of 4200 cm^2/Vs, which is consistent with other OPTP experiments in GaAs [95]. This is also consistent with a total carrier density of about 1.9 × 10^{17} cm^{-3}, estimated from the measured pump fluence incident on the sample and assuming a pump beam reflectance of about 40%. At high THz fields, the same value for n is used as in the low-field case. The best fit to the observed THz transmission (Figure 27 (b)) gives τ_{Γ}= 0.051 ps and requires intervalley scattering with $\tau_{\Gamma L0}$ = 0.022 ps and $\tau_{L\Gamma}$= 3.0 ± 1.0 ps. The initial $\Gamma - L$ population transfer occurs over a timescale of 77 fs, which is comparable to the $\Gamma - L$ intervalley scattering times of about 80 fs reported elsewhere [104]. The transfer time back to the Γ valley of $\tau_{L\Gamma}$= (3.0 ± 1.0) ps also agrees well with the approximately 2 ps transfer times reported in other OPTP experiments [78, 99]. The threshold energy extracted from the fitting is ε_{th} = 0.16 eV, which is lower than the actual $\Gamma - L$ valley separation of 0.29 eV. This obvious discrepancy in threshold energy may be attributed to thermal smearing effects related to the hot electron distribution in the Γ valley [89, 98], which are not accounted for in the simple model. Table 3 below summarizes the best-fit parameters used in the dynamic intervalley-electron-transfer model.

Table 3: Model parameters for GaAs

Parameters	**Symbols**	**Simulation parameters**
Carrier concentration (cm^{-3})	n	1.7×10^{-17}[93]
Intra-valley scattering time (ps)	τ_{Γ}	Low field: 0.16 [93] High field: 0.051 [93]
Γ -L Intervalley scattering times (ps)	$\tau_{\Gamma L0}$	0.022 [93]
L- Γ Intervalley scattering times (ps)	$\tau_{L\Gamma}$	3 [93]
Threshold energy (eV)	ε_{th}	0.16 [93]

4.4.5 Velocity overshoot

It is well known that a velocity overshoot of electrons can take place under the application of a large DC electric field in GaAs, which is then followed by strong intervalley scattering over sub-picosecond timescales [89, 105, 106].

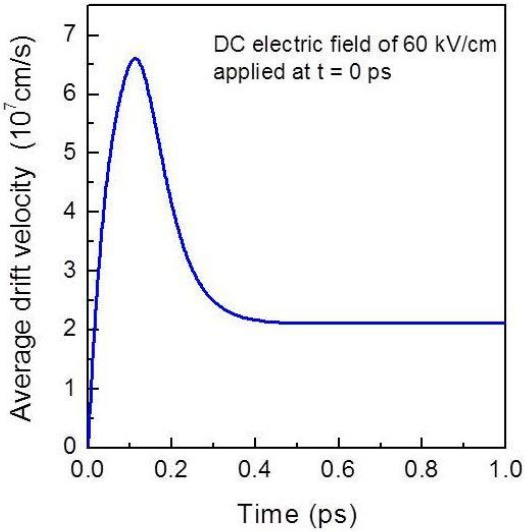

Figure 28 . Time evolution of the average electron drift velocity upon the application of a step-like electric field of 60 kV/cm, according to the dynamic intervalley-electron-transfer model (adapted from Ref. [93]).

For example, the maximum velocity acquired by an electron in GaAs after the application of a DC electric field of 40 kV/cm is about 7×10^7 cm/s [105, 106]. This velocity is reached in a time span of about 150 fs, after which intervalley scattering to the lower mobility *L* valley sets in, and the average carrier velocity is greatly reduced. Using the same parameters that were used in the dynamic intervalley-electron-transfer model to fit the THz data, a calculation of the average electron velocity $\langle v_\Gamma \rangle = (n_\Gamma / n_0) v_\Gamma$ upon the application of a step-like 60 kV/cm electric field, revealed a pronounced velocity overshoot in a time less than 200 fs, as shown in Figure 28. This is consistent with typical velocity overshoot phenomena in GaAs. As such, this provides some justification for the low threshold value for intervalley scattering of ε_{th} = 0.16 eV obtained from the simulation fits, despite the fact that the $\Gamma - L$ energy separation in GaAs is 0.29 eV. In fact, the energy associated to an electron with a velocity of 7×10^7 cm/s is only 0.1 eV, and yet this is where intervalley scattering is known to occur in GaAs. It is emphasized again that this represents the average electron velocity, and the thermal smearing due to carrier heating effects must be taken into account in a more detailed analysis. Nevertheless, the simple model used in this analysis seems to capture the essential physics of the observations on transient absorption bleaching when the photoexcited GaAs is illuminated with intense THz pulses. It is observed that recent THz-pump / THz-probe measurements have also shown transient absorption bleaching in GaAs due to intervalley scattering [103, 107].

4.4.6 Conductivity extraction

The frequency-dependent complex conductivity $\sigma(\omega)$ in an OPTP experiment can be calculated using Eq. (4.8). Here, $E_{trans\_P}(\omega)$ and $E_{trans\_R}(\omega)$ are the complex Fourier transforms of the time-domain THz waveforms transmitted through the excited and unexcited GaAs, respectively, n_r is the refractive index of medium Figure 29 shows the complex conductivities extracted from the transmitted THz waveforms using Eq.(4.8). At low THz probe fields, the observed conductivity spectrum is consistent with a Drude response [94, 95, 98], as shown in Figure 29 (a). However, the high-field conductivity spectrum shown in Figure 29 (b) differs significantly from the Drude behavior observed at low fields, and in fact cannot be fitted to any conductivity model. This is simply due to the fact that the conductivity of the photoexcited layer in the GaAs sample is a nonlinear function of the THz probe field at high fields. As such, the conductivity cannot be extracted by the simple Fourier analysis used in most OPTP experiments, since this would require the conductivity to be independent from the amplitude of the electric field. This emphasizes once more the need to look at the temporal evolution of the THz waveform rather than the frequency spectrum when probing materials with intense THz fields. Figure 29 (c) shows how the model fit becomes significantly less accurate if intervalley scattering is ignored.

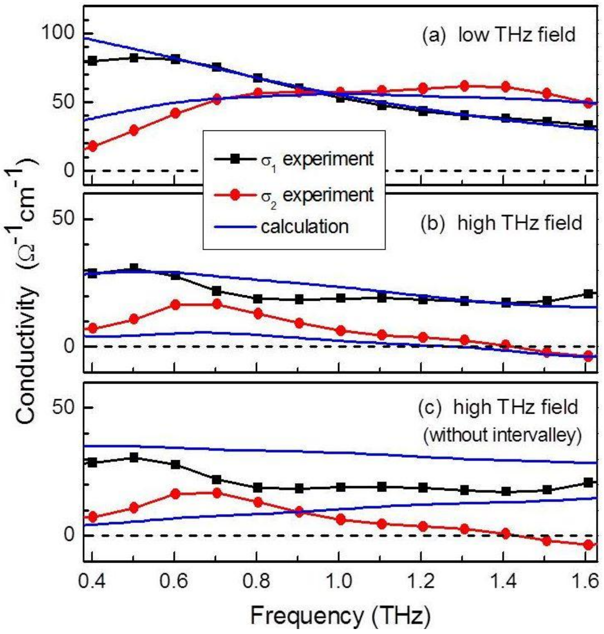

Figure 29. Real (σ_1) and imaginary (σ_2)part of the complex conductivity extracted at a pump-probe delay time of 10 ps measured at low (a) and high (b) THz probe fields. Blue lines in (a) and (b) are the corresponding fits using the dynamic intervalley-electron-transfer model. (c) The effect of neglecting intervalley scattering in the model (adapted from Ref. [93]).

4.5 Carrier density effects on nonlinear absorption of THz radiation in GaAs

In the first part of this chapter, THz-induced absorption bleaching in photoexcited GaAs sample is investigated, where the optical pump beam excites electrons in to the conduction band of the GaAs sample and we study the effect of the intense THz pulse on these photoexcited electrons. In order to obtain better insight, next we vary the carrier density in the conduction band of the GaAs sample by changing the optical pump fluence, and investigate its effect on THz induced absorption bleaching. In this section, the effect of carrier density on the nonlinear absorption of THz radiation in GaAs sample is discussed.

4.5.1 Experimental set-up

The same experimental set-up described in section 4.4.1 is used for this experiment as well. In order to change the optical pump power, and hence the carrier density within the GaAs sample, a set of half wave plates and polarizer is used. The carrier density is varied in the range of 1×10^{17} to 10.6×10^{17} cm^{-3}. The THz electric field is varied using wire-grid polarizers. In this study, we use two values of the THz electric field to investigate their effects: the high-field case (133 kV/cm) and the low-field case (9 kV/cm).

4.5.2 Definition of absorption bleaching

Before we start investigating the effect of carrier density on absorption bleaching, we need to quantify the effect by defining the “level of THz-induced absorption bleaching”, as follows:

$$
\begin{aligned}
&level\ of\ \ absorption\ bleaching = \Psi = \left[\left\{ \frac{T_{high}}{T_{low}} \right\} - 1 \right], \\
&T_i = \frac{\int \left| E^i_{samp}\left(t\right) \right|^2 dt}{\int \left| E^i_{ref}\left(t\right) \right|^2 dt} \quad ,\ i{=}high\ or\ low
\end{aligned}
\tag{4.18}
$$

Here, E^{high}_{samp} , E^{high}_{ref} , E^{low}_{samp} and E^{low}_{ref} are the transmitted THz electric field through the photoexcited (*samp*) and unexcited (*ref*) samples at high (133 kV/cm) and low (9 kV/cm) THz fields, respectively.

4.5.3 Experimental results and discussion

Figure 30 shows the THz induced nonlinearity (absorption bleaching) for carrier density ranging from 1.0×10^{17} to $10.6\ \times10^{17}$ cm^{-3}. It can be clearly seen from Figure 30 that ψ varies significantly with carrier density.

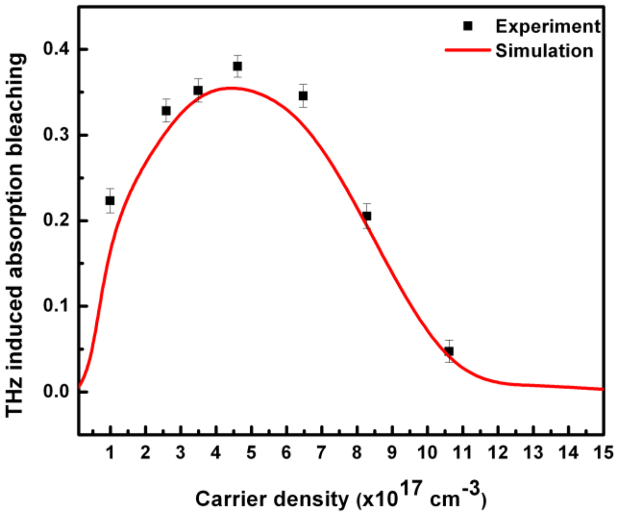

Figure 30. The carrier density dependence of the experimental (black squares with error bar) and simulated (red line) THz absorption bleaching for 800 nm photoexcited GaAs.

ψ in Figure 30 can be divided into two regions of carrier-density: (i) at relatively low carrier densities (<4.7×10^{17} cm^{-3}), ψ increases with increasing carrier density for 1×10^{17} cm^{-3} up to 4.7×10^{17} cm^{-3}. For the range of carrier densities we have investigated, absorption bleaching reaches a maximum at a carrier density of 4.7×10^{17} cm^{-3}; (ii) for carrier densities from 4.7×10^{17} cm^{-3} to 10.6×10^{17} cm^{-3} (the maximum carrier density under investigation), absorption bleaching decreases monotonically. For the maximum value of the carrier density studied (10.6×10^{17} cm^{-3}), ψ almost vanishes completely.

The difference between THz transmission at low and high THz fields has been explained in the previous section, and has been attributed to the intervalley scattering of electrons from the Γ valley to the L valley [20][93, 108]. To summarize, the mobility of electrons in the L valley is over 10 times less than in the central $\Gamma-$valley. Therefore, a high-field THz pulse that induces intervalley scattering of electrons into the L valley will effectively reduce the conductivity in the photoexcited GaAs, thus increasing the transmitted electric field when compared with the low-field case. This results in THz free carrier absorption bleaching for sufficiently high THz electric fields. The change in the bleaching from an increasing to decreasing dependence beyond 4.7×10^{17} cm^{-3} suggests the onset of a competing scattering process governed by the carrier density.

Previous linear THz spectroscopic studies have demonstrated that the density of the photo-injected electrons and holes strongly influences the mobility of the carriers in GaAs [99]. Analogous to impurity scattering, electron-hole (*e*-*h*) scattering limits the electron mobility [89, 99, 109]. As the effective mass of a hole is much larger than that of an electron, *e*-*h* scattering is insufficient to transfer energy from an electron to a hole. However, *e*-*h* scattering is effective for momentum relaxation. This reduces the Drude scattering time at low THz fields $\tau_\Gamma(low)$ and hence the electron mobility [99].

As the carrier density is increased, the *e*-*h* scattering reduces τ_Γ for the low field case. This in turn limits the maximum drift velocity achieved by electrons at higher carrier densities. In our simulation, we reduced the scattering time τ_Γ for low fields in Eq. (4.11) with increasing carrier density, in order to take this effect into account.

During the absorption bleaching process, the incident field accelerates the electrons in the conducting layer of the sample and induces a population transfer between the different valleys of the conduction band. This in turn affects the current density J in Eq. (3), and hence modifies the transmitted field E_{trans}. Now the current density depends on the drift velocity, and the drift velocity depends not only on the transmitted THz electric field but also on the electron and hole population. As the population increases, the momentum component parallel to the THz *E*-field vector is randomized due to *e*-*h* scattering, limiting the maximum achievable velocity and hence the kinetic energy of the electrons. As the carrier density increases further, the *e*-*h* scattering rate increases approximately linearly with a logarithmic correction [110, 111]. This has been taken into account in our model by decreasing the intravalley scattering rate in Eq. (4). The intervalley scattering rate depends on the energy of the electrons. If the kinetic energy of the electrons is reduced due to an increase in the *e-h* scattering, the intervalley scattering rate will also be reduced. This discussion suggests that absorption bleaching strongly depends on the charge carrier density.

To obtain a better insight into the physical process related to the observed THz nonlinearity, we extracted the carrier mobility from the intravalley scattering time, for the low THz field strengths (9 kV/cm) used in our simulations. Figure 31 shows the extracted mobility as a function of the carrier density. As previously discussed, it can be seen in Figure 31 that as we increase the carrier density, the overall mobility of the conduction band decreases. The mobility as a function of carrier density is empirically fitted using the Caughey-Thomas relation given by the following expression [98, 112].

$$\mu = \frac{\mu_{max} - \mu_{min}}{1 + \left(n / n\left(ref\right)\right)^{\gamma}} + \mu_{min} \tag{4.19}$$

Here, μ is the mobility and n is the carrier density. The values of μ_{max} and μ_{min} are floating parameters chosen via the best fit of a straight line to the plot of $log[(\mu_{max}-\mu)/(\mu-\mu_{min})]$ versus $log(n)$. The values of γ and $n(ref)$ are then obtained from the slope and unity intercept of the straight line. The fitting values obtained for μ_{max} and μ_{min} are 7900 cm^2/Vs and 1000 cm^2/Vs, in good agreement with previous work [98]. The value of γ and $n(ref)$ are evaluated to be 0.29 and 5.25×10^{16} cm^{-3}, respectively. The experimental data are shown to fit well with the Caughey-Thomas relation, corresponding to the solid black line in Figure 31. When the carrier density is increased from 1×10^{17} to 10.6×10^{17} cm^{-3}, the carrier mobility decreases from 4010 cm^2/Vs to 3055 cm^2/Vs [78, 95]. The red dashed line in Figure 31 shows the DC conductivity ($\sigma_{dc} = ne\mu$, where n is the carrier density, e is the electron charge and μ is the mobility) of the GaAs sample with respect to the carrier density.

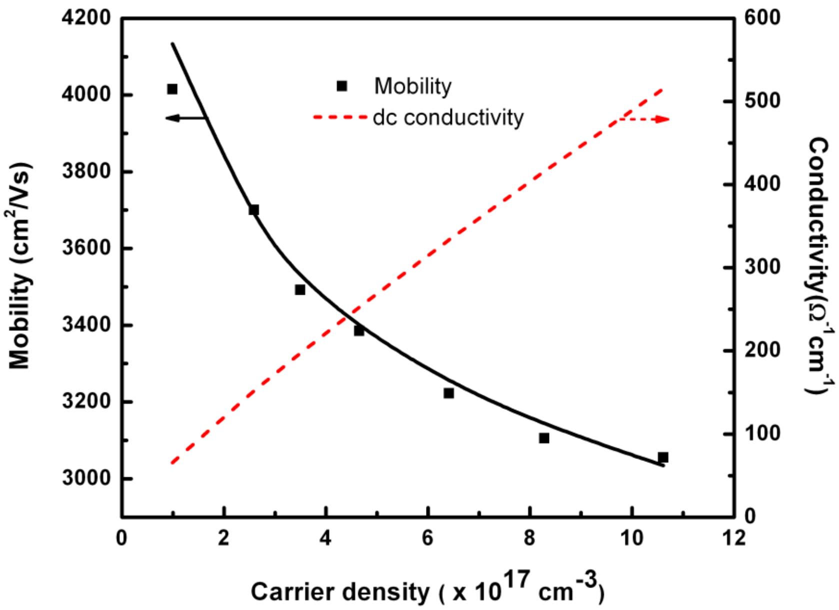

Figure 31. Electron mobility as a function of carrier density. The black squares represent the mobility of the carriers as a function of the carrier density, extracted from an intervalley scattering based Drude fit to the experimental data. The mobility follows the empirical Caughey-Thomas curve (solid black line). The DC conductivity as a function of carrier density is plotted in the red dashed line.

Here we have discussed the effect of carrier density on the THz pulses transmitted through photoexcited GaAs. The increase in absorption bleaching with the increase in carrier density (for $n < 4.7\times 10^{17}$cm^{-3}) follows from the initial increase in conductivity of the GaAs sample. For high THz fields, however, the transmission is affected less by an increase in carrier density, as compared to the low field case. The main reason for the relatively lower decrease in transmission for high fields is a reduction in electron mobility, due to two effects: nonparabolicity of the conduction band and intervalley scattering from the high mobility Γ valley to the low mobility *L* valley. The intervalley scattering rate depends on the electron energy, which is limited by *e*-*h* scattering via the reduction of the electron mobility. Even if the intervalley scattering rate is lower (thus promoting population of the Γ valley), the electron will still experience a reduction in mobility due to the nonparabolicity of the conduction band. Therefore, the THz transmission through the photoexcited GaAs layer is less attenuated for high fields as compared to low fields. This initially increases the THz induced absorption bleaching (when the carrier density rises from 1×10^{17} to 4.7×10^{17} cm^{-3}). However, a further increase in the carrier density beyond 4.7 ×

10^{17} cm^{-3} leads to a monotonically decreasing absorption bleaching as a function of density. This can be explained instead by the increased *e-h* scattering rate as a function of density, which in turn reduces the mobility significantly to the point where intervalley scattering becomes less likely and nonparabolicity effects (happening at the edge of the conduction band) can be ignored. Thus the high field transmission approaches the low field transmission and the absorption bleaching is reduced. Despite the simplicity of our model, we find that it explains the carrier density dependence of the nonlinear THz absorption rather well.

Chapter 5

Linear and nonlinear THz spectroscopy of graphene

Graphene is a novel material with tremendous applications in the THz regime. In particular, the high electron mobility of graphene suggests a great potential for broadband communications and high-speed electronics operating at THz switching rates [113, 114]. It has also been proposed that graphene can be used as frequency multipliers [115-118]. This makes it an important material to investigate at THz frequencies. In this chapter, we present preliminary results for linear and nonlinear THz spectroscopy of monolayer graphene.

5.1 Introduction

Graphene is single layer of carbon atoms and can be considered as a building block of several carbon allotropes. It has served many civilizations in the form of graphite, *i.e.* a stack of graphene sheets that is known to human beings since 1500 BC. Even though graphene has been around for such a long time, owing to its single atomic layer thickness, the separation of a single graphene sheet from a block of graphite was first demonstrated only recently in 2004 [119]. Ever since then, thousands of articles have been published in order to explain the unique properties of graphene.

In Graphene, the carbon atoms are arranged in a hexagonal structure, as shown in Figure 32.

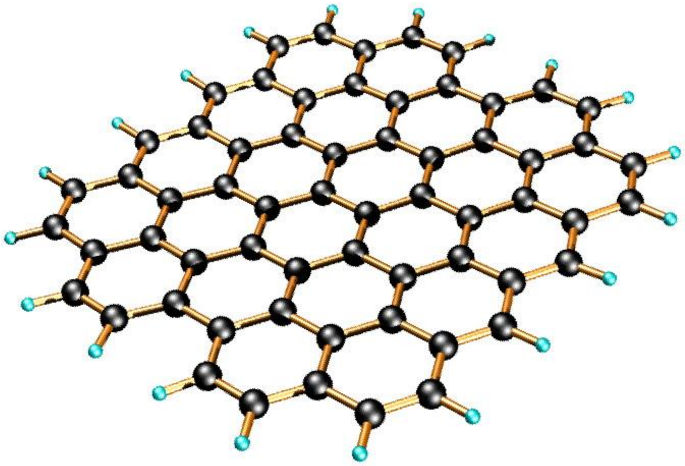

Figure 32. Honeycomb structure of graphene (adapted from Ref [121])

Due to the peculiar arrangement of the atoms in graphene, each carbon atom is tied to its three nearest neighbors. The carbon atom has 6 electrons, out of which 4 are in the valence shell. The three electrons out of the four valence electrons form the strong σ bonds that lie in the graphene plane at 120^0 angles. The fourth valence electron, whose orbital plane is orthogonal to the graphene plane, makes a weak π bond that is formed due to the overlap of its orbit with other orbits. It is this π bonded electron that gives rise to several interesting properties of graphene [120].

The unique structure of Graphene makes it different from conventional three-dimensional materials. The π bonded electrons, whose path crosses with each other, creates a cone-like structure called the Dirac cone, which is shown in Figure 33. The tip of this cone is called the Dirac point, and for each carbon atom arranged in a hexagonal symmetry, there are six such points [121].

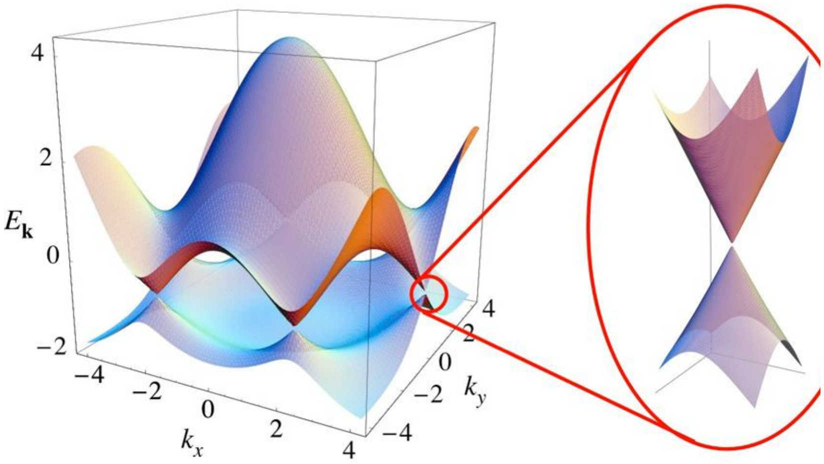

Figure 33. Energy dispersion relation of graphene (adapted from Ref [121])

As early as in 1947, it was suggested by P. R. Wallace that such a structure would give rise to a linear E-k relationship that leads to massless charge carriers at room temperature behaving like relativistic particles at the six Dirac points. With this unique structure, graphene behaves as a semiconductor with a zero band gap. This makes graphene a potential future candidate for the development of high-speed electron devices, including field-effect transistors, pin-diodes, Terahertz oscillators, and electronic and optical sensors [122-126].

Moreover, since graphene is the building block of carbon nanotubes (graphene sheet rolled along one axis) and fullerene (graphene in the shape of a ball), understanding the properties of graphene is essential in order to understand the properties of these materials. Such a study was not possible prior to 2004, due to the unavailability of freestanding graphene. Since then, several methods of graphene preparation as a monolayer, bilayer or multi-layer graphene have been proposed, some of which are discussed further.

5.2 Methods of fabrication

5.2.1 Mechanical exfoliation

The first ever method, which is by far also the simplest method for graphene preparation, is called mechanical exfoliation. In this method, which is also called the Scotch tape method, layers of graphene are peeled off from bulk graphite using adhesive tape [119, 127]. Since the graphene layers in graphite are loosely bound to each other via weak Van der Waals forces, peeling of the graphene layers is relatively easy using adhesive tape. This method has been successfully used by some groups to synthesize single-, double- and triple-layer flakes, up to 1 mm in size. The number of the layers extracted can then be determined using techniques such as Raman spectroscopy [128].

5.2.2 Chemical vapor deposition

Chemical vapor deposition is another method that has recently been used to grow thin graphite and graphene layers [129, 130]. In this technique, hydrocarbon molecules from hydrocarbon gas that is placed near a metallic surface are decomposed, allowing the carbons atoms to dissolve into the metal. The thin film of carbon atoms deposited on the metal foil can then be transferred to a polymer or semiconducting substrate via chemical etching [130]. The monolayer of graphene produced in this way has shown high mobility (~4000 $cm^{-2}V^{-1}$ s^{-1}) with only a few defects, which makes this technology promising for graphene preparation.

5.2.3 Graphene from silicon carbide crystal

In this method of graphene preparation developed by Heer *et al.* [131-134], silicon atoms from a hexagonal silicon carbide (SiC) crystal are evaporated by heating it to the temperature of 1300 degree Celsius, which leaves behind a sheet of graphite. The properties of the graphene produced using this method highly depend on the surface of the SiC crystal on which graphene is grown. For graphene grown on the SiC (0001) face of the crystal, which is bound to the substrate through covalent bond, it has been shown that the interaction between graphene and the substrate shifts the Fermi energy above the Dirac point due to n-type doping. Although the graphene layers deposited on the SiC $(000\bar{1})$ face show Dirac cones in their low-energy band structure, these layers do not show graphene-like band structures, due to the additional strain caused by a dilated C–C bond length in this layer [135]. On the other hand, graphene grown on a SiC (0001) face would be bound to the substrate through weak dispersion forces. Multilayer graphene grown using this method with rotational disorder, which minimizes the interaction between the layers, shows the properties of a monolayer graphene. The two-graphene samples (provided by Kyushu University and by NTT (Japan)) used in our experiment were fabricated using this method.

5.3 Graphene characterization

Once the graphene sample has been prepared, the next step is its characterization. This includes determining the number of graphene layers deposited and the properties of the sample. Some of the techniques that have been used for this purpose are discussed further.

5.3.1 Atomic force microscopy

Atomic force microscopy (AFM) is a technique that can measure the thickness of a sample grown on the substrate with picometer (10^{-12} m) accuracy. Therefore, AFM could be used to determine the relative height of the graphene layer with respect to the substrate. By knowing the thickness of one graphene layer, one can determine the number of layers of graphene present on the substrate. AFM was used by Obraztsova *et al.* [128] in order to perform a statistical analysis over many graphene samples, and the thickness of the graphene layer was predicted to be approximately 0.35 nm. Although the measured graphene thickness matches very well with the previously estimated values of the graphene layer thickness, the use of AFM is time consuming, while leading to low throughput. AFM measurements for three different graphene samples are shown in Figure 34.

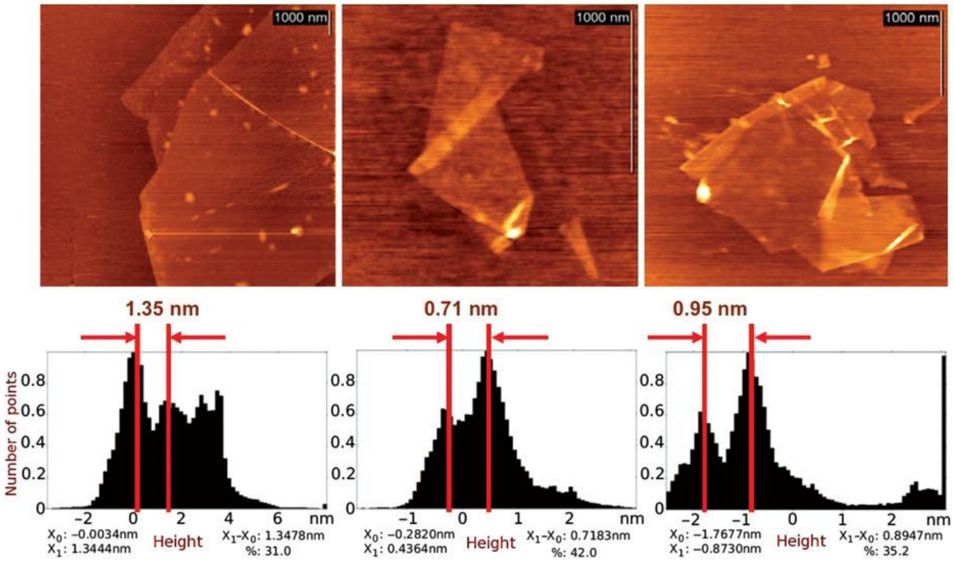

Figure 34. The atomic force microscopy (AFM) images of three different arbitrary graphene flakes and the distribution of the height values over their surface points [128].

5.3.2 Raman spectroscopy

Raman spectroscopy, which is related to the phonon modes in the sample being probed, has shown a much higher throughput as compared to AFM in determining the number of layers in a graphene flake. The most prominent Raman feature in graphene is called the G band, appearing at 1582 cm^{-1}, and the G’ band appearing at 2700 cm^{-1}, using a laser excitation of 2.41 eV, as can be seen in Figure 35.

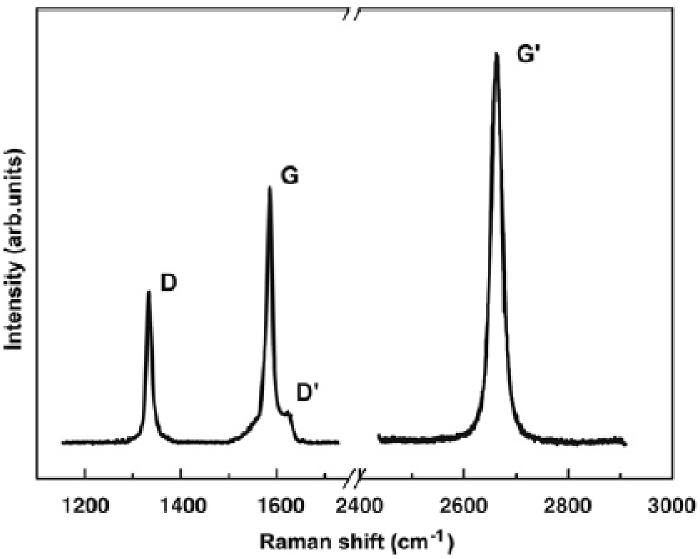

Figure 35 Raman spectrum of graphene edge, showing the main graphene features at 1582 cm^{-1} (G peak) and 2700 cm^{-1} (G' peak) [136]

5.3.3 THz spectroscopy

Using THz linear spectroscopy, we can extract the sheet conductivity of the graphene sample. This sheet conductivity can be a useful parameter to know the quality of the graphene sample under investigation. We have used THz time-domain spectroscopy technique to measure the sheet conductivity of the graphene sample, as described in next section.

5.4 Determining the sheet conductivity of a graphene sample using THz spectroscopy

Absorption of electromagnetic radiation by graphene is calculated to be frequency-independent for the spectral range from 0.5 to 1.2 eV, with a magnitude given by $\pi\alpha = 2.3\%$ [137]. Prediction of such frequency independent constant absorbance is equivalent to a frequency independent optical sheet conductivity of graphene, which is given by $\pi e^2/2\hbar = 6.1\times10^{-5}\Omega^{-1}$ [138]. This universal conductivity behavior is in accordance with the idealized model of interband transitions [137]. However, this universal behavior breaks down as the photon energy goes below 0.2 eV. For THz photons (with photon energy of 4 meV), graphene conductivity is dominated by intraband transitions, and should reflect the DC electrical conductivity of graphene. Therefore, sheet conductivity at THz frequencies can be a useful tool to determine the quality of the graphene sample.

The theoretical background for extracting the sheet conductivity of the sample is discussed in the following section, followed by the experimental determination of sheet conductivity in section 5.5.2.

5.5.1 Theoretical background

Our graphene samples can be divided into a multi-layer structure consisting of layers of air, graphene, SiC and another layer of air, being the four regions designated by index 1, 2, 3, and 4 respectively. The geometry for this sample is shown in

Figure **36**, with air (1, 4), graphene (2) and the SiC substrate (3) regions indicated. When the electromagnetic field propagates through this sample, there will be multiple reflection and transmission due to these interfaces as shown in Figure 36. If *t* is the field transmitting through the graphene sample, after the SiC-air interface (3-4), the first transmission through the sample will be given by $t*t_{34}$, here t_{34} is the part of the transmitted field after the reflection through the 3-4 interface. Similarly the second transmission will be given by $t*r_{34}*t_{34}$. We analyzed this multilayer structure using the Fresnel coefficient and the thin film Drude model.

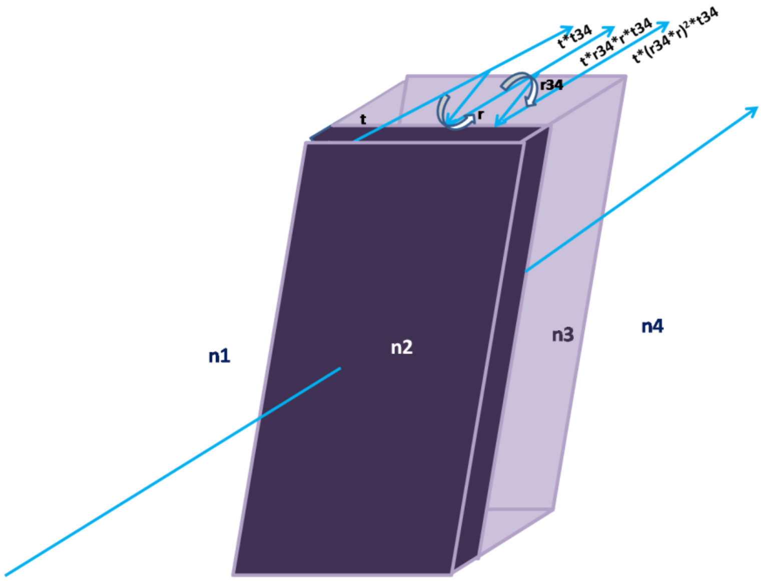

Figure 36. Transmission of the electromagnetic signal through air (n1), graphene (n2) and substrate (n3) interface, for the electromagnetic pulse propagating normal to the surface.

5.5.1.1 Fresnel coefficients

For the reflection and transmission of radiation across an interface (i and j), the boundary condition for the tangential components of the electric ($\vec{E}$) and magnetic field ($\vec{H}$), and the normal components of the electric displacement ($\vec{D}$) and magnetic flux ($\vec{B}$) should be continuous across the interface. When the propagation direction of radiation is at normal incidence to the medium, the amplitudes of the incident (E_{inc}, H_{inc}), transmitted (E_{trans},H_{trans}) and reflected (E_{ref}, H_{ref}) fields can be given by Eq. (4.3) and Eq. (4.4) respectively. Using the relations $H = B / \mu = B / \mu_0$ (non-magnetic material), $\left|\vec{E}\right| = v\left|\vec{B}\right|$ and $v = c / n$, where n is the index of refraction, we arrive at the expression:

$$E_{trans} n_2 = E_{inc} n_1 - E_{ref} n_1 \tag{5.1}$$

$$E_{trans} = E_{inc} + E_{ref} \tag{5.2}$$

Combining Eq. (5.1) and (5.2) gives the amplitude reflection (r_{12}) and transmission coefficient (t_{12}), between the 1 and 2 interface, at normal incidence,

$$r_{12} = \frac{n_1 - n_2}{n_1 + n_2} \tag{5.3}$$

$$t_{12} = \frac{2n_1}{n_1 + n_2} \tag{5.4}$$

These equations describe completely the electromagnetic radiation as it crosses an interface of a bulk material.

5.5.1.2 Graphene sheet conductivity

The graphene layer is treated as a zero thickness thin conducting film, whereas the SiC substrate is considered as an optically thick medium. Using a Drude thin film model (see Chapter 4), Eq. (4.7), the transmission through the first interface $(\text{air} \rightarrow \text{graphene} \rightarrow \text{SiC})$ is given by [139]

$$t(\sigma_s) = \frac{2}{n_{SiC} + 1 + Z_0 \sigma_s} \tag{5.5}$$

The internal reflection from the graphene interface is given by

$$r(\sigma_s) = \frac{n_{SiC} - 1 - Z_0 \sigma_s}{n_{SiC} + 1 + Z_0 \sigma_s} \tag{5.6}$$

Here, Z_0 (376.7 Ω) is the vacuum impedance, σ_s is the conductivity and n_{SiC} is the refractive index of the substrate. The relative field transmission of the mth pulse is given by

$$t_{rel}^{(m)}(\sigma_s) = \frac{E_{G-SiC}^{(m)}}{E_{SiC}^{(m)}} = \frac{t(\sigma_s)}{t_{13}} \left(\frac{r(\sigma_s)}{r_{13}} \right)^{m-1} \tag{5.7}$$

Here, $E_{G\text{-}SiC}^{(m)}$ is the electric field of the mth pulse after transmission through the sample/substrate and $E_{SiC}^{(m)}$ is the electric field of the mth pulse after transmission through the SiC substrate, $t(\sigma_s)$ and $r(\sigma_s)$ are the transmission and reflection signal through graphene over SiC layer and t_{13} and r_{13} are the signal transmitted and reflected through just SiC susbtrate only. So here, $n_1 = n_{air}$ and $n_3 = n_{SiC}$. For the refractive index of SiC n_{SiC} =3.677 and for air n_{air} =1, the conductivity for the first pulse in time (no reflection) is given by

$$\sigma_s = \left(\frac{4.677}{t_{rel}^{(1)}} - 4.677 \right) \times \frac{1}{377} \tag{5.8}$$

5.5.2 Experimental extraction of sheet conductivity

For the experimental extraction of sheet conductivity of the graphene sample, a THz time-domain spectroscopy (TDS) system based on a photoconductive antenna is used. The experimental set-up of the THZ-TDS system is shown in Figure 37.

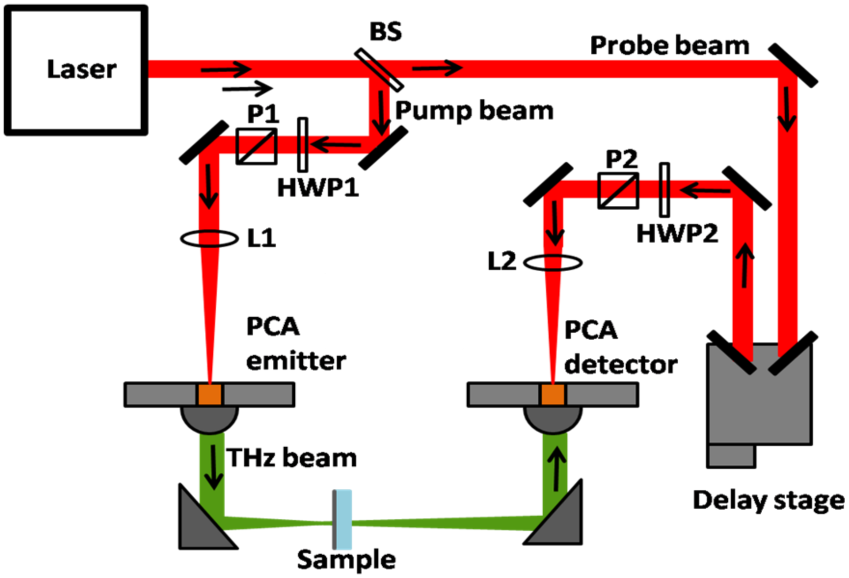

Figure 37. Experimental set-up for linear THz spectroscopy. The THz signal is generated and detected by using photoconductive antenna. The sample is placed at the focus of the THz beam. The transmitted signal through the sample is measured at the detector antenna.

The input laser beam is split into two parts (the pump and the probe beam) using the beam splitter BS. The probe beam passes through the delay stage in order to match the optical path length of the pump and the probe beam. Two sets of half wave plates and polarizers are used to control the pump and probe power that reaches the PCA emitter and detector. The optical pump and probe beam are focused on to the PCA emitter and detector using two lenses L1 and L2. For THz generation, a bias voltage is applied to the emitter. THz radiation is generated by the acceleration of the optically pumped electron in the conduction band of the PCA switch, driven by the bias voltage. The generated THz radiation is collimated using a silicon lens, and is focused using an off-axis mirror at the sample position. The THz signal is collimated again with a second off-axis mirror and focused at the detector antenna using a second silicon lens. The typical waveform of the generated THz and its corresponding spectrum is shown in Figure 38.

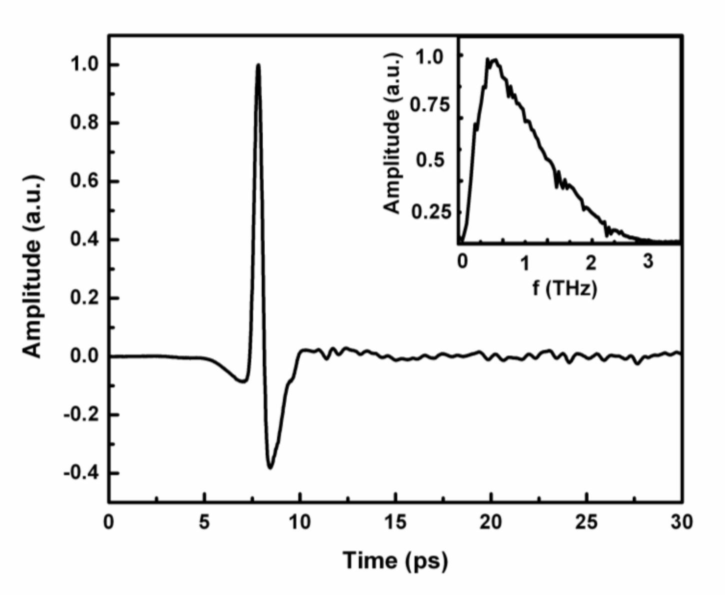

Figure 38. THz pulse shape and corresponding spectrum in inset.

The graphene sample fabricated on a SiC substrate is placed at the focus of the THz beam, and the THz detector measures the transmitted THz signal. Figure 39 shows the THz pulse transmitted through air only, and through the sample with a SiC substrate (graphene + SiC). As it can be seen from Figure 39, one can also see multiple reflections of the THz pulse from the sample/air interface, that can be used to extract the sheet conductivity information.

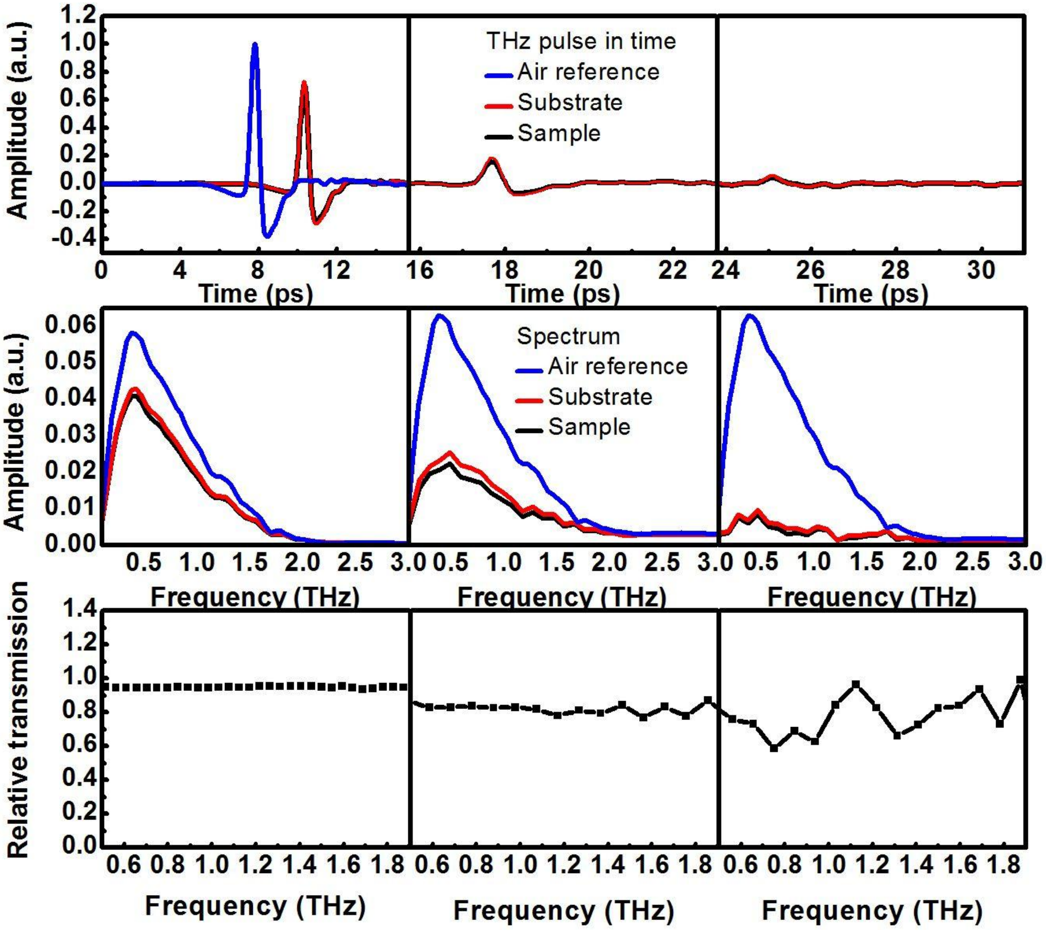

Figure 39. (a)THz pulse (b) corresponding spectrum (c) relative transmission (sample/ substrate) in air, through Substrate (SiC) and Sample (graphene on SiC)

Using Eq. (5.8), one could extract the sheet conductivity of the graphene sample, knowing the relative transmission ratio (t_{rel}) from the experimental data.

For the first THz pulse in time, the extracted sheet conductivities of the graphene sample fabricated by NTT and by Kyushu University are shown in Figure 40.

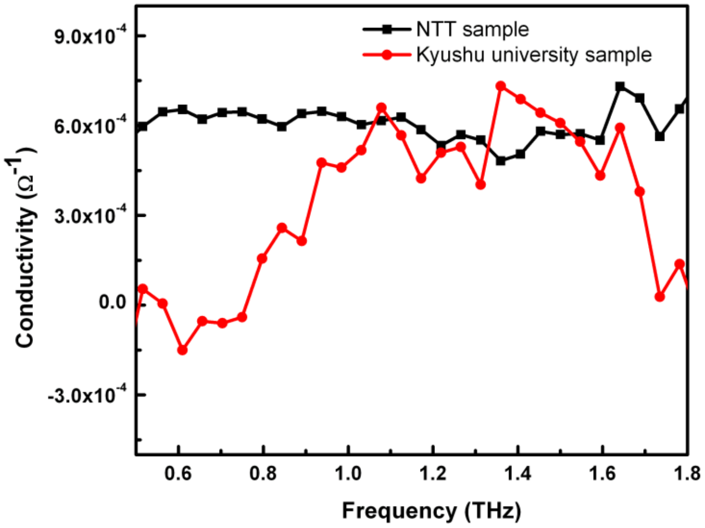

Figure 40. Experimentally extracted conductivity of the two graphene samples from NTT and Kyushu University

As can be seen from Figure 40, the sheet conductivity of the graphene sample fabricated by NTT is ~$0.6\times10^{-3}\Omega^{-1}$. For the NTT sample, the sheet conductivity of the sample is uniform for the frequency range of 0.5 – 2THz, whereas the sheet conductivity of the graphene sample fabricated by Kyushu University varies from 0 to $0.6\times10^{-3}\Omega^{-1}$. There are several other works that shows that the sheet conductivity of the graphene sample should be constant as a function of frequency raging from for 0.1-3THz [139]. The measured sheet conductivity is ~10 times greater than $\sigma_q = e^2/4\hbar$ = $6.1 \times 10^{-5}\Omega^{-1}$ (σ_q is the optical conductivity of graphene due to interband transitions [138]). The measured conductivity is higher than the universal conductivity, since the conductivity in THz range is dominated by the intraband transition and it corresponds to the dc conductivity of the graphene sample. These results show that THz spectroscopy can be a useful tool to evaluate the quality of the graphene sample.

5.6 Nonlinear response of graphene at THz frequencies

Various theoretical works show that graphene possess a strong nonlinearity at THz frequencies [115-118]. To qualitatively demonstrate the nonlinear behavior of graphene electrons, consider a classical 2D particle with charge *-e*. The energy spectrum is given by the following equation [140]

$$\varepsilon_p = vp = v\sqrt{p_x^2 + p_y^2} \tag{5.9}$$

Here, *v* is the velocity of the 2D electrons in the energy band (in graphene $v \approx 10^8$ cm/s [123, 124]) Here electrons are massless like photons with velocity $v \approx c$. The applied external electric field E_x is given by,

$$E_x(t) = E_0 \cos \Omega t \tag{5.10}$$

According to classical mechanics, the equation of motion can be written as

$$\frac{dp_x}{dt} = -eE_x(t) \tag{5.11}$$

From these equations, the momentum can be written as

$$p_x(t) = -\frac{eE_0}{\Omega}\sin\Omega t \tag{5.12}$$

The *x*- component of the velocity is given by

$$v_x = \frac{\partial \varepsilon_p}{\partial p_x} \tag{5.13}$$

On solving this equation, if one considers $p_y = 0$, the velocity can be written as

$$v_x(t) = -v\,\mathrm{sgn}(\sin\Omega t) \tag{5.14}$$

If there are n_s particles per unit area, the corresponding AC electric current is given by

$$j_x(t) = evn_s\,\mathrm{sgn}(\sin\Omega t) \tag{5.15}$$

or,

$$j_x(t) = en_s v\frac{4}{\pi}\left[\sin\Omega t + \frac{1}{3}\sin 3\Omega t + \frac{1}{5}\sin 5\Omega t + \ldots\right] \tag{5.16}$$

Therefore, this simple classical model shows that the current density contains all the Fourier harmonics with the amplitude j_m (m=1,3,5…). The higher order components decreases very slowly with the harmonic order as $j_m=1/m$.

If we make a simple estimation for a carrier density $n_s=6\times10^{12}$ cm^{-2} and the electron velocity $v=10^8$ cm s^{-1}, the current density results in a huge value of $j_0=100$ Amp/cm. This simple formalism gives a reasonable hint that, on applying a modest electric field, higher harmonics could be generated. To study this phenomenon, we have used our intense THz source to investigate the possibility of frequency multiplication at THz frequencies.

5.7 Investigation of the nonlinear response of graphene using intense THz source

For the two graphene samples from Kyushu University and from NTT, we have used two different intense THz sources available at the INRS (discussed in Chapter 2 and Chapter 4) for the nonlinearity measurement. The experimental set-up is shown in Figure 41.

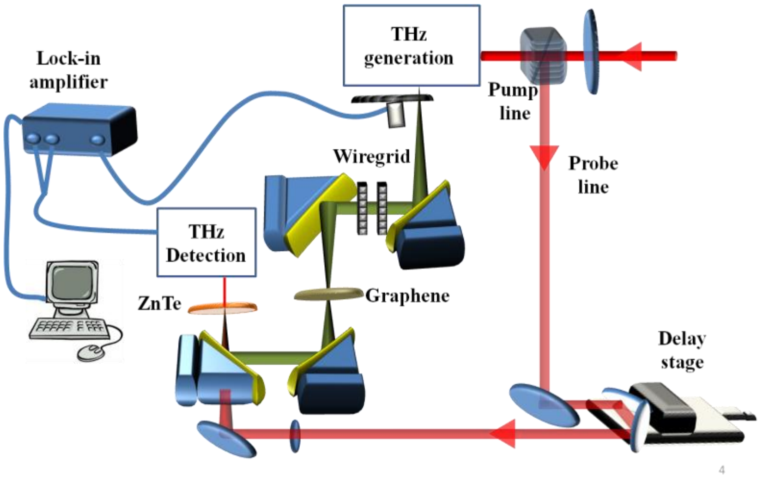

Figure 41. Typical experimental set-up for nonlinear graphene spectroscopy. The THz is generated by optical rectification either in large aperture ZnTe or LiNbO$_3$ crystal. The generated THz signal is focused using off-axis mirrors. The graphene sample is placed at the focus. The THz electric field is changed by set of wire-grid polarizers. The transmitted THz signal is detected using EO sampling in ZnTe crystal

5.7.1 Measurement of the graphene sample fabricated by Kyushu University

For this measurement, we used an intense THz source based on the tilted-pulse-front technique in $LiNbO_3$ crystal discussed in Chapter 2. In this experiment, the energy of the intense THz pulses was 0.55 μJ, measured using a pyroelectric detector calibrated at THz frequencies (Microtech Instrument). The spot size of the THz beam at focus was measured to be ~0.76 mm using a pyroelectric IR camera (ElectroPhysics, model PV320). For a measured THz pulse duration of 1 ps, the maximum THz electric field is evaluated to be 210 kV/cm. We have used wire-grid polarizers to vary the THz electric field on the sample. The THz signal is detected via EO sampling in a 0.5 mm thick ZnTe crystal. Different wire-grid angles were used, and the corresponding THz electric field is shown in Table 4.

Table 4. Wire grid angle and corresponding electric field

Wire grid angle (degree)	THz electric field (kV/cm)
80	210
60	170
50	135
40	95
35	75
20	30

The sample is kept perpendicular to the incoming THz beam. To investigate the THz-field-dependent nonlinearity, the THz electric field is measured for the graphene sample on the SiC substrate (Sample), and for the SiC substrate

(Substrate) only. The measured THz electric field through the Sample and Substrate, and their corresponding spectra are shown in Figure 42.

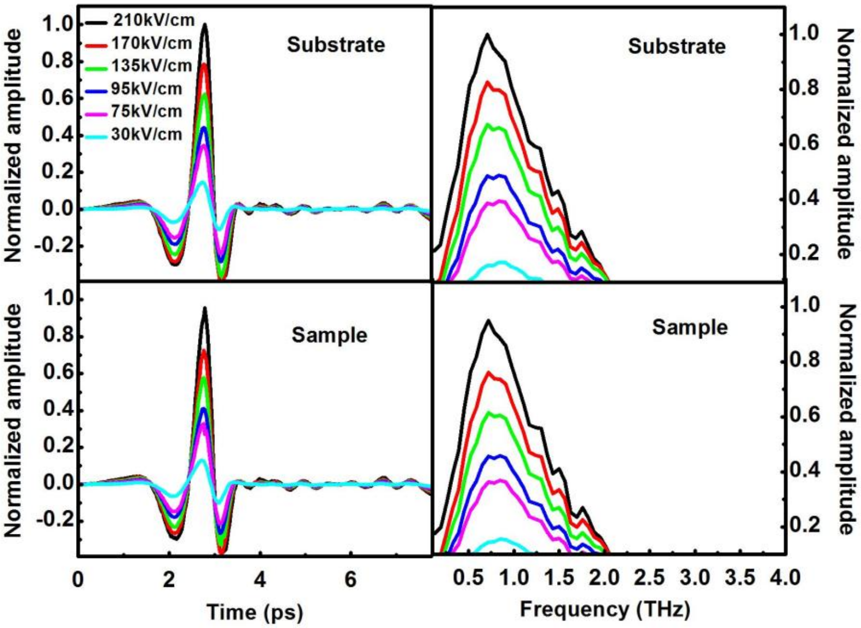

Figure 42. The electric field and corresponding spectrum through the (a) Substrate (SiC) (b) Sample (graphene over SiC substrate)

To investigate the THz-field-dependent nonlinearity, we extracted the normalized transmission of the THz electric field through graphene. For this purpose we took the ratio $|E(\omega)_{Sample}|/|E(\omega)_{Substrate}|$ between the spectral amplitude of the THz pulse transmitted through the graphene sample (on a SiC substrate) $|E(\omega)_{Sample}|$ and through the SiC substrate alone $|E(\omega)_{Substrate}|$. The corresponding ratios are shown in Figure 43.

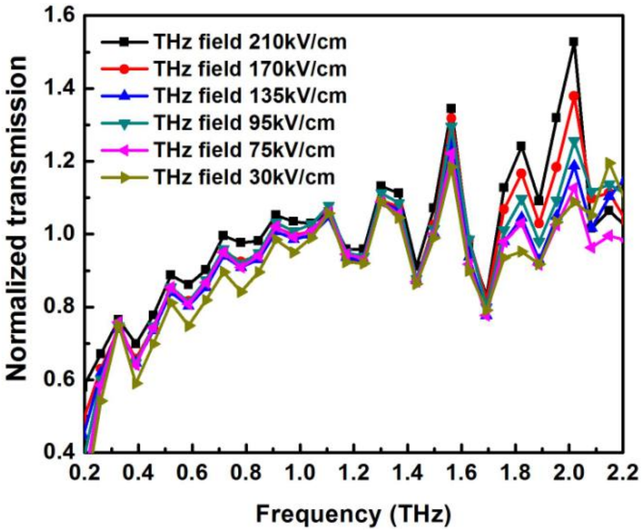

Figure 43. Normalized transmission through the graphene sample for different THz electric field strengths

As can be seen in Figure 43, the spectral ratio of graphene to substrate exceeds unity at a frequency of 1.6 THz and for the range of frequency between1.8 and 2.1 THz. Further, this increase is dependent on the THz-electric-field strength. As we decrease the input THz electric field, this ratio decreases, reaching approximately 1 for a THz electric field of 30 kV/cm.

One of the big limitations of this measurement is the size of the sample. The graphene sample provided by Kyushu University is quite small (3mm × 5mm). Therefore, it is challenging to find the right position on the sample for the measurement, which requires that the THz field is not clipped and making sure that the graphene layer is also there.

5.7.2 Measurement of the graphene sample fabricated by NTT

For the measurements using graphene samples fabricated by NTT, we have used our intense THz source based on optical rectification in a large aperture ZnTe, discussed in Chapter 4. In this experiment, the energy of the intense THz pulses was 0.5 μJ, measured using a pyroelectric detector calibrated at THz frequencies (Microtech Instrument). The spot size of the THz beam at focus was measured to be ~1.2 mm using a pyroelectric IR camera (ElectroPhysics, model PV320). For a measured THz pulse duration of 1 ps, the maximum THz electric field is evaluated to be 133 kV/cm. We have used wire-grid polarizers to vary the THz electric field on the sample. The measurements were performed for four THz peak electric fields: 133 kV/cm, 93 kV/cm, 67 kV/cm and 40 kV/cm. The THz wave transmitted through the sample is detected using electro-optic sampling in another ZnTe crystal with a thickness of 0.5 mm.

To determine the change in the transmission of the THz field through the graphene sample as a function of the peak THz electric field, the sample and the substrate are placed normal to the incoming THz beam, as shown in Figure 41. In these measurements, we have rotated the angle of the wire-grid polarizer to change the THz electric field incident on our graphene on SiC substrate sample (referred from here on as the graphene sample) and on just the bare SiC substrate. The transmitted THz electric field through the graphene sample and the SiC substrate alone are measured for different wire-grid angles. The measurement is taken at THz energies of 100%, 70%, 50%, and 30%. The THz electric field transmitted through the Sample and Substrate, and its corresponding spectrum is shown in Figure 44.

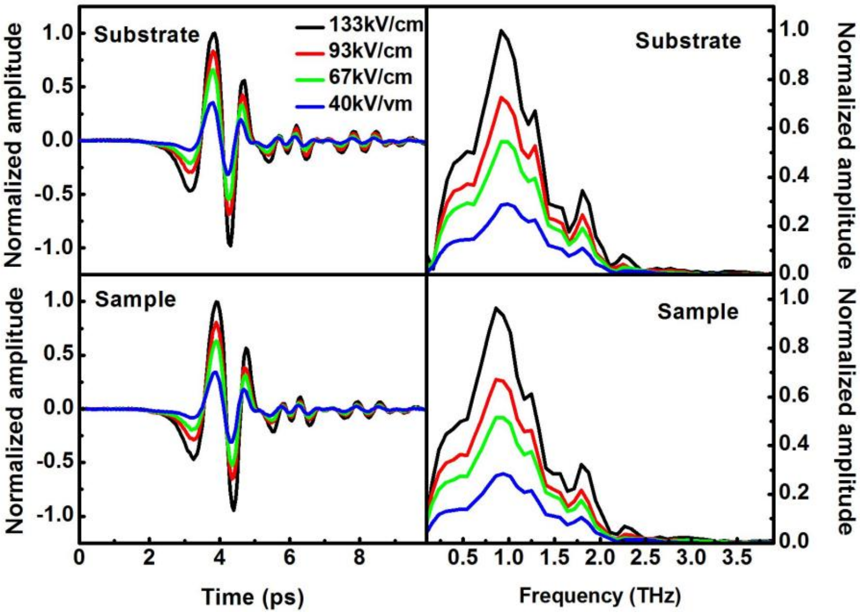

Figure 44. THz electric field and corresponding spectrum through(a) Substrate (SiC) (b) Sample (graphene over SiC substrate)

Figure 45 shows the normalized transmission $\left|E(\omega)_{Sample}\right| / \left|E(\omega)_{Substrate}\right|$ as a function of the THz frequency.

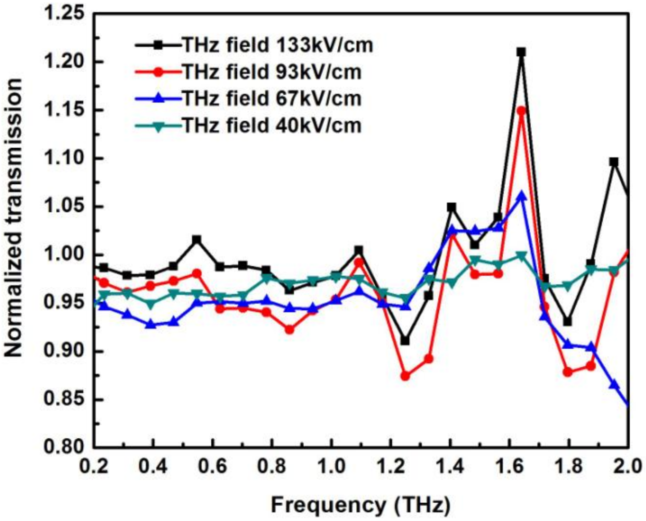

Figure 45. Normalized transmission through the graphene sample for different THz electric field strengths

We observe an increase in THz transmission for a broad range of THz frequencies ranging from 1.4 THz to1.7 THz. The other interesting observation is that this increase depends on the THz electric field value. We observe a maximum increase in THz transmission of 21% for a maximum THz electric field of 133 kV/cm at a THz frequency of 1.64 THz. As we reduce the THz field to 93 kV/cm, the spectral ratio is reduced to 15%. On further reducing the THz electric field to 67 kV/cm, the ratio goes down to 6%, and finally it disappears at 40 kV/cm.

Since the graphene sample (on SiC substrate) should be more conducting than the SiC substrate alone, we expect the THz transmission through the graphene sample to be less than for the SiC substrate only. Thus, one would expect that the ratio of the $\left|E(\omega)_{Sample}\right| / \left|E(\omega)_{Substrate}\right|$ between the spectral amplitude of the THz pulse transmitted through the Sample $E(\omega)_{Sample}$ and through the Substrate alone $E(\omega)_{Substrate}$ should always be less than one. Unlike what we expected, we see an increase in relative transmission at certain frequencies. We further find that this increase is dependent on the THz electric field strength, and is consistent for two different samples grown, with different techniques, using two different THz sources (with different spectra).

5.8 Discussion

The results described in this Chapter are one of the first experimental results showing the nonlinear response of graphene at THz frequencies. The results show that graphene interacts strongly with THz radiations and can be a potential candidate for THz frequency up-conversion. The transmission greater than one for can be attributed to frequency multiplication at THz frequencies as can discussed using very simple model in section 5.6. We are currently working on a theoretical model for this experimental observation in collaboration with a theorist at the University of Tokyo, Japan.

Chapter 6

Conclusion

The main objective of this thesis was to develop an intense THz source and use it to study the nonlinear THz response of semiconductors and graphene.

For the nonlinear spectroscopy of semiconductors and graphene, the main requirement for the THz source was high electric field and good signal-to-noise ratio. When this project was started, there was already an intense THz source available at ALLS, based on a large aperture ZnTe crystal, using 50mJ laser energy, generating 200 kV/cm THz electric fields. The problem with this source was the low signal-to-noise ratio, as this source was based on a 100 Hz laser system. The other limitation was the laser beam time, as ALLS is a user facility and the 100 Hz laser is used by many other users, which makes the laser beam time access quite competitive. Therefore, the idea was to develop an intense THz source using a laser that is relatively more available, with much less laser energy but capable to generate comparable THz electric fields with a high signal-to-noise ratio. With this aim in mind, we started working on the development of an intense THz source using the 5 mJ multi kHz laser facility at ALLS, which was a relatively less occupied laser system.

6.1 Intense THz source development using the tilted-pulse-front technique in $LiNbO_3$ crystal

The first objective was to demonstrate an intense THz source using a tilted-pulse-front technique in $LiNbO_3$ crystals. For this purpose, we have used a multi-kHz laser source with 5 mJ energy, 30 fs pulse duration, and 1 kHz repetition rate. The maximum energy used at the $LiNbO_3$ crystal to generate THz radiation was 1 mJ. With this pump laser energy, we were able to generate THz radiation with energy as high as 0.6 μJ, with peak electric fields of 160 kV/cm. The signal-to-noise ratio of the $LiNbO_3$ based THz source is measured to be 100 times better than the signal-to-noise ratio of the ZnTe based source.

6.2 THz detection using spectral domain interferometry

At the time of the THz source characterization, we experienced the problem of over-rotation in measuring THz pulse waveform using the conventional electro-optic (EO) sampling technique. In EO sampling, the induced phase difference is directly proportional to the thickness of the crystal. Therefore, the problem of over-rotation is even more severe when thick detection crystals are used, which is an important requirement to achieve good spectral resolution, a must for spectroscopic purposes. To overcome the limitation of over rotation and to simplify the detection set-up, we proposed a novel technique based on spectral domain interferometry. We also experimentally demonstrated the possibility of THz detection using this technique. Theoretically, this technique can measure THz signal that is almost 18,000 times higher than what can be measured with the standard EO sampling technique.

6.3 Nonlinear THz spectroscopy of semiconductors

Once the source was developed and characterized, the next step was to use this source for nonlinear spectroscopy of semiconductors. In this regard, we used an optical-pump high-power THz-probe spectroscopy technique for the characterization of GaAs samples. When the 800 nm optically-pumped GaAs sample was probed and pumped with an intense THz electric field, absorption bleaching of intense THz pulses was observed. The absorption bleaching is the result of intervalley scattering of electrons between the Γ and L valley of the conduction band. We have used intervalley-scattering-based Drude model to simulate our results. The simulation results are in good agreement with our experiments observations.

Moving further, we changed the optical pump fluence and hence the carrier density in the conduction band and investigated its effect on THz-induced absorption bleaching. The level of THz-induced absorption bleaching initially increases with an increase in the carrier density. However, on further increasing the carrier density, THz-induced absorption bleaching starts to decrease, and eventually relaxes to almost zero. The main reason for this trend for the level of THz-induced absorption bleaching was the decrease in carrier mobility in the Γ valley with an increase in the carrier density. We added this decrease in the mobility parameter in our simulation. The simulation results are found to be in good agreement with our experimental findings.

6.4 THz linear and nonlinear spectroscopy of graphene samples

One of the objectives of this project was to perform THz spectroscopy of graphene samples. For this purpose, we have collaborated with two groups in Japan that could fabricate graphene samples; NTT and Kyushu University. The first sample we probed was monolayer graphene on a SiC substrate from Kyushu University, Japan. The problem with this sample was its small dimension. The substrate on which the sample was fabricated was 3 mm × 5 mm. Since THz wavelengths are long (1 THz = 300 μm), experimentally it was quite difficult to use this sample. Later we collaborated with NTT and received a sample from them. The samples from NTT were fabricated on a bigger substrate (10 mm × 10 mm). First, we linearly characterized the samples. We extracted their sheet conductivity using THz spectroscopy. The sheet conductivity of the NTT sample was found to be $0.6 \times 10^{-3}\Omega^{-1}$, and it was constant as a function of frequency for the range of 0.1 - 2.5 THz, whereas the sheet conductivity extracted from the Kyushu university sample was varying from 0 to $0.7 \times 10^{-3}\Omega^{-1}$.

After the linear characterization was done, we used our intense THz source for the nonlinear spectroscopy of graphene. We performed THz electric field dependent measurements, in which we changed the incident THz electric field at the graphene sample (or substrate) using wire-grid polarizers. When we extracted the transmission through the graphene samples, we found a very interesting behavior, that is, THz electric field dependent up-conversion is observed in our graphene samples. In particular, we observed a similar response in both of them. To the best of our knowledge, this is one of the first nonlinear THz result in graphene. We are in collaboration with a theoretical group in Japan to model these results.

6.5 Future perspective

6.5.1 Up-grading the $LiNbO_3$ source using the 100 Hz laser system

One objective of developing a THz source using the 5 mJ multi-kHz laser was to acquire the know-how of the THz source based on the tilted-pulse-front method, so that eventually it could be upgraded for pumping using the 50 mJ, 100 Hz based laser source. In this way, the INRS could become one of the facilities with the most intense THz source in the world.

6.5.2 THz detection improvements

We have demonstrated a new detection technique using spectral domain interferometry. There are several changes that can be incorporated to improve the proposed technique. For example, instead of a glass plate, a Mach-Zehnder configuration can be used to work around the zero optical path difference, where the SNR of the SDI is maximum. Several applications of this method are possible. For instance, a simultaneous reflection transmission set-up can be built using a single detection line.

6.5.3 Linear and nonlinear THz spectroscopy of various semiconductors and graphene

There are several proposed experiments for linear and nonlinear spectroscopy of semiconductors and graphene samples. These include pumping graphene with different frequencies and probing it with intense THz electric fields, performing THz-pump THz-probe experiments on graphene samples. The first experiment was done on monolayer graphene, but all the proposed experiments can be performed on bilayer and multilayer graphene as well.

List of variables

Polarization	P
Optical pump electric field	E_{opt}
Nonlinear susceptibility	$\chi^{(n)}$
Angular frequency of the optical pump pulse	$\omega(=\omega_2)$
Difference between frequency components of broadband laser pulse	Ω
Sum frequency component in optical rectification $(\omega+\Omega)$	ω_1
Radiated THz electric field	E_{THz}
Wave vector for optical pulse	k
Beam waist	ω_0
Wave vector for THz pulse	k_{THz}
Phase mismatch between the optical and THz pulse	Δk
Coherence length	L_c
Wavelength	λ
Refractive index of detection ZnTe crystal for 800nm beam	n_0
Coordinates of the index ellipsoid for ZnTe detection crystal	x, y, z
Electric field along the coordinates of index ellipsoid	E_x, E_y, E_z
Electro-optic coefficient of ZnTe crystal	r_{41}
Phase delay	ϕ
Thickness of electro-optic crystal	d
Difference of the refractive index for the two axes	Δn
Input laser intensity	I_0
Output laser intensity	I
Static phase delay in ZnTe crystal	ϕ_0
THz generation efficiency	η_{THz}
Effective nonlinear coefficient	d_{eff}
Free space permittivity	ε_0
Velocity of light	c
Nonlinear crystal length	L_{max}
THz Absorption coefficient	α_{THz}
Group velocity of optical pulse	n_{opt}^{gr}
Phase velocity of the THz pulse	n_{THz}^{ph}
Phase matching angle	θ_c
Angle of incidence at the grating	α
Angle of diffraction from the grating	β
Order of grating	m
Number of groves per millimeter in the grating	N
Object distance	S_0
Image distance	S_i
Demagnification ratio (S_0/S_i)	F

Optical pulse duration	τ_{opt}
Refractive index of optical beam in $LiNbO_3$ crystal	n_{opt}
Free-space impedance	η_0
THz peak electric field	E_0
THz energy	W
THz temporal profile	$g(t)$
Bandwidth of the laser pulse	$\Delta\lambda$
Optical path difference	L_{OPD}
Total bandwidth of interfering signal	Δk_{tot}
Number of pixels of the CCD camera	N_p
Distance per pixel	Δd
Signal to noise ratio of SDI signal	SNR_{SDI}
Standard deviation	SD
Phase stability of standard deviation	$\left\langle \phi^2 \right\rangle$
Minimum optical path difference measured using SDI	$\Delta z_{minimum}$
Propagation constant	$\beta(\omega)$
Phase correction term for SDI	$\overline{\Phi}$
2nd order dispersion compensation component	a_1
3rd order dispersion compensation component	a_2
Spectral range of spectrometer	$\Delta\Lambda$
Number of illuminated groves at the CCD camera	$\mathbb{N}$
First order spectral resolution of the diffraction pattern	$\Delta\hat{\lambda}_{grating}$
Electric field	E
Magnetic field	H
Current density	J
Thickness of sample	d
Index of sample	n_r
Admittance	Y
Incident electric field	E_{inc}
Transmitted electric field	E_{trans}
Transmission coefficient	t
Conductivity	$\tilde{\sigma}$
Transmission through a thin conducting film	t_{film}
Impedance of free space	Z_0
Transmission coefficient for the unexcited dielectric slab	t_{subs}
Transmission function for a photoexcited layer with respect to the background unexcited substrate	$T(\omega)$
Pump induced change in conductivity	$\Delta\sigma$
Effective mass	m^*
Plank's constant	h
collisional damping rate	$1/\tau$
Mean velocity distribution	v
Electron density	n
Electron density in Γ and L valley	n_Γ, n_L

Drift velocities of electrons in *Γ* and *L* valley	v_{Γ}, v_L
Intravalley scattering times in *Γ* and *L* valley	τ_{Γ}, τ_L
Effective masses of electron in *Γ* and *L* valley	m^*_{Γ} , m^*_L
Intervalley scattering rates from Γ to L, and L to Γ valleys	$\tau^{-1}_{L\Gamma}$, $\tau^{-1}_{\Gamma L}$
Average kinetic energy of electron	ε_{Γ}
Smoothening parameter	b
Nonparabolicity parameter for G and L valley	α_{Γ}, α_L
Effective masses at the Γ and L valley minima	$m^*_{\Gamma 0}$, m^*_{L0}
Transmitted THz waveforms, excited and unexcited GaAs	$E_{trans\_P}(\omega)$, $E_{trans\_R}(\omega)$
Level of absorption bleaching	Ψ
Electron mobility	μ
Electron charge	e

References

[1] N. Nagai, R. Kumazawa, and R. Fukasawa, "Direct evidence of inter-molecular vibrations by THz spectroscopy," *Chemical Physics Letters,* Vol. 413, p. 495, 2005.

[2] S. E. Whitmire, D. Wolpert, A. G. Markelz, J. R. Hillebrecht, J. Galan, and R. R. Birge, "Protein Flexibility and Conformational State: A Comparison of Collective Vibrational Modes of Wild-Type and D96N Bacteriorhodopsin," *Biophysical journal,* Vol. 85, p. 1269, 2003.

[3] D. M. Mittleman, R. H. Jacobsen, R. Neelamani, R. G. Baraniuk, and M. C. Nuss, "Gas sensing using terahertz time-domain spectroscopy," *Applied Physics B,* Vol. 67, p. 379, 1998.

[4] D. M. Mittleman, M. C. Nuss, and V. L. Colvin, "Terahertz spectroscopy of water in inverse micelles," *Chemical Physics Letters,* Vol. 275, p. 332, 1997.

[5] I. H. Libon, M. Hempel, S. Seitz, N. E. Hecker, J. Feldmann, A. Hayd*, et al.*, "THz spectroscopy of polar liquids," *Proc. SPIE* 3617, Terahertz Spectroscopy and Applications, p. 24, 1999.

[6] W. Knap, Y. Deng, S. Rumyantsev, and M. S. Shur, "Resonant detection of subterahertz and terahertz radiation by plasma waves in submicron field-effect transistors," *Applied Physics Letters,* Vol. 81, p. 4637, 2002.

[7] X. G. Peralta, S. J. Allen, M. C. Wanke, N. E. Harff, J. A. Simmons, M. P. Lilly*, et al.*, "Terahertz photoconductivity and plasmon modes in double-quantum-well field-effect transistors," *Applied Physics Letters,* Vol. 81, p. 1627, 2002.

[8] M. Diem, T. Koschny, and C. M. Soukoulis, "Wide-angle perfect absorber/thermal emitter in the terahertz regime," *Physical Review B,* Vol. 79, p. 033101, 2009.

[9] A. C. Warren, J. M. Woodall, J. L. Freeouf, D. Grischkowsky, D. T. McInturff, M. R. Melloch*, et al.*, "Arsenic precipitates and the semi-insulating properties of GaAs buffer layers grown by low-temperature molecular beam epitaxy," *Appl. Phys. Lett.,* Vol. 57, p. 1331, 1990.

[10] J. T. Kindt and C. A. Schmuttenmaer, "Far-Infrared Dielectric Properties of Polar Liquids Probed by Femtosecond Terahertz Pulse Spectroscopy," *The J. of Phys. Chem.,* Vol. 100, p. 10373, 1996.

[11] B. B. Hu and M. C. Nuss, "Imaging with terahertz waves," *Opt. Lett.,* Vol. 20, p. 1716, 1995.

[12] D. M. Mittleman, R. H. Jacobsen, and M. C. Nuss, "T-ray imaging," *IEEE J. Sel. Top. Quantum Electron.,* Vol. 2, p. 679, 1996.

[13] P. Gaal, K. Reimann, M. Woerner, T. Elsaesser, R. Hey, and K. H. Ploog, "Nonlinear Terahertz Response of n-Type GaAs," *Phys. Rev. Lett.,* Vol. 96, p. 187402, 2006.

[14] P. Gaal, W. Kuehn, K. Reimann, M. Woerner, T. Elsaesser, R. Hey, *et al.*, "Carrier-wave Rabi flopping on radiatively coupled shallow donor transitions in n-type GaAs," *Phys. Rev. B,* Vol. 77, p. 235204, 2008.

[15] Y. Shen, T. Watanabe, D. A. Arena, C. C. Kao, J. B. Murphy, T. Y. Tsang, *et al.*, "Nonlinear Cross-Phase Modulation with Intense Single-Cycle Terahertz Pulses," *Phys. Rev. Lett.,* Vol. 99, p. 043901, 2007.

[16] Y. Shen, G. L. Carr, J. B. Murphy, T. Y. Tsang, X. Wang, and X. Yang, "Spatiotemporal control of ultrashort laser pulses using intense single-cycle terahertz pulses," *Phys. Rev. A,* Vol. 78, p. 043813, 2008.

[17] J. Hebling, K.-L. Yeh, K. A. Nelson, and M. C. Hoffmann, "High-Power THz Generation, THz Nonlinear Optics, and THz Nonlinear Spectroscopy," *IEEE J. Sel. Top. Quantum Electron.,* Vol. 14, p. 345, 2008.

[18] H. Wen, M. Wiczer, and A. M. Lindenberg, "Ultrafast electron cascades in semiconductors driven by intense femtosecond terahertz pulses," *Phys. Rev. B,* Vol. 78, p. 125203, 2008.

[19] M. C. Hoffmann, J. Hebling, H. Y. Hwang, K.-L. Yeh, and K. A. Nelson, "Impact ionization in InSb probed by terahertz pump terahertz probe spectroscopy," *Phys. Rev. B,* Vol. 79, p. 161201, 2009.

[20] L. Razzari, F. H. Su, G. Sharma, F. Blanchard, A. Ayesheshim, H. C. Bandulet, *et al.*, "Nonlinear ultrafast modulation of the optical absorption of intense few-cycle terahertz pulses in n-doped semiconductors," *Phys. Rev. B,* Vol. 79, p. 193204, 2009.

[21] M. C. Hoffmann, J. Hebling, H. Y. Hwang, K.-L. Yeh, and K. A. Nelson, "THz-pump/THz-probe spectroscopy of semiconductors at high field strengths [Invited]," *J. Opt. Soc. Am. B,* Vol. 26, p. A29, 2009.

[22] M. C. Hoffmann, N. C. Brandt, H. Y. Hwang, K.-L. Yeh, and K. A. Nelson, "Terahertz Kerr effect," *Appl. Phys. Lett.,* Vol. 95, p. 231105, 2009.

[23] T. Ogawa, S. Watanabe, N. Minami, and R. Shimano, "Room temperature terahertz electro-optic modulation by excitons in carbon nanotubes," *Appl. Phys. Lett.,* Vol. 97, p. 041111, 2010.

[24] M. C. Hoffmann and D. Turchinovich, "Semiconductor saturable absorbers for ultrafast terahertz signals," *Appl. Phys. Lett.,* Vol. 96, p. 151110, 2010.

[25] T. Kampfrath, A. Sell, G. Klatt, A. Pashkin, S. Mahrlein, T. Dekorsy, *et al.*, "Coherent terahertz control of antiferromagnetic spin waves," *Nat Photon,* Vol. 5, p. 31, 2011.

[26] F. Blanchard, L. Razzari, H. C. Bandulet, G. Sharma, R. Morandotti, J. C. Kieffer, *et al.*, "Generation of 1.5 µJ single-cycle terahertz pulses by optical rectification from a large aperture ZnTe crystal," *Opt. Express,* Vol. 15, p. 13212, 2007.

[27] M. Bass, P. A. Franken, J. F. Ward, and G. Weinreich, "Optical Rectification," *Physical Review Letters,* Vol. 9, p. 446, 1962.

[28] K. H. Yang, P. L. Richards, and Y. R. Shen, "Generation of Far-Infrared Radiation by Picosecond Light Pulses in LiNbO[sub 3]," *Applied Physics Letters*, Vol. 19, p. 320, 1971.

[29] A. Rice, Y. Jin, X. F. Ma, X. C. Zhang, D. Bliss, J. Larkin, *et al.*, "Terahertz optical rectification from <110> zinc-blende crystals," *Applied Physics Letters*, Vol. 64, p. 1324, 1994.

[30] T. J. Carrig, G. Rodriguez, T. S. Clement, A. J. Taylor, and K. R. Stewart, "Scaling of terahertz radiation via optical rectification in electro-optic crystals," *Applied Physics Letters,* Vol. 66, p. 121, 1995.

[31] Q. Chen and X. C. Zhang, "Polarization modulation in optoelectronic generation and detection of terahertz beams," *Applied Physics Letters,* Vol. 74, p. 3435, 1999.

[32] P. Y. Han and X. C. Zhang, "Coherent, broadband midinfrared terahertz beam sensors," *Applied Physics Letters,* Vol. 73, p. 3049, 1998.

[33] A. Nahata, A. S. Weling, and T. F. Heinz, "A wideband coherent terahertz spectroscopy system using optical rectification and electro-optic sampling," *Applied Physics Letters,* Vol. 69, p. 2321, 1996.

[34] X. C. Zhang, Y. Jin, and X. F. Ma, "Coherent measurement of THz optical rectification from electro-optic crystals," *Applied Physics Letters,* Vol. 61, p. 2764, 1992.

[35] L. Xu, X. C. Zhang, and D. H. Auston, "Terahertz beam generation by femtosecond optical pulses in electro-optic materials," *Applied Physics Letters,* Vol. 61, p. 1784, 1992.

[36] Y.-S. Lee, *Principles of Terahertz Science and Technology*. New York: Springer, 2008.

[37] B. B. Hu, X. C. Zhang, D. H. Auston, and P. R. Smith, "Free-space radiation from electro-optic crystals," *Applied Physics Letters,* Vol. 56, p. 506, 1990.

[38] A. Nahata, D. H. Auston, T. F. Heinz, and C. Wu, "Coherent detection of freely propagating terahertz radiation by electro-optic sampling," *Applied Physics Letters*, Vol. 68, p. 150, 1996.

[39] M. Nagai, K. Tanaka, H. Ohtake, T. Bessho, T. Sugiura, T. Hirosumi, *et al.*, "Generation and detection of terahertz radiation by electro-optical process in GaAs using 1.56 mu m fiber laser pulses," *Applied Physics Letters*, Vol. 85, p. 3974, 2004.

[40] A. Syouji, S. Saito, K. Sakai, M. Nagai, K. Tanaka, H. Ohtake, *et al.*, "Evaluation of a terahertz wave spectrum and construction of a terahertz wave-sensing system using a Yb-doped fiber laser," *Journal of the Optical Society of America B-Optical Physics*, Vol. 24, p. 2006, 2007.

[41] Q. Wu, T. D. Hewitt, and X. C. Zhang, "Two-dimensional electro-optic imaging of THz beams," *Applied Physics Letters,* Vol. 69, p. 1026, 1996.

[42] P. U. Jepsen, C. Winnewisser, M. Schall, V. Schyja, S. R. Keiding, and H. Helm, "Detection of THz pulses by phase retardation in lithium tantalate," *Physical Review E,* Vol. 53, p. R3052, 1996.

[43] M. Tonouchi, "Cutting-edge terahertz technology," *Nat Photon,* Vol. 1, p. 97, 2007.

[44] Q. Wu and X. C. Zhang, "7 terahertz broadband GaP electro-optic sensor," *Applied Physics Letters,* Vol. 70, p. 1784, 1997.

[45] A. C. Warren, N. Katzenellenbogen, D. Grischkowsky, J. M. Woodall, M. R. Melloch, and N. Otsuka, "Subpicosecond, freely propagating electromagnetic pulse generation and detection using GaAs:As epilayers," *Applied Physics Letters*, Vol. 58, p. 1512, 1991.

[46] P. C. M. Planken, H. K. Nienhuys, H. J. Bakker, and T. Wenckebach, "Measurement and calculation of the orientation dependence of terahertz pulse detection in ZnTe," *Journal of the Optical Society of America B-Optical Physics,* Vol. 18, p. 313, 2001.

[47] C. Kübler, R. Huber, and A. Leitenstorfer, "Ultrabroadband terahertz pulses: generation and field-resolved detection," *Semiconductor Science and Technology,* Vol. 20, p. S128, 2005.

[48] G. Gallot, J. Zhang, R. W. McGowan, T.-I. Jeon, and D. Grischkowsky, "Measurements of the THz absorption and dispersion of ZnTe and their relevance to the electro-optic detection of THz radiation," *Applied Physics Letters,* Vol. 74, p. 3450, 1999.

[49] J. Hebling, A. G. Stepanov, G. Almási, B. Bartal, and J. Kuhl, "Tunable THz pulse generation by optical rectification of ultrashort laser pulses with tilted pulse fronts," *Applied Physics B: Lasers and Optics,* Vol. 78, p. 593, 2004.

[50] A. Schneider, M. Neis, M. Stillhart, B. Ruiz, R. U. A. Khan, and P. Gunter, "Generation of terahertz pulses through optical rectification in organic DAST crystals: theory and experiment," *Journal of the Optical Society of America B-Optical Physics,* Vol. 23, p. 1822, 2006.

[51] F. Pan, G. Knopfle, C. Bosshard, S. Follonier, R. Spreiter, M. S. Wong*, et al.*, "Electro-optic properties of the organic salt 4-N,N-dimethylamino-4[prime]-N[prime]-methyl-stilbazolium tosylate," *Applied Physics Letters,* Vol. 69, p. 13, 1996.

[52] M. Walther, K. Jensby, S. R. Keiding, H. Takahashi, and H. Ito, "Far-infrared properties of DAST," *Opt Lett,* Vol. 25, p. 911, 2000.

[53] M. Schall, M. Walther, and P. Uhd Jepsen, "Fundamental and second-order phonon processes in CdTe and ZnTe," *Physical Review B,* Vol. 64, p. 094301, 2001.

[54] K. L. Yeh, M. C. Hoffmann, J. Hebling, and K. A. Nelson, "Generation of 10 mu J ultrashort terahertz pulses by optical rectification," *Applied Physics Letters,* Vol. 90, p. 171121, 2007.

[55] J. A. L'huillier, G. Torosyan, M. Theuer, C. Rau, Y. Avetisyan, and R. Beigang, "Generation of THz radiation using bulk, periodically and aperiodically poled lithium niobate – Part 2: Experiments," *Applied Physics B: Lasers and Optics,* Vol. 86, p. 197, 2007.

[56] A. Schneider, M. Stillhart, and P. Gunter, "High efficiency generation and detection of terahertz pulses using laser pulses at telecommunication wavelengths," *Opt Express,* Vol. 14, p. 5376, 2006.

[57] T. Loffler, T. Hahn, M. Thomson, F. Jacob, and H. G. Roskos, "Large-area electro-optic ZnTe terahertz emitters," *Opt Express,* Vol. 13, p. 5353, 2005.

[58] M. C. Hoffmann, K. L. Yeh, J. Hebling, and K. A. Nelson, "Efficient terahertz generation by optical rectification at 1035 nm," *Opt Express,* Vol. 15, p. 11706, 2007.

[59] D. Redfield and W. J. Burke, "Optical absorption edge of LiNbO[sub 3]," *Journal of Applied Physics,* Vol. 45, p. 4566, 1974.

[60] J. A. L'huillier, G. Torosyan, M. Theuer, Y. Avetisyan, and R. Beigang, "Generation of THz radiation using bulk, periodically and aperiodically poled lithium niobate – Part 1: Theory," *Applied Physics B: Lasers and Optics,* Vol. 86, p. 185, 2007.

[61] D. H. Auston, K. P. Cheung, J. A. Valdmanis, and D. A. Kleinman, "Cherenkov Radiation from Femtosecond Optical Pulses in Electro-Optic Media," *Physical Review Letters,* Vol. 53, p. 1555, 1984.

[62] D. A. Kleinman and D. H. Auston, "Theory of electro-optic shock radiation in nonlinear optical media," *IEEE Journal of Quantum Electronics,* Vol. 20, p. 964, 1984.

[63] M. Schall, H. Helm, and S. R. Keiding, "Far Infrared Properties of Electro-Optic Crystals Measured by THz Time-Domain Spectroscopy," *International Journal of Infrared and Millimeter Waves,* Vol. 20, p. 595, 1999.

[64] J. Hebling, G. Almasi, I. Kozma, and J. Kuhl, "Velocity matching by pulse front tilting for large area THz-pulse generation," *Opt. Express,* Vol. 10, p. 1161, 2002.

[65] A. G. Stepanov, J. Hebling, and J. Kuhl, "Efficient generation of subpicosecond terahertz radiation by phase-matched optical rectification using ultrashort laser pulses with tilted pulse fronts," *Applied Physics Letters,* Vol. 83, p. 3000, 2003.

[66] L. Palfalvi, J. Hebling, G. Almasi, A. Peter, K. Polgar, K. Lengyel, *et al.*, "Nonlinear refraction and absorption of Mg doped stoichiometric and congruent LiNbO[sub 3]," *Journal of Applied Physics,* Vol. 95, p. 902, 2004.

[67] L. Palfalvi, J. Hebling, J. Kuhl, A. Peter, and K. Polgar, "Temperature dependence of the absorption and refraction of Mg-doped congruent and stoichiometric LiNbO[sub 3] in the THz range," *Journal of Applied Physics,* Vol. 97, p. 123505, 2005.

[68] F. Blanchard, G. Sharma, L. Razzari, X. Ropagnol, H.-C. Bandulet, F. Vidal, *et al.*, "Generation of Intense Terahertz Radiation via Optical Methods " *IEEE Journal of selected topics in quantum electronics,* Vol. 17, p. 5, 2011.

[69] S. P. Jamison, J. Shen, A. M. MacLeod, W. A. Gillespie, and D. A. Jaroszynski, "High-temporal-resolution, single-shot characterization of terahertz pulses," *Opt. Lett.,* Vol. 28, p. 1710, 2003.

[70] K. Y. Kim, B. Yellampalle, A. J. Taylor, G. Rodriguez, and J. H. Glownia, "Single-shot terahertz pulse characterization via two-dimensional electro-optic imaging with dual echelons," *Opt. Lett.*, Vol. 32, p. 1968, 2007.

[71] Y. Kawada, T. Yasuda, H. Takahashi, and S.-i. Aoshima, "Real-time measurement of temporal waveforms of a terahertz pulse using a probe pulse with a tilted pulse front," *Opt. Lett.*, Vol. 33, p. 180, 2008.

[72] J. Fletcher, "Distortion and uncertainty in chirped pulse THz," *Opt. Express*, Vol. 10, p. 1425, 2002.

[73] J. Zhang, B. Rao, L. Yu, and Z. Chen, "High-dynamic-range quantitative phase imaging with spectral domain phase microscopy," *Opt. Lett.*, Vol. 34, p. 3442, 2009.

[74] A. F. Fercher, C. K. Hitzenberger, G. Kamp, and S. Y. El-Zaiat, "Measurement of intraocular distances by backscattering spectral interferometry," *Optics Communications*, Vol. 117, p. 43, 1995.

[75] K. Singh, C. Dion, M. R. Lesk, T. Ozaki, and S. Costantino, "Spectral-domain phase microscopy with improved sensitivity using two-dimensional detector arrays," *Review of Scientific Instruments*, Vol. 82, p. 023706, 2011.

[76] K. Singh, C. Dion, M. Wajszilber, T. Ozaki, M. R. Lesk, and S. Costantino, "Measurement of Ocular Fundus Pulsation in Healthy Subjects Using a Novel Fourier-Domain Optical Coherence Tomography," *Invest Ophthalmol Vis Sci*, Vol. 52, p. 8927, 2011.

[77] M. Wojtkowski, V. Srinivasan, T. Ko, J. Fujimoto, A. Kowalczyk, and J. Duker, "Ultrahigh-resolution, high-speed, Fourier domain optical coherence tomography and methods for dispersion compensation," *Opt. Express*, Vol. 12, p. 2404, 2004.

[78] M. C. Nuss, D. H. Auston, and F. Capasso, "Direct subpicosecond measurement of carrier mobility of photoexcited electrons in gallium arsenide," *Physical Review Letters*, Vol. 58, p. 2355, 1987.

[79] A. C. Schmuttenmaer, "Exploring dynamics in the far-Infrared with terahertz spectroscopy," *Chemical Review*, Vol. 104, p. 1759, 2004.

[80] R. E. Glover, III and M. Tinkham, "Conductivity of superconducting films for photon energies between 0.3 and $40kT_c$," *Physical Review*, Vol. 108, p. 243, 1957.

[81] J. D. Perkins, A. Mascarenhas, Y. Zhang, J. F. Geisz, D. J. Friedman, J. M. Olson, *et al.*, "Nitrogen-activated transitions, level repulsion, and band gap reduction in $GaAs_{1-x}N_x$ with x< 0.03," *Physical Review Letters*, Vol. 82, p. 3312, 1999.

[82] P. R. C. Kent and A. Zunger, "Evolution of III-V nitride alloy electronic structure: The localized to delocalized transition," *Physical Review Letters*, Vol. 86, p. 2613, 2001.

[83] D. Fowler, O. Makarovsky, A. Patana, L. Eaves, L. Geelhaar, and H. Riechert, "Electron conduction in two-dimensional $GaAs_{1-y}N_y$ channels," *Physical Review B*, Vol. 69, p. 153305, 2004.

[84] M. P. Vaughan and B. K. Ridley, "Solution of the Boltzmann equation for calculating the Hall mobility in bulk GaN_xAs_{1-x}," *Physical Review B,* Vol. 72, p. 075211, 2005.

[85] W. Zhang, A. K. Azad, and D. Grischkowsky, "Terahertz studies of carrier dynamics and dielectric response of n-type, freestanding epitaxial GaN," *Applied Physics Letters,* Vol. 82, p. 2841, 2003.

[86] Y. Zhang, A. Mascarenhas, H. P. Xin, and C. W. Tu, "Scaling of band-gap reduction in heavily nitrogen doped GaAs," *Physical Review B,* Vol. 63, p. 161303, 2001.

[87] R. Mouillet, L.-A. de Vaulchier, E. Deleporte, Y. Guldner, L. Travers, and J.-C. Harmand, "Role of nitrogen in the mobility drop of electrons in modulation-doped GaAsN/AlGaAs heterostructures," *Solid State Communications,* Vol. 126, p. 333, 2003.

[88] B. Fluegel, S. Francoeur, A. Mascarenhas, S. Tixier, E. C. Young, and T. Tiedje, "Giant spin-orbit bowing in $GaAs_{1-x}Bi_x$," *Physical Review Letters,* Vol. 97, p. 067205, 2006.

[89] M. Lundstrom, "Fundamentals of carrier transport " *Cambridge University Press, Cambridge,* 2000.

[90] A. Rice, Y. Jin, X. F. Ma, X. C. Zhang, D. Bliss, J. Larkin, *et al.*, "Terahertz optical rectification from <110> zinc-blende crystals," *Appl. Phys. Lett.*, Vol. 64, p. 1324, 1994.

[91] Q. Wu and X. C. Zhang, "Ultrafast electro-optic field sensors," *Appl. Phys. Lett.*, Vol. 68, p. 1604, 1996.

[92] P. C. M. Planken, H.-K. Nienhuys, H. J. Bakker, and T. Wenckebach, "Measurement and calculation of the orientation dependence of terahertz pulse detection in ZnTe," *J. Opt. Soc. Am. B,* Vol. 18, p. 313, 2001.

[93] F. H. Su, F. Blanchard, G. Sharma, L. Razzari, A. Ayesheshim, T. L. Cocker, *et al.*, "Terahertz pulse induced intervalley scattering in photoexcited GaAs," *Opt. Express,* Vol. 17, p. 9620, 2009.

[94] R. P. Prasankumar, A. Scopatz, D. J. Hilton, A. J. Taylor, R. D. Averitt, J. M. Zide, *et al.*, "Carrier dynamics in self-assembled ErAs nanoislands embedded in GaAs measured by optical-pump terahertz-probe spectroscopy," *Appl. Phys. Lett.,* Vol. 86, p. 201107, 2005.

[95] D. G. Cooke, F. A. Hegmann, E. C. Young, and T. Tiedje, "Electron mobility in dilute GaAs bismide and nitride alloys measured by time-resolved terahertz spectroscopy," *Appl. Phys. Lett.,* Vol. 89, p. 122103, 2006.

[96] M. C. Nuss and J. Orenstein, "Terahertz time-domain spectroscopy," in *Millimter and Submillimeter Wave Spectroscopy of Solids*, ed: Springer-Verlag, Berlin, 1998.

[97] S. E. Ralph, Y. Chen, J. Woodall, and D. McInturff, "Subpicosecond photoconductivity of $In_{0.53}Ga_{0.47}As$: Intervalley scattering rates observed via THz spectroscopy," *Physical Review B,* Vol. 54, p. 5568, 1996.

[98] M. C. Beard, G. M. Turner, and C. A. Schmuttenmaer, "Transient photoconductivity in GaAs as measured by time-resolved terahertz spectroscopy," *Physical Review B,* Vol. 62, p. 15764, 2000.

[99] P. N. Saeta, J. F. Federici, B. I. Greene, and D. R. Dykaar, "Intervalley scattering in GaAs and InP probed by pulsed far-infrared transmission spectroscopy," *Applied Physics Letters*, Vol. 60, p. 1477, 1992.

[100] Q.-l. Zhou, Y. Shi, B. Jin, and C. Zhang, "Ultrafast carrier dynamics and terahertz conductivity of photoexcited GaAs under electric field," *Applied Physics Letters*, Vol. 93, p. 102103, 2008.

[101] K. Blotekjaer, "Transport equations for electrons in two-valley semiconductors " *Electron Devices, IEEE Transactions,* Vol. 17, p. 38, 1970.

[102] A. M. Anile and S. D. Hern, "Two-valley hydrodynamical models for electron transport in gallium arsenide:Simulation of Gunn oscillations," *VLSI Design,* Vol. 15, p. 681, 2002.

[103] M. C. Hoffmann, J. Hebling, H. Y. Hwang, K.-L. Yeh, and K. A. Nelson, "Impact ionization in InSb probed by terahertz pump-terahertz probe spectroscopy," *Phys. Rev. B,* Vol. 79, p. 161201, 2009.

[104] P. C. Becker, H. L. Fragnito, C. H. B. Cruz, J. Shah, R. L. Fork, J. E. Cunningham, *et al.*, "Femtosecond intervalley scattering in GaAs," *Appl. Phys. Lett.,* Vol. 53, p. 2089, 1988.

[105] M. Grundmann, "The physics of semiconductors " *Springer-Verlag, Berlin,* 2006.

[106] B. E. Foutz, S. K. O'Leary, M. S. Shur, and L. F. Eastman, "Transient electron transport in wurtzite GaN, InN, and AlN," *Journal of Applied Physics,* Vol. 85, p. 7727, 1999.

[107] J. Hebling, M. C. Hoffmann, H. Y. Hwang, K.-L. Yeh, and K. A. Nelson, "Observation of nonequilibrium carrier distribution in Ge, Si, and GaAs by terahertz pump-terahertz probe measurements," *Phys. Rev. B,* Vol. 81, p. 035201, 2010.

[108] L. Razzari, F. H. Su, G. Sharma, F. Blanchard, A. Ayesheshim, H. C. Bandulet, *et al.*, "Nonlinear ultrafast modulation of the optical absorption of intense few-cycle terahertz pulses in n -doped semiconductors," *Phys. Rev. B,* Vol. 79, p. 193204, 2009.

[109] W. Walukiewicz, L. Lagowski, L. Jastrzebski, M. Lichtensteiger, and H. C. Gatos, "Electron mobility and free-carrier absorption in GaAs: Determination of the compensation ratio," *Journal of Applied Physics,* Vol. 50, p. 899, 1979.

[110] D. G. Cooke, "Time-resolved terahertz spectroscopy of bulk and nanoscale semiconductors " PhD, Department of physics University of Alberta, , Edmonton, 2007.

[111] J. F. Young, P. J. Kelly, N. L. Henry, and M. W. C. Dharma-wardana, "Carrier density dependence of hot-electron scattering rates in quasi-equilibrium electron-hole plasmas," *Solid State Communications,* Vol. 78, p. 343, 1991.

[112] D. M. Caughey, "Carrier mobilities in silicon empirically related to doping and field " *Proceedings of the IEEE,* Vol. 55, p. 2192, 1967.

[113] W. Han, D. Nezich, K. Jing, and T. Palacios, "Graphene Frequency Multipliers," *Electron Device Letters, IEEE,* Vol. 30, p. 547, 2009.

[114] N. L. Rangel and J. M. Seminario, "Graphene Terahertz Generators for Molecular Circuits and Sensors," *The Journal of Physical Chemistry A,* Vol. 112, p. 13699, 2008.

[115] S. A. Mikhailov, "Non-linear electromagnetic response of graphene," *Europhysics Letters,* Vol. 79, p. 27002, 2007.

[116] S. A. Mikhailov and K. Ziegler, "Nonlinear electromagnetic response of graphene: frequency multiplication and the self-consistent-field effects " *Journal of Physics: Condensed Matter* Vol. 20, p. 384204, 2008.

[117] S. A. Mikhailov, "Non-linear graphene optics for terahertz applications," *Microelectronics Journal,* Vol. 40, p. 712, 2009.

[118] A. R. Wright, X. G. Xu, J. C. Cao, and C. Zhang, "Strong nonlinear optical response of graphene in the terahertz regime," *Applied Physics Letters,* Vol. 95, p. 072101, 2009.

[119] K. S. Novoselov, A. K. Geim, S. V. Morozov, D. Jiang, Y. Zhang, S. V. Dubonos, *et al.*, "Electric Field Effect in Atomically Thin Carbon Films," *Science,* Vol. 306, p. 666, 2004.

[120] M. J. Allen, V. C. Tung, and R. B. Kaner, "Honeycomb Carbon: A Review of Graphene," *Chemical Reviews,* Vol. 110, p. 132, 2009.

[121] D. S. L. Abergel, V. Apalkov, J. Berashevich, K. Ziegler, and T. Chakraborty, "Properties of graphene: a theoretical perspective," *Advances in Physics,* Vol. 59, p. 261, 2010.

[122] A. H. C. Neto, F. Guinea, N. M. R. Peres, K. S. Novoselov, and A. K. Geim, "The electronic properties of graphene," *Reviews of Modern Physics,* Vol. 81, p. 109, 2009.

[123] K. S. Novoselov, A. K. Geim, S. V. Morozov, D. Jiang, M. I. Katsnelson, I. V. Grigorieva, *et al.*, "Two-dimensional gas of massless Dirac fermions in graphene," *Nature,* Vol. 438, p. 197, 2005.

[124] Y. Zhang, Y.-W. Tan, H. L. Stormer, and P. Kim, "Experimental observation of the quantum Hall effect and Berry's phase in graphene," *Nature,* Vol. 438, p. 201, 2005.

[125] S. Kim, J. Nah, I. Jo, D. Shahrjerdi, L. Colombo, Z. Yao, *et al.*, "Realization of a high mobility dual-gated graphene field-effect transistor with Al_2O_3 dielectric," *Applied Physics Letters,* Vol. 94, p. 06210, 2009.

[126] F. Rana, "Graphene terahertz plasmon oscillators " *IEEE Transactions on Nanotechnology,* Vol. 7, p. 91, 2008.

[127] K. S. Novoselov, D. Jiang, F. Schedin, T. J. Booth, V. V. Khotkevich, S. V. Morozov, *et al.*, "Two-dimensional atomic crystals," *Proceedings of the National Academy of Sciences,* Vol. 102, p. 10451, 2005.

[128] E. A. Obraztsova, A. V. Osadchy, E. D. Obraztsova, S. Lefrant, and I. V. Yaminsky, "Statistical analysis of atomic force microscopy and Raman spectroscopy data for estimation of graphene layer numbers," *physica status solidi (b),* Vol. 245, p. 2055, 2008.

[129] A. Reina, X. Jia, J. Ho, D. Nezich, H. Son, V. Bulovic, *et al.*, "Large Area, Few-Layer Graphene Films on Arbitrary Substrates by Chemical Vapor Deposition," *Nano Letters,* Vol. 9, p. 30, 2008.

[130] K. S. Kim, Y. Zhao, H. Jang, S. Y. Lee, J. M. Kim, K. S. Kim, *et al.*, "Large-scale pattern growth of graphene films for stretchable transparent electrodes," *Nature,* Vol. 457, p. 706, 2009.

[131] C. Berger, Z. Song, T. Li, X. Li, A. Y. Ogbazghi, R. Feng, *et al.*, "Ultrathin epitaxial graphite:2D electron gas properties and a route toward graphene-based nanoelectronics," *The Journal of Physical Chemistry B,* Vol. 108, p. 19912, 2004.

[132] C. Berger, Z. Song, X. Li, X. Wu, N. Brown, C. c. Naud, *et al.*, "Electronic confinement and coherence in patterned epitaxial graphene," *Science,* Vol. 312, p. 1191, 2006.

[133] S. Tanaka, K. Morita, and H. Hibino, "Anisotropic layer-by-layer growth of graphene on vicinal SiC(0001) surfaces," *Physical Review B,* Vol. 81, p. 041406, 2010.

[134] H. Hibino, H. Kageshima, and M. Nagase, "Graphene growth on silicon carbide," *NTT Technical Review,* Vol. 8, p. 1, 2010.

[135] M. L. Sadowski, G. Martinez, M. Potemski, C. Berger, and W. A. de Heer, "Landau Level Spectroscopy of Ultrathin Graphite Layers," *Physical Review Letters,* Vol. 97, p. 266405, 2006.

[136] L. M. Malard, M. A. Pimenta, G. Dresselhaus, and M. S. Dresselhaus, "Raman spectroscopy in graphene," *Physics Reports,* Vol. 473, p. 51, 2009.

[137] R. R. Nair, P. Blake, A. N. Grigorenko, K. S. Novoselov, T. J. Booth, T. Stauber, *et al.*, "Fine Structure Constant Defines Visual Transparency of Graphene," *Science,* Vol. 320, p. 1308, 2008.

[138] K. F. Mak, M. Y. Sfeir, Y. Wu, C. H. Lui, J. A. Misewich, and T. F. Heinz, "Measurement of the Optical Conductivity of Graphene," *Physical Review Letters,* Vol. 101, p. 196405, 2008.

[139] J. L. Tomaino, A. D. Jameson, J. W. Kevek, M. J. Paul, A. M. van der Zande, R. A. Barton, *et al.*, "Terahertz imaging and spectroscopy of large-area single-layer graphene," *Opt. Express,* Vol. 19, p. 141, 2011.

[140] S. A. Mikhailov and K. Ziegler, "Nonlinear electromagnetic response of graphene: frequency multiplication and the self-consistent-field effects " *Journal of Physics: Condensed Matter* Vol. 20, p. 384204, 2010.

Résumé en français

I. Introduction

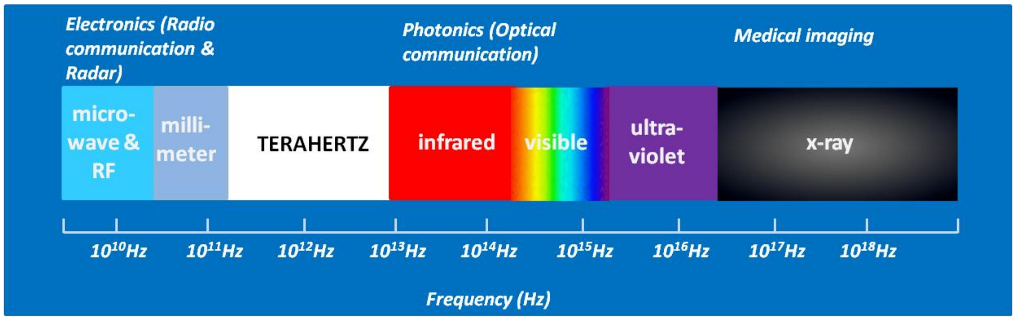

Figure 1. Spectre électromagnétique

Le spectre électromagnétique complet peut être divisé en diverses régions de longueurs d'onde, fréquences, ou énergie tel qu'illustré à la Figure 1. Dans ce spectre, la bande de fréquence THz se situe entre 0.1 et 10 THz, et constitue l'une des régions du spectre électromagnétique les moins explorées. Plusieurs phénomènes importants se produisent dans ce domaine de fréquence, ce qui fait de la région THz un champ d'intérêt très particulier pour la communauté scientifique. Par exemple, des vibrations intermoléculaires de matériaux solides sont observées aux fréquences THz. En biologie, d'importants modes collectifs de protéines vibrent aux fréquences THz. Des niveaux d'énergie rotationnelle de petites molécules tombent également à l'intérieur du domaine de fréquence THz. La rotation et les modes collectifs font également en sorte que des liquides polaires (tels que l'eau) absorbent fortement les fréquences THz. De plus, lorsqu'elles sont sous forme de plasmas gazeux ou liquides, les molécules oscillent aux fréquences THz. La matière à des températures supérieures à 10 K émet des radiations de corps noir qui tombent également dans le domaine de fréquence THz.

Parmi les applications scientifiques des ondes térahertz de haute énergie, un des plus grands défis est la spectroscopie non linéaire. En utilisant des sources THz intenses, il est aujourd'hui possible d'étudier la réponse optique non linéaire de matériaux aux fréquences THz et à l'échelle de l'ordre des picosecondes (et même des fractions de picosecondes). Par exemple, l'excitation d'une couche de GaAs de type-*n* par une impulsion THz intense avec un champ magnétique d'une amplitude maximale de 70 kV/cm a permis d'observer une émission cohérente de longue durée de vie (centrée à environ 2 THz), ainsi que des oscillations porteuses de Rabi entre les niveaux énergétiques des impuretés présentes dans le semi-conducteur [13, 14]. De plus, ces sources, couplées à l'usage de pompe-THz / techniques-de-sondage-THz, ont permis l'observation d'une décroissance dans l'absorption THz due à la diffusion intervallaire de semi-conducteurs dopés tels InGaAs, GaAs, Si, et Ge [19-21]. Les champs THz intenses ont été utilisés pour faire le plan de l'anisotropie de la masse effective pour la bande de conduction non parabolique d'un film mince de InGaAs [23].

En dépit des résultats mentionnés ci-haut, le champ de la spectroscopie THz non linéaire n'en est toujours qu'à ses débuts. Le meilleur reste à venir, puisque la principale limitation est la disponibilité des sources THz de hautes puissances. Sans surprise, de nombreux chercheurs autour du monde sont à l'œuvre pour développer les sources THz intenses dans le but d'exploiter cette sphère de recherche.

II. Génération des THz intenses

Il existe diverses façons de générer des radiations THz en utilisant des lasers femtosecondes. L’une des façons les plus conventionnelles est par l’usage d’antennes photoconductrices. Lorsque des oscillateurs sont utilisés pour générer des radiations THz, l’antenne photoconductrice est un bon choix. Dans le cas de systèmes lasers amplifiés, les effets non linéaires dans le semi-conducteur empêchent l’utilisation d’antennes photoconductrices. Lorsqu’il s’agit de lasers amplifiés, la correction optique dans un cristal non linéaire est plus aisément faisable. Normalement, des cristaux de ZnTe sont utilisés pour la génération THz, car ils satisfont à la condition de l’accord des phases ($v_{opt}^{gr} \approx v_{THz}^{ph}$), mais le coefficient électro-optique trop faible ne permet pas une efficacité de génération qui soit supérieure à l’ordre de 10^{-5}. D’autres cristaux tels que $LiNbO_3$ ne pouvaient être utilisés auparavant dû au décalage des phases entre les vitesses de groupe et de phase des impulsions optique et THz respectivement. Une nouvelle méthode a été proposée pour accorder les vitesses dans un cristal $LiNbO_3$, tel que discuté ci-dessous.

A. La technique d’inclinaison du front d’impulsion

En 2002, Hebling *et al.* ont proposé une méthode pour générer des radiations THz intenses [65], et dont l’efficacité a par la suite été démontrée par ce même groupe [50, 66]. La technique consiste à incliner le front d’impulsion de la pompe optique afin d’accorder la vitesse de groupe de l’impulsion optique avec la vitesse de phase de l’impulsion THz.

Des grillages de diffraction optique peuvent être utilisés pour introduire l’inclinaison du front d’impulsion dans le faisceau optique. Le front d’impulsion incliné est calculé à partir de l’Éq. 1. Si un faisceau optique est incident au grillage avec un angle d’incidence α, il sera diffracté avec un angle β, une inclinaison du front d’impulsion θ_c sera introduite dans le faisceau optique suivant l’équation suivante:

$$tan\theta_c = \frac{F}{n_{opt}} \frac{mN\lambda}{cos(\beta)} \qquad (1)$$

Ici, m est l'ordre de la diffraction, N est le nombre de rainures par millimètre du grillage de diffraction optique, λ est la longueur d'onde du faisceau optique, F est le ratio de démagnification des lentilles utilisées pour produire l'image du faisceau optique diffracté après le grillage sur la position du cristal $LiNbO_3$, et n_{opt} l'indice de réfraction du faisceau optique à l'intérieur du cristal $LiNbO_3$.

B. *Montage expérimental*

Pour développer cette source, le laser kHz Ti:saphir disponible dans le laboratoire ALLS au campus INRS-ÉMT de Varennes est utilisé. Ce laser produit des impulsions laser de 4 mJ, de durée de 30 fs/impulsion, à un taux de répétition de 1 kHz et dont la longueur d'onde est 800 nm. Le faisceau optique possède un diamètre de 5 mm. Le schéma du montage expérimental est illustré à la Figure 2.

Le faisceau pompe est divisé en deux parties en utilisant une combinaison de lames demi-onde et un polariseur. Le faisceau polarisé horizontalement est d'abord réduit par un facteur 2 en utilisant un télescope constitué de deux lentilles dont les distances focales sont 200 mm et -100 mm respectivement. Cette réduction est nécessaire afin d'accroître l'intensité du faisceau pompe à la position du cristal. Une fois réduit, le réseau horizontalement polarisé est lancé au réseau de diffraction optique (qui est plus efficace pour la polarisation-H). Quant au faisceau verticalement polarisé, celui-ci est expédié du côté de la détection (sonde). Le faisceau pompe est incident sur le grillage de diffraction optique avec un angle d'incidence de 37.31°, déterminé par Éq. 1. Après être diffracté par le réseau, le faisceau pompe est imagé sur le cristal avec une réduction de 1.7, en utilisant une lentille dont la distance focale est 75 mm. Après les lentilles, une lame demi-onde est placée entre les lentilles et le cristal, ceci dans le but de faire tourner la polarisation du faisceau pompe de l’horizontale à la verticale. Le résultat est une polarisation du faisceau pompe qui est parallèle à l’axe-z (où l’axe-z est la direction de l’axe extraordinaire). Le rayonnement THz est généré à partir du cristal puis capté par un miroir parabolique décalé recouvert d’une couche d’or. Le faisceau THz est orienté sur un détecteur en cristal ZnTe de 0.5 mm d’épaisseur à l’aide d’un miroir décalé. Afin de maintenir la linéarité de la détection, le champ électrique THz est réduit au niveau du cristal ZnTe à l’aide d’un polariseur en grille métallique et de plaques de silicone de haute résistivité. L’échantillonnage électro-optique (ÉO) en espace libre est utilisé pour la détection des signaux THz [47].

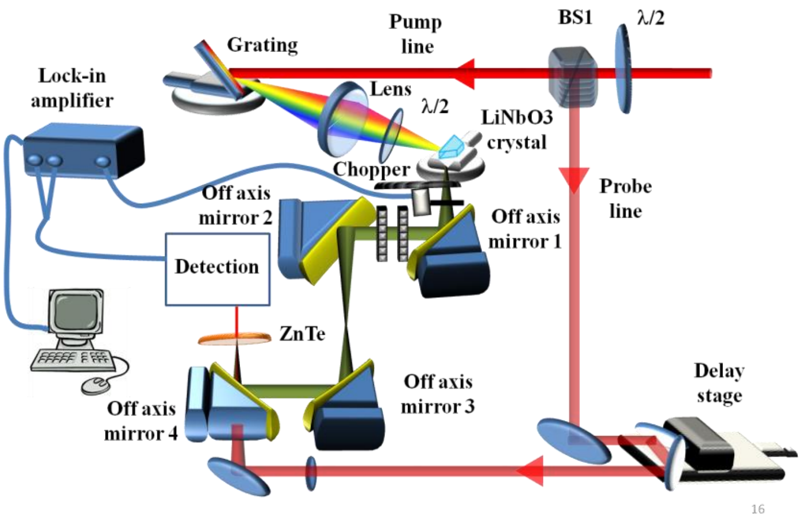

Figure 2. Schéma du montage expérimental

C. Résultats

L’énergie THz est mesurée en utilisant un détecteur pyroélectrique (Coherent Molectron J4–05) de Microtech® Instrument, inc. La Figure 3 montre la relation entre le champ électrique THz et l’énergie de la pompe optique. L’énergie maximale mesurée est 0.6 μJ, avec une énergie induite à la pompe de 0.9 mJ à la surface du cristal sLN. Ceci donne l’efficacité de conversion maximale de 6×10^{-4}.

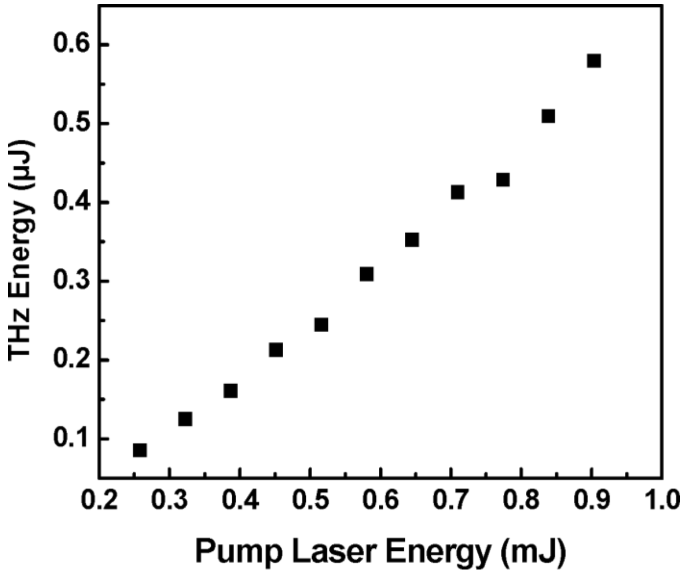

Figure 3. Énergie THz en fonction de l'énergie de la pompe optique

III. Détection THz par interférométrie du domaine spectral

Pour l'échantillonnage ÉO, une impulsion laser femtoseconde linéairement polarisée se copropage avec une impulsion THz picoseconde dans in cristal ÉO. Le champ électrique THz induit de la biréfringence dans le cristal, ce qui change la polarisation de l'impulsion laser qui s'y copropage linéairement. Le changement de phase entre les deux composantes de la polarisation du faisceau sonde (qui est proportionnel au champ électrique THz) peut être mesuré en utilisant des polariseurs croisés installés avant et après le cristal détecteur. Dans ce cas, le changement de phase apparaît comme une modulation dans l'intensité du faisceau sonde. La forme d'onde THz complète peut être reconstruite en balayant le faisceau sonde sur la totalité de l'impulsion THz.

Les techniques basées sur l'échantillonnage ÉO ont utilisé deux polariseurs pour mesurer le champ électrique THz. Toutefois, avec les avancées récentes dans les techniques de génération THz de haute puissance, l'utilisation de cristaux plus épais pose un problème majeur en termes de la rotation excessive qui est appliquée au faisceau. Si le champ électrique THz est suffisamment élevé pour introduire une différence de phase de plus de 90°, cela mène à une inversion dans l'intensité de modulation du faisceau de détection, causant des ambiguïtés dans les champs THz mesurés [74]. Cette situation est appelée "surrotation ". La biréfringence introduite dans le cristal ÉO est proportionnelle à la fois au champ électrique THz et à l'épaisseur du cristal. Il serait en principe possible de faire usage de cristaux plus minces afin d'éviter le phénomène de surrotation. Ce n'est toutefois pas désirable à cause des effets de réflexion interne. De plus, l'utilisation de cristaux minces réduit le rapport signal sur bruit (RSB) du signal THz mesuré, cela étant dû à la diminution de la distance d'interaction.

Afin de pouvoir surmonter la limitation de la surrotation dans la mesure du signal THz intense, nous proposons une nouvelle technique basée sur l'interférométrie du domaine spectral (IDS). Pour cette technique, au lieu d'utiliser deux polariseurs croisés, nous mesurons le changement dans la différence de phase introduite and le faisceau sonde par le champ électrique THz.

A. *Modèle expérimental*

Une nouvelle technique pour détecter la forme d'onde THz, utilisant l'IDS, est proposée. Le montage expérimental est illustré à la Figure 4.

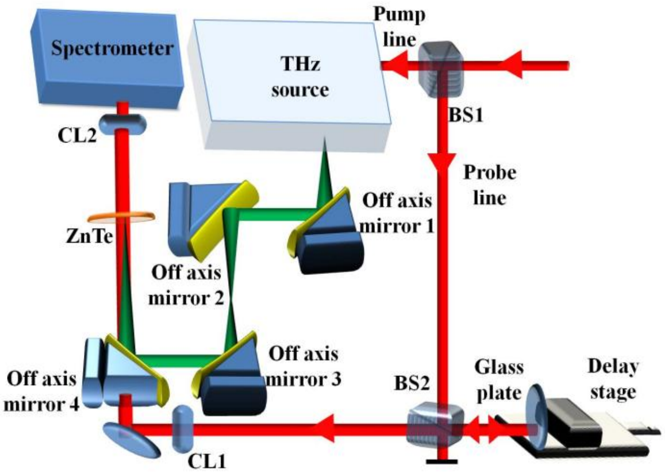

Figure 4. Montage expérimental

Le miroir semi-réfléchissant (BS1) divise le faisceau laser en un faisceau sonde et un faisceau pompe. Le faisceau pompe est utilisé pour générer le signal THz en utilisant la technique du front d'impulsion incliné dans un cristal $LiNbO_3$. Cette source génère des impulsions THz de 0.3 μJ, avec une bande passante qui s'étend de 0.1 THz à 3 THz. Le miroir semi-réfléchissant (BS2) divise le faisceau sonde en deux parties égales. La partie réfléchie du faisceau est dirigée sur une lame de verre de 0.3 mm d'épaisseur. Les deux surfaces de la lame de verre réfléchissent environ 4% du faisceau incident. La moitié du faisceau sonde qui est réfléchi par la lame de verre est transmise à travers le miroir semi-réfléchissant BS2. Le signal qui est réfléchi par la lame de verre consiste en deux impulsions : une qui est réfléchie par la surface avant (impulsion avant), et la seconde qui est réfléchie par la surface arrière (impulsion arrière). L'impulsion avant et l'impulsion arrière sont séparées par 3 ps (en raison de l'indice de réfraction de la lame verre qui est de 1.5). En utilisant une lentille cylindrique (CL1), ces deux impulsions se propagent à travers un orifice dans le miroir décalé, et leur profil spatial pseudolinéaire est orienté vers un détecteur en cristal ZnTe, de 0.5 mm d'épaisseur, à la même position que le faisceau THz. Une lentille cylindrique (CL2) est utilisée pour collimater le faisceau sonde, qui est ensuite envoyé dans un spectromètre. Le spectromètre, fait sur mesure, est constitué d'un grillage de diffraction optique contenant 600 rainures/mm, d'une lentille cylindrique ayant une distance focale f = 100 mm, et d'une caméra 2D CCD de 760 × 1024 pixels. Par l'usage du spectromètre, les franges d'interférence sont observables dû à l'interférence entre les impulsions avant et arrière. Avec l'IDS, les différentes composantes spectrales sont séparées après le grillage de diffraction optique et, de cette façon, les différentes composantes spectrales de l'impulsion sonde ne sont plus sous blocage de mode (*mode-locked*). Pour cette raison, il devient possible de mesurer le patron d'interférence sur la gamme de profondeur de la technique IDS (déterminée par le spectromètre utilisé).

Afin de mesurer l'impulsion THz complète, une ligne de délai optique est utilisée pour faire varier le délai entre l'impulsion THz et l'impulsion optique. L'impulsion THz est temporairement appariée avec l'impulsion sonde arrière. Le délai entre l'impulsion avant et l'impulsion arrière est suffisamment long (3 ps) pour que l'impulsion avant puisse passer à travers le cristal ZnTe sans voir le champ électrique THz. La présence du champ électrique THz a pour effet de changer l'indice de réfraction du cristal ZnTe via l'effet Pockel. L'impulsion arrière subit ce changement dans l'indice de réfraction, alors que l'impulsion avant ne le subit pas, introduisant ainsi une différence de phase entre les deux impulsions sondes optiques. Le changement de phase entre ces deux impulsions est proportionnel au champ électrique THz.

B. *Mesure du champ électrique THz*

Pour des fins de comparaison, le champ électrique d'une impulsion THz, générée à partir d'une source $LiNbO_3$ à inclinaison du front d'impulsion, a été mesuré en utilisant simultanément l'échantillonnage ÉO et l'interférométrie DS. Les résultats de ces mesures sont illustrés à la Figure 5.

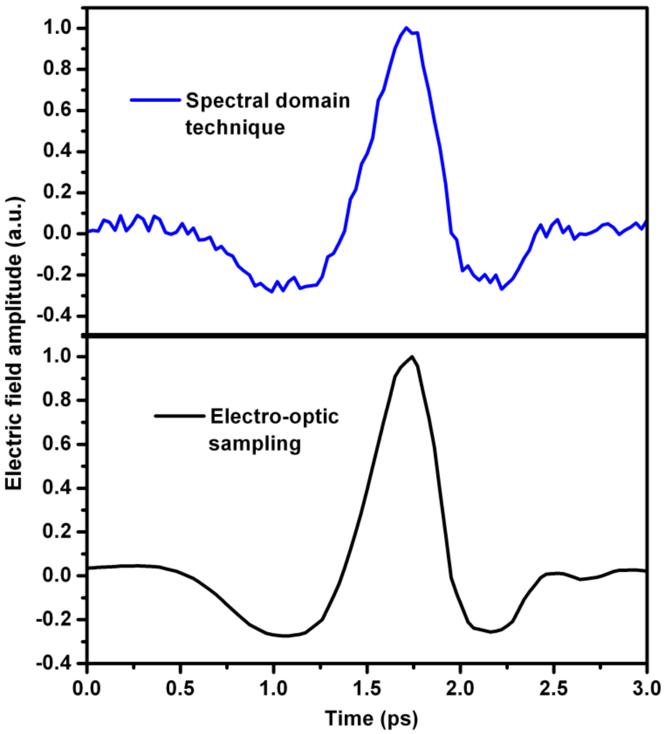

Figure 5. Impulsion THz mesurée avec une technique de domaine spectral (bleu) et par échantillonnage électro-optique (noir)

IV. Spectroscopie THz non linéaire de semi-conducteurs

Dans la partie précédente, la génération et la détection du champ électrique THz intense ont été discutées. Avec la disponibilité des sources THz de hautes puissances, l’étape suivante consiste à étudier différents phénomènes pouvant résulter des interactions entre différents matériaux et les champs électriques THz intenses. En temps normal, la spectroscopie THz est utilisée pour caractériser la réponse dynamique d’un semi-conducteur. Par conséquent, pour notre premier matériau, nous étudions un échantillon d’arséniure de gallium (GaAs) dont la réponse non linéaire est dépendante du champ électrique THz.

A. Mesures par pompe-optique/ sonde-THz d'un échantillon GaAs

Pour les expériences sur GaAs, des impulsions THz de hautes énergies sont générées par correction optique dans une gaufrette de ZnTe monocristallin, équipée d'un large orifice (75 mm de diamètre) [27, 92]. La source produit des impulsions THz picosecondes dans une gamme de fréquences allant de 0.1 à 3 THz, avec une énergie de 0.6 μJ.

B. Expérience de sondage par pompe optique THz

Une technique de pompe-optique / sonde-THz intense (POST) est appliquée afin d'explorer la dynamique électronique non linéaire du GaAs non dopé [95]. L'expérience POST est effectuée sur une gaufrette GaAs semi-isolante (SI) de 0.5 mm d'épaisseur. L'échantillon est placé au point focal du faisceau THz, et un faisceau pompe optique (longueur d'onde de 800 nm, durée d'impulsion de 40 fs, fluence de 8 μJ/cm^2) est utilisé pour photo-exciter l'échantillon. Deux polariseurs en grille métallique ont été utilisés pour faire varier le champ électrique THz à la position de l'échantillon.

Tout d'abord, la transmission THz au sommet de l'impulsion THz est mesurée, en fonction du temps de délai pompe-sonde. Il s'agit d'une méthode communément utilisée pour sonder la dynamique ultrarapide des porteurs de charge des semi-conducteurs au cours des expériences de POST linéaire [96, 97]. L'expérience a été effectuée pour la transmission, à des champs électriques faible et élevé de sonde THz, dans le GaAs photo-excité, où les champs élevé et faible correspondent respectivement à 173 kV/cm et 4 kV/cm.

La Figure 6 montre la transmission THz en fonction du temps de délai pompe-sonde pour les champs THz élevé et faible, respectivement. L'encart à la Figure 6 montre la dynamique sur une longue période de temps.

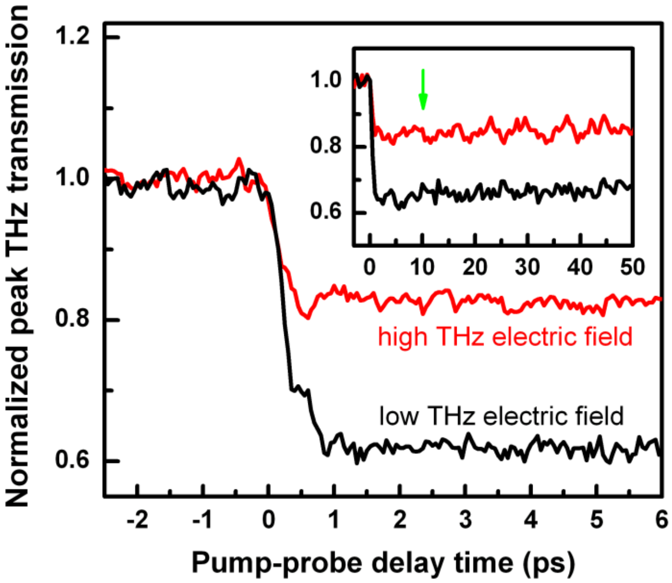

Figure 6. **Transmission normalisée du champ électrique maximal d'une pulsation THz, pour les champs Thz faible et élevé, en fonction du temps de délai pour une impulsion pompe optique de 800 nm et 40 fs [95].**

C. Interprétation théorique

L'impulsion pompe de 800 nm photo-excite les paires électron-trou dans l'échantillon GaAs qui normalement est un isolant. En raison du pompage optique, les électrons photo-excités sont injectés par le faisceau pompe dans la vallée Γ centrale à plus haute mobilité de la bande de conduction. Aux champs sondes THz faibles, la transmission de l'impulsion THz à travers l'échantillon de GaAs photo-excité est approximativement 60% de la transmission à travers l'échantillon non excité. Toutefois, aux champs sondes THz élevés, le changement relatif de la transmission est considérablement réduit en comparaison au champ sonde THz faible, ce qui suggère qu'un blanchiment d'absorption se produit. Le blanchiment d'absorption est défini ici comme étant la diminution de l'absorption THz de l'échantillon GaAs photo-excité aux champs THz élevés par rapport aux champs THz faibles. Le blanchiment d'absorption observé au cours des interactions entre les pulsations THz intenses et les électrons photo-excités dans la bande de conduction de l’échantillon GaAs peut être attribué à la diffusion intervallaire, induite par les THz, entre des vallées non équivalentes. Notre attention s’est particulièrement concentrée sur la dynamique électronique entre la vallée *Γ* et *L* (qui est la vallée de plus haute énergie la plus près de *Γ* dans GaAs) de la bande de conduction de l’échantillon analysé.

La Figure 7 montre les parties réelle et imaginaire de la conductivité complexe mesurée aux champs sondes THz élevés et faibles, obtenue avec un temps de délai pompe-sonde de 10 ps. La conductivité au champ faible est en bon accord avec le modèle de Drude. Avec le champ élevé, lorsque la conductivité est obtenue à partir du modèle de Drude basée sur la diffusion intervallaire, celle-ci s’harmonise mieux au modèle que lorsque le phénomène de diffusion intervallaire est négligé, tel qu’observé aux parties (b) et (c) de la figure suivante.

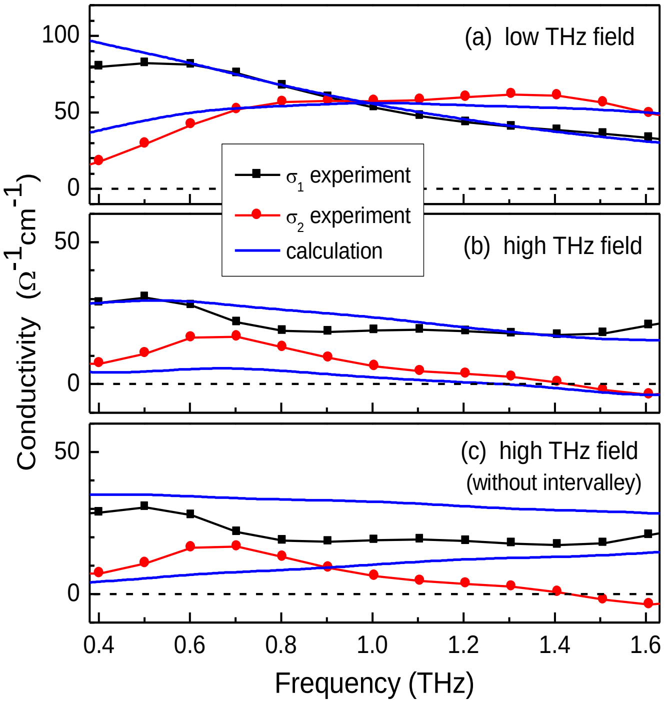

Figure 7. Parties réelle et imaginaire de la conductivité complexe obtenue à un temps de délai pompe-sonde de 10 ps, mesurée à un champ sonde THz faible (a) et élevé (b). Les lignes bleues dans (a) et (b) sont les déconvolutions correspondantes à partir du modèle de transfert électronique. (c) montre la conséquence de négliger la diffusion intervallaire dans le modèle (adaptation de la référence [95]).

D. Effets de la densité des transporteurs de charge sur l'absorption non linéaire des radiations THz dans le GaAs

Dans la partie précédente, le blanchiment d'absorption, induit par le rayonnement THz, dans un échantillon de GaAs photo-excité, a été étudié où le faisceau pompe optique excite des électrons vers la bande de conduction de l'échantillon GaAs. Nous avons étudié l'effet de l'impulsion THz intense sur ces électrons photo-excités dans la bande de conduction de GaAs. Afin d'avoir une meilleure idée, nous avons ensuite fait varier la densité des transporteurs de charge dans la bande de conduction de l'échantillon GaAs en changeant la fluence de la pompe optique, puis nous avons étudié les effets de ces changements sur le blanchiment d'absorption. Dans cette partie, l'effet de la densité des transporteurs de charge sur l'absorption non linéaire des radiations THz par l'échantillon GaAs est étudié.

E. Définition du blanchiment d'absorption

Avant de commencer à étudier l'effet de la densité des transporteurs de charge sur le blanchiment d'absorption, il nous faut tout d'abord quantifier cet effet en définissant le "niveau de blanchiment d'absorption induit par THz" comme suit :

$$\begin{gathered} \text{level of asorption bleaching} = \Psi = \left[\left\{ \frac{T_{high}}{T_{low}} \right\} - 1 \right], \\ T_i = \frac{\int \left| E^i_{samp}(t) \right|^2 dt}{\int \left| E^i_{ref}(t) \right|^2 dt} \quad , \ i = high \text{ or } low \end{gathered} \tag{2}$$

Ici, E_{samp}^{high} , E_{ref}^{high} , E_{samp}^{low} et E_{ref}^{low} correspondent au champ électrique THz transmis à travers l'échantillon photo-excité (*samp*) et non excité (*ref*) aux champs THz élevé (133kV/cm) et faible (9kV/cm), respectivement.

F. Résultats expérimentaux et discussion

La Figure 8 montre la non-linéarité induite par les THz pour des densités de transporteurs de charge allant de 1.0×10^{17} à 10.6×10^{17} cm^{-3}. Il peut être clairement observé à partir de la Figure 8 que ψ varie de façon significative par rapport à la densité des transporteurs de charge.

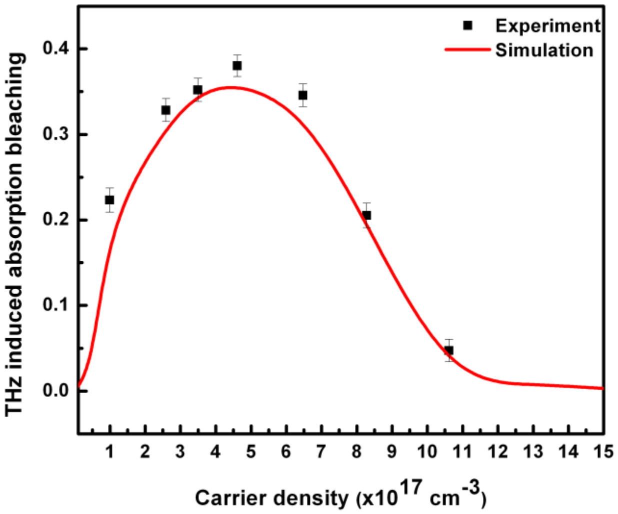

Figure 8. Tendances expérimentales (carrés noirs avec bande d'erreur) et simulées (ligne rouge) de la dépendance du blanchiment d'absorption THz en relation avec la densité des transporteurs de charge pour le GaAs photo-excité à 800 nm.

La valeur de ψ est supérieure à zéro à cause de la diffusion intervallaire entre les vallées Γ et L de la bande de conduction, tel qu'il fut expliqué dans la section précédente. ψ à la Figure 8 peut être divisé en deux régions de densité-de-transporteurs-de-charge : (i) à des densités relativement faibles ($<4.7\times10^{17}$ cm^{-3}), ψ augmente proportionnellement avec l'accroissement de la densité des transporteurs de charge de 1×10^{17} cm^{-3} jusqu'à 4.7×10^{17} cm^{-3}. Pour la plage de densités que nous avons étudiées, le blanchiment d'absorption atteint un sommet à une densité de transporteurs de charge de 4.7×10^{17} cm^{-3}; (ii) pour les densités allant de 4.7×10^{17} cm^{-3} à 10.6×10^{17} cm^{-3} (la densité maximale de transporteurs de charge sous investigation), le blanchiment d'absorption décroit de façon monotone. Pour la valeur maximale de densité étudiée (10.6×10^{17} cm^{-3}), ψ disparaît dans sa presque totalité.

De précédentes études spectroscopiques THz ont démontré que la densité d'électrons photo-éjectés et de trous a une forte influence sur la mobilité des transporteurs de charge dans le GaAs [101]. Analogue à la diffusion par les impuretés, la diffusion électron-trou (*é-t*) impose une limitation à la mobilité des électrons [91, 101, 110]. Comme la masse effective d'un trou est considérablement supérieure à celle d'un électron, la diffusion *é-t* est insuffisante pour transférer l'énergie d'un électron vers un trou. Toutefois, la diffusion *é-t* est efficace pour la relaxation de la dynamique diélectrique. Elle a pour effet de diminuer le temps de diffusion de Drude aux faibles champs THz $\tau_{\Gamma}(low)$ et par conséquent, réduit la mobilité des électrons [101]. Ceci a donc pour effet de limiter l'énergie maximale que peut atteindre l'électron et, par conséquent, diminue la diffusion intervallaire, comme cela peut être observé à partir de nos résultats expérimentaux.

V. Spectroscopie THz linéaire et non linéaire du graphène

A. Spectroscopie THz linéaire

En utilisant la spectroscopie THz linéaire, il est possible de connaître la conductivité superficielle d'un échantillon de graphène. Cette conductivité superficielle peut constituer un paramètre utile pour évaluer la qualité de l'échantillon de graphène qui est étudié. Nous avons utilisé la technique de spectroscopie THz résolue en temps (*THz time-domain spectroscopy*) pour mesurer la conductivité superficielle de l'échantillon de graphène, tel que décrit à la section suivante.

B. Détermination de la conductivité superficielle d'un échantillon de graphène par spectroscopie THz

La conductivité superficielle d'un échantillon de graphène peut être exprimée par l'équation suivante

$$t_{rel}^{(m)}(\sigma_s) = \frac{E_{G-SiC}^{(m)}}{E_{SiC}^{(m)}} = \frac{t(\sigma_s)}{t_{13}}\left(\frac{r(\sigma_s)}{r_{13}}\right)^{m-1} \tag{3}$$

Ici, $E_{G\text{-}SiC}^{(m)}$ est le champ électrique de la $m^{ème}$ impulsion suite à la transmission à travers l'échantillon/substrat et $E_{SiC}^{(m)}$ est le champ électrique de la $m^{\text{ème}}$ impulsion suite à la transmission à travers le substrat SiC. Ici, $n_1 = n_{air}$ et $n_3 = n_{SiC}$. Pour les indices de réfraction de SiC (n_{SiC} = 3.677) et de l'air (n_{air} = 1), la conductivité de la première impulsion dans le temps (sans réflexion) est donnée par

$$\sigma_s = \left(\frac{4.677}{t_{rel}^{(1)}} - 4.677\right) \times \frac{1}{377} \tag{4}$$

C. Détermination expérimentale de la conductivité superficielle

Pour la détermination expérimentale de la conductivité superficielle de l'échantillon de graphène, un système de spectroscopie THz résolue en temps (SRT) basée sur une antenne photoconductrice est utilisé. L'échantillon de graphène, fabriqué sur un substrat SiC, est placé au point focal du faisceau THz, et le détecteur THz mesure le signal THz transmit. À partir de l'Équation 3, on peut calculer la conductivité superficielle de l'échantillon de graphène, connaissant le rapport de transmission relatif (T_{rel}) à partir des données expérimentales. Pour la première impulsion dans le temps, les conductivités superficielles mesurées pour des échantillons de graphène fabriqués respectivement par NTT et l’Université Kyushu sont illustrées à la Figure 9.

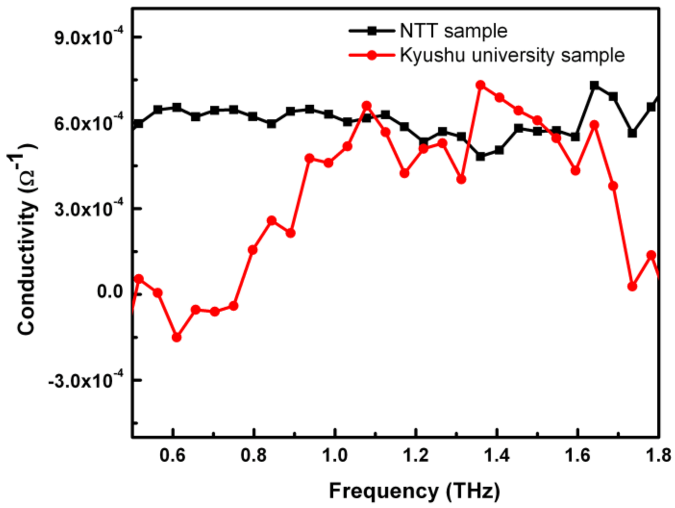

Figure 9. Conductivités expérimentales mesurées pour deux échantillons de graphène fabriqués par NTT et l’Université Kyushu

Comme on peut le voir à la Figure 9, la conductivité superficielle de l’échantillon de graphène produit par NTT est de $\sim 0.6\times10^{-3}\Omega^{-1}$. Pour cet échantillon, la conductivité superficielle est uniforme sur la plage de fréquences de 0.5 – 2THz, alors que conductivité superficielle du graphène produit par l’Université Kyushu fluctue entre 0 et $0.6\times10^{-3}\Omega^{-1}$. D’autres recherches ont rapporté une conductivité superficielle pour le graphène qui est constante sur une plage de fréquences de 0.1 – 3THz [140]. La conductivité superficielle mesurée est ~ 10 fois supérieure à $\sigma_q = e^2/4\hbar = 6.1 \times 10^{-5}\Omega^{-1}$ (σ_q étant la conductivité optique du graphène résultant des transitions inter-bandes [139]). La conductivité mesurée est plus élevée que la conductivité universelle, car la conductivité dans le domaine THz des dominée par les transitions intra-bandes et correspond à la conductivité du courant direct (CD) de l’échantillon de graphène. La spectroscopie THz peut ainsi être un outil très utile pour évaluer la qualité d’un échantillon de graphène.

D. Réponse non linéaire du graphène aux fréquences THz

De nombreux travaux théoriques révèlent que le graphène montre une forte non-linéarité aux fréquences THz [116-119].

Étude de la réponse non linéaire du graphène à une source THz intense

Mesures sur l’échantillon de graphène fabriqué par l’Université Kyushu

Pour cette évaluation, nous avons utilisé une source THz intense basée sur la technique du front d’impulsion incliné dans un cristal $LiNbO_3$ discutée précédemment. Pour cette expérience, l’énergie des impulsions THz intenses était de 0.55 μJ. Le champ électrique THz maximum est estimé à 210 kV/cm. Nous avons usé de polariseurs en grille métallique pour faire varier le champ électrique THz sur l’échantillon. L’échantillon est maintenu perpendiculaire au faisceau THz incident. Dans le but d’étudier la non-linéarité dépendante au champ THz, nous avons mesuré la transmission normalisée du champ électrique THz à travers le graphène. Pour ce faire, nous avons déterminé le rapport $\left|E(\omega)_{Sample}\right| / \left|E(\omega)_{Substrate}\right|$ entre les amplitudes spectrales de l’impulsion THz transmise à travers l’échantillon de graphène (sur un substrat SiC) $\left|E(\omega)_{Sample}\right|$ et transmise à travers le substrat SiC seul $\left|E(\omega)_{Substrate}\right|$. Les rapports correspondants sont illustrés à la Figure 10.

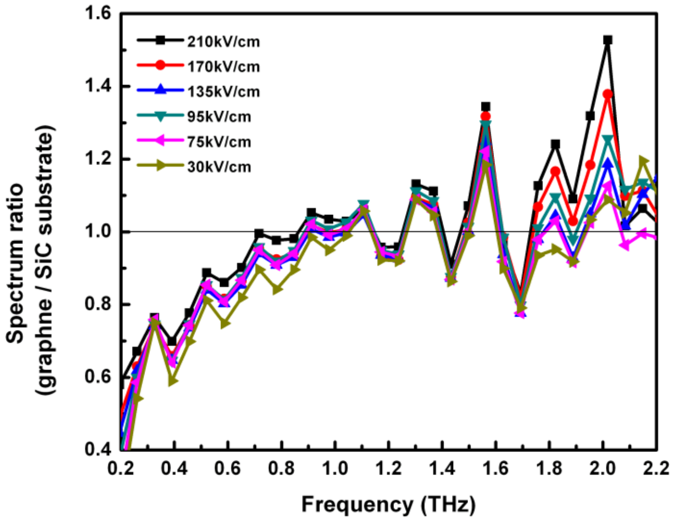

Figure 10. Transmission relative à travers l'échantillon de graphène à des champs électriques THz de diverses forces

Comme on peut l'observer à la Figire 10, le rapport spectral graphène/substrat excède 1 à une fréquence de 1.6 THz ainsi que pour une gamme de fréquences entre 1.8 et 2.1 THz. De plus, cette augmentation est dépendante de la force du champ électrique THz. À mesure que nous diminuons l'énergie du champ électrique THz, ce rapport décroît, atteignant approximativement la valeur de 1 pour un champ électrique THz de 30 kV/cm.

Mesures sur l'échantillon de graphène fabriqué par NTT

Pour la prise de mesures sur l'échantillon de graphène produit par NTT, nous avons utilisé notre source THz intense basée sur la correction optique par ZnTe à large orifice. Dans cette expérience, l'énergie des impulsions THz intenses était de 0.5 μJ. Le champ électrique THz maximum est estimé à 133 kV/cm. La Figure 11 montre le rapport spectral $\left|E(\omega)_{Sample}\right| / \left|E(\omega)_{Substrate}\right|$ en fonction de la fréquence THz.

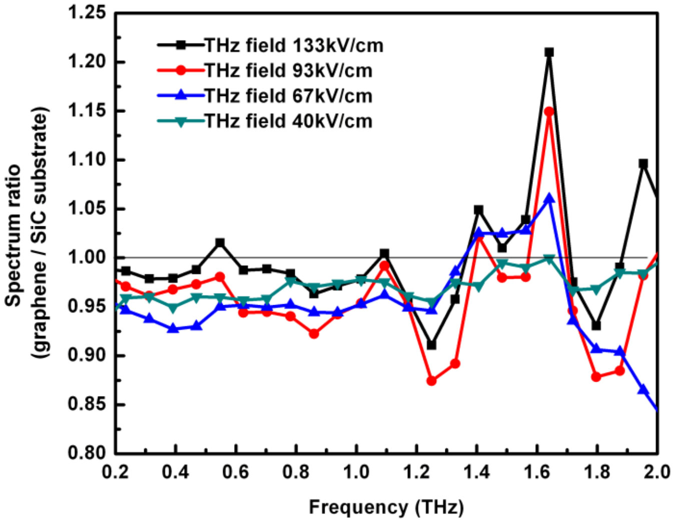

Figure 11. Transmission relative à travers l'échantillon de graphène à des champs électriques THz de diverses forces

Nous observons une augmentation de la transmission THz sur une large gamme de fréquences THz allant de 1.4 THz à 1.7 THz. Une autre observation intéressante est que cette augmentation dépend de la valeur du champ électrique THz. Nous observons une augmentation maximale de 21% de la transmission THz, pour un champ électrique THz de 133 kV/cm, à une fréquence de 1.64 THz. Lorsque nous diminuons le champ THz à 93 kV/cm, le rapport spectral est réduit à 15%. En diminuant davantage le champ électrique THz à 67 kV/cm, le rapport est réduit à 6%, et finalement disparaît à 40 kV/cm.

Puisque l'échantillon de graphène (sur un substrat SiC) devrait être un meilleur conducteur que le substrat SiC seul, nous nous attendons à ce que la transmission THz à travers l'échantillon de graphène soit moindre que le substrat SiC seul. De ce fait, il serait attendu que le rapport $\left|E(\omega)_{Sample}\right| / \left|E(\omega)_{Substrate}\right|$ soit toujours inférieur à 1. Or, contrairement à ce dont nous nous attendions, nous observons une augmentation de la transmission relative à certaines fréquences.

Nous découvrons en plus que cette augmentation est dépendante à la force du champ électrique THz. Cela est consistant pour deux échantillons différents, produits à partir de techniques différentes, utilisant deux sources THz différentes (ayant des spectres différents).

VI. Conclusion

En conclusion, nous avons développé la source THz intense basée sur la technique du front d'impulsion incliné. En ce qui a trait à la détection THz, afin d'être capables de surmonter les limitations de la surrotation, nous avons développé une nouvelle technique de détection basée sur l'interférométrie du domaine spectral. L'une des sources étant développée et caractérisée, nous avons utilisé cette source pour la spectroscopie THz non linéaire de semi-conducteurs. Nous avons utilisé la technique pompe-optique/sonde-THz pour étudier la dynamique des transporteurs de charge sur des échantillons de GaAs. Nous avons également étudié la réponse THz linéaire et non linéaire d'échantillons de graphène fabriqués au Japon, par l'Université Kyushu et NTT, respectivement.